UNIVERSITY OF CALIFORNIA
RIVERSIDE

Assessment of AlCl as a Candidate for Laser Slowing

A Dissertation submitted in partial satisfaction
of the requirements for the degree of

Doctor of Philosophy

in

Physics

by

John Daniel

September 2022

Dissertation Committee:

Dr. Boerge Hemmerling, Chairperson
Dr. Chris Bardeen
Dr. Allen Mills

The Dissertation of John Daniel is approved:

Committee Chairperson

University of California, Riverside

Acknowledgments

I am grateful to my advisor, without whose help and Ferengi proverbs, I would not have been here.

To my wife for all the support.

ABSTRACT OF THE DISSERTATION

Assessment of AlCl as a Candidate for Laser Slowing

by

John Daniel

Doctor of Philosophy, Graduate Program in Physics
University of California, Riverside, September 2022
Dr. Boerge Hemmerling, Chairperson

Following the successes obtained from using lasers to cool and trap atoms, the same principles are being applied to molecules. Finding a molecule that is amenable to laser-cooling is not trivial. Aluminum monochloride (AlCl) has been proposed as a viable candidate for laser-cooling and trapping due to predicted large Franck-Condon factors and short excited state lifetime, allowing for efficient imparting of momentum from photons. To be efficiently slowed, multiple electrons must be cycled between the ground and excited states. This thesis presents a detailed derivation of the hamiltonian terms that must be understood for the $X^1\Sigma^+ \leftrightarrow A^1\Pi$ transition in AlCl. Initial absorption spectroscopy measurements are performed on the transition, yielding measurements of molecular constants. From these constants, the Franck-Condon factor for the cycling transition is determined to be 0.9988, which is ideal for cycling. The choice of chemical compound that is ablated to produce AlCl for these experiments is not trivial. It is found that a mixing aluminum and potassium chloride with a molar ratio of 1:1.55 produces the optimal yield of AlCl. Additionally, a magneto-optical-trap apparatus is discussed and tested here on ytterbium. This

test realizes the successful trapping of neutral ytterbium, marking the creation of the first magneto-optical-trap at the University of California, Riverside. The vibrational and rotational properties of AlCl clearly make it a strong candidate for laser-cooling and trapping, however there are still many challenges that must be overcome before such experiments can be successful.

Contents

List of Figures **xi**

List of Tables **xiv**

1 Introduction **1**
1.1 Cold Molecules . . . 1
1.2 Interest in AlCl . . . 3
1.2.1 Variation of $\dot{\mu}$ . . . 4
1.3 Is AlCl A Viable Candidate For Slowing? . . . 5

2 AlCl Hamiltonian **6**
2.1 Electronic Structure . . . 6
2.2 Basis Sets . . . 8
2.2.1 Primitive Basis Set . . . 8
2.2.2 Parity-Conserved Basis Set . . . 9
2.3 $X^1\Sigma^+$ Hamiltonian . . . 9
2.4 $A^1\Pi$ Hamiltonian . . . 10
2.5 Dunham Expansion . . . 11
2.6 Λ-Doubling . . . 11
2.7 Electric Quadrupole Term . . . 12
2.8 Hyperfine Term . . . 15
2.9 Zeeman Term . . . 19
2.10 $a^3\Pi$ . . . 24

3 UV Laser System **27**
3.1 Second-Harmonic Generation . . . 29
3.2 Sum-Frequency Generation . . . 32
3.3 Wavemeter Calibration . . . 33
3.3.1 Temperature-Stabilized HeNe . . . 33
3.3.2 Rb Pump-Probe Spectroscopy . . . 34

4 Cryogenic Buffer-Gas Beam Source **36**
4.1 Cryogenic System . . . 38
4.1.1 Compressor . . . 38
4.1.2 Shields . . . 39
4.1.3 Cell . . . 41
4.1.4 Temperature Monitoring . . . 46
4.2 Helium Buffer Gas . . . 47
4.2.1 Yb Demonstration of Buffer-Gas Cooling . . . 49
4.2.2 Sorbs . . . 50
4.3 Laser Ablation . . . 51
4.3.1 Laser Setup . . . 51

5 Absorption Spectroscopy **52**
5.1 Measurement Procedure . . . 53
5.2 Line Broadening Mechanisms . . . 53
5.2.1 Lorentzian Broadening . . . 53
5.2.2 Gaussian Broadening . . . 54
5.2.3 Voigt Broadening . . . 54
5.3 Line Intensities . . . 56
5.3.1 Franck-Condon Factors . . . 56
5.3.2 Hönl-London Factors . . . 56
5.3.3 Hyperfine Transistion Probability . . . 57
5.4 Data Analysis . . . 58
5.4.1 Signal Quality Improvement . . . 58
5.4.2 Line Centers . . . 59
5.4.3 Molecular Constants . . . 60
5.5 Franck-Condon Factors . . . 64
5.6 Temperature Measurement . . . 64

6 Target Study **68**
6.1 Al:KCl Mixing . . . 69
6.2 Laser Setup . . . 70
6.3 Results . . . 71

7 Slowing and Trapping Yb **74**
7.1 Zeeman Slower . . . 74
7.2 Magnetic Coils . . . 78
7.3 Laser Setup . . . 80
7.4 Yb MOT . . . 82

8 Conclusions **84**
8.1 Dark States . . . 85
8.2 Laser Upgrades . . . 86
8.2.1 SFG Bowtie . . . 86
8.2.2 Doubled Vexlum . . . 87

8.2.3 Quadrupoled Fiber . . . 88
8.3 Different Chloride Sources . . . 88
8.4 Final Thoughts . . . 89

Bibliography **91**

A Constants **97**

B Spherical Tensors **99**
B.1 Wigner . . . 100
B.1.1 The Wigner-Eckart Theorem . . . 100
B.1.2 Common Matrix Elements . . . 100
B.1.3 Common Reduced Matrix Elements . . . 101
B.1.4 Common Wigner 3j Symbols . . . 102
B.1.5 Coupled Matrix Elements . . . 102

C Artiq **104**
C.1 Device Summary . . . 104
C.2 Scan Single Laser . . . 105
C.3 Raster Target . . . 107

D Line Centers **108**

List of Figures

2.1 Angular momentum diagram for the singlet states of AlCl. Since **L** precesses rapidly about the inter-nuclear axis, the component, **Λ**, of **L** along this axis is coupled to the molecular rotation, **R** to obtain the total angular momentum **J** = **R** + **Λ**. All hyperfine interactions are excluded from this figure. 8

2.2 $X^1\Sigma^+$ and $A^1\Pi$ hyperfine states for $J = J' = 1$. Shades of red correspond to $F_1 = 3/2$, shades of green correspond to $F_1 = 5/2$, and shades of blue correspond to $F_1 = 7/2$. 18

2.3 A least-squares fit of R(0) fluorescence data provided by the McCarron lab at the University of Connecticut. The circles are the data with error bars. The vertical lines at the bottom indicate where the $A^1\Pi$ hyperfine states lie and their relative intensities. 20

2.4 Simulated Zeeman splitting of the hyperfine structure for $A^1\Pi(\nu'=0, J'=1)$ state of AlCl. 23

2.5 Simulated Zeeman splitting of the hyperfine structure for $A^1\Pi(\nu'=0, J'=2)$ state of AlCl. 23

2.6 Simulated Zeeman splitting of the hyperfine structure for $A^1\Pi(\nu'=0, J'=3)$ state of AlCl. 24

3.1 A schematic of the THG system that utilizes an LBO crystal in a bowtie cavity to frequency-double the 784.5 nm Ti:Sapph output (red) to 392.3 nm (blue). These two frequencies are summed in an LBO crystal to produce 261.5 nm UV light (magenta) for absorption spectroscopy of the $X^1\Sigma^+ \rightarrow A^1\Pi$ transition of AlCl. 28

3.2 Pump-Probe absorption spectroscopy setup using a heated, rubidium vapor cell as an atomic reference. 34

3.3 Rb Pump-Probe Absorption Spectroscopy Data 35

4.1 Dewar horizontal cross-section. Cell is depicted in single-stage configuration. Also depicted is the optical setup of the ablation laser. 37

4.2 Cooldown of the 40K (orange) and 4K (blue) stages of the cryogenic system in an empty dewar with super-insulation thermally isolating each stage. This test was without any attached heat load, i.e. no thermal shields, cell, etc. . 39

4.3 Heat Links connecting 4K pulse tube foot to the top plate of the 4K shields. 41
4.4 2-Stage Cell 42
4.5 Disassembled 2-Stage Cell showing (from left to right) the cell back with helium line entry, 1/8" spacer, diffuser, 1/2" spacer, main cell body with snorkel and glass clamps above and target holder and glass clamp below, first stage aperture, round spacers, second stage body, second stage aperture, and finally the mesh holder. 46
4.6 Unit controller helium flow characterization 47
4.7 40K and first of two 4K copper thermal bobbins, connected by a stainless steel piece for thermal insulation. Helium flows in from the top right copper tubing and continues down into the cell. 48
4.8 Example Yb cooling by buffer gas collisions deduced from doppler broadening of in-cell absorption lines for times after ablation. Ablation occurs at $t = 0$ ms. 50

5.1 Comparison between utilization of a Doppler fit (red) and a Voigt fit (green) when fitting absorption data (blue) for line centers. 55
5.2 Comparison between Yb absorption signals. The left plot is an overlay of a typical absorption signal (blue) with the power fluctuations of the SHG cavity. The surface plots are a 3D representation of a sample Yb spectroscopy without (left) and with (right) blue-noise subtraction to illustrate the smoothing benefit of this blue-noise subtraction. 59
5.3 An estimation of the structure of the Q-forest (unresolved overlap of Q(0), Q(1), Q(2), etc). Shown is an overlay of preliminary fluorescence data provided by the McCarron lab at the University of Connecticut (green) with the aggregate simulated fluorescence at around 2.5 K (red) of the strongest Q-forest lines (vertical blue lines). 60
5.4 Absorption signals for the $X^1\Sigma^+(\nu = 0) \rightarrow A^1\Pi(\nu' = 0)$ manifold Q (a), R (b), and P (c) branches and $X^1\Sigma^+(\nu = 1) \rightarrow A^1\Pi(\nu' = 1)$ manifold (d). Data (blue) is shown after a moving 3-point average has been applied. A simulated spectrum (red) created with the molecular constants obtained from fitting the P and R branches is plotted over the data. Theoretical line center calculations (black) are labeled according to J of the $X^1\Sigma^+$ for the $Al^{35}Cl$ (solid) and $Al^{37}Cl$ (dashed) isotopologues. 61
5.5 Monte-Carlo simulation to determine the error from fitting the mass-reduced Dunham coefficients. 63
5.6 Franck-Condon factors, $f_{\nu,\nu'}$, inferred from molecular constants and simple harmonic oscillator wave functions for $\nu' = 0, 1$ transitions. 65
5.7 Fit (red) for in-cell rotational temperature to line strength data (blue) for the P branch of the X state of AlCl. The fit shown here yields a rotational temperature of 8.3(4) K. 66

6.1 A precursor target that has reacted with moisture in the air. The white half of the target was an $AlCl_3$ pellet. 69

6.2 Chemical structure for aluminum phthalocyanine chloride. This organic compound was explored as a precursor due to the existence of an Al-Cl bond, however all the carbon and nitrogen renders this organic not viable for AlCl production via ablation. 70
6.3 Laser setup schematic for the target study. Flip mirrors are added the the existing setup to allow for multiple configurations. Configuration (1) directs the Ti:Sapph output, set to 767 nm, through the cell to measure K absorption. Configuration (2) directs the output of the SHG cavity through the cell to observe Al at 395 nm. Configuration (3) uses the full THG system detailed above to observe AlCl at 261.5 nm. 72
6.4 A Sample data set including four sub-targets with Al:KCl molar ratios 10:1, 8:1, 5:1, and 1:4 (top left, bottom left, top right, bottom right). From left to right, the images are ALD absorption images of AlCl at 261.5 nm, Al at 395 nm, and K at 767 nm. Each pixel represents the amount of absorption at a location on the target. 72
6.5 A photo of a used target that had recently been removed from the dewar. You can clearly see the shiny features near where the three targets meet. We deduce that this must be aluminum that has recondensed onto the surface. 73

7.1 A photo of the installed Zeeman slower assembly. The dewar can be seen on the right and the UHV chamber can be seen on the left. 75
7.2 A simulation of the Zeeman slower magnetic field through the plane of the magnets. You can clearly see here that some regions are appropriately uniform, however at the ends of the slower the field direction depends on distance from the beam axis. 77
7.3 On-axis magnetic field intensity comparison between the simulated field (blue) and the ideal slower profile (red dash). 78
7.4 MOT coil assembly just prior to being installed in the UHV chamber. . . . 79
7.5 Cross section of the simulated MOT coil magnetic field through the XZ plane. Due to the symmetry of the system, these field lines will be approximately the same (up to deviations from the concentric-loop model) for any angle of rotation around the z-axis. 80
7.6 MOT Laser Setup 81
7.7 A photo of the resistive heating Yb oven used to test the MOT coils. 82
7.8 The University of California, Riverside's first MOT. This MOT was trapped by Zeeman slowing a hot ytterbium beam from an oven source. 83

8.1 Sketch of how to upgrade the single-pass configuration into a possible bowtie resonance cavity configuration. 87
8.2 Sketch of how to use a SHG cavity to frequency-double a Vexlum laser. . . 88

List of Tables

1.1 A summary of molecules that have been either laser-slowed or trapped by the community. 2

2.1 Quantum vectors and numbers used throughout the following derivations. . 7

5.1 The fitted Dunham coefficients obtained from individually fitting the line centers for the two isotopologues of AlCl. 62
5.2 The fitted mass-reduced Dunham coefficients for AlCl with and without the inclusion of a Born-Oppenheimer-breakdown coefficient, $\Delta_{00}^{\mathrm{Cl}}$. 62

A.1 Universal Constants of Nature 97
A.2 Nuclear properties for Al and Cl obtained from Appendix B of Brown and Carrington. MM is the nuclear magnetic moment and EQM is the electric quadrupole moment. Nuclear g-factors were obtained from easyspin.org. . . 97
A.3 A summary of AlCl constants. 98

B.1 Spherical tensors for rank 1 (vector) and 2 (tensor) operators. 99
B.2 Useful spherical tensors for an angular momentum operator **J** 100

C.1 List of Devices Controlled by Artiq. PD is short for "photodiode". 105
C.2 Scan_Single_Laser.py Parameters 106
C.3 raster_target.py Parameters 107

D.1 $Al^{37}Cl$ line center frequencies for the $X^1\Sigma^+ \rightarrow A^1\Pi$ taken from a least-square fit of the observed lines to a Voigt function. Because the Q branch has multiple overlapping lines, we report the frequency of peak absorption for the Q branch observations. Included for completeness[15]. 109
D.2 $Al^{35}Cl$ line center frequencies for the $X^1\Sigma^+ \rightarrow A^1\Pi$ taken from a least-square fit of the observed lines to a Voigt function. Because the Q branch has multiple overlapping lines, we report the frequency of peak absorption for the Q branch observations. Included for completeness[15]. 110

Chapter 1

Introduction

The laser is arguably the most important experimental development of the twentieth century for quantum mechanics. The ability to precisely control wavelengths and phases of light waves allow for exploration and control of nature on the atomic level. The dawn of the twenty-first century heralded a new era as the first atoms were cooled to the point of Bose-Einstein condensation, proving that novel quantum states could be realized in the lab environment with the proper application of lasers and willpower.

1.1 Cold Molecules

Following the enormous successes with laser cooling and trapping neutral atoms, researchers turned to apply the same techniques to molecules. Molecules have vibrational and rotational modes, leading to a rich internal structure that offers a platform for studying many different areas of novel physics[37, 20]. There are ongoing experiments using precision measurements to study physics, including theories beyond the standard model[1, 19, 10, 28,

Diatomics	SrF [8] YO [14] CaF [5, 49, 52] AlF [48, 18] BaF [13, 4] BaH [27] Cs_2 [7] MgF [54] RaF [26] TiO [47] TlF [42] YbF [35]
Polyatomics	CaOH [9] $CaOCH_3$ [40] SrOH [29] YbOH [6, 30]

Table 1.1: A summary of molecules that have been either laser-slowed or trapped by the community.

62, 24, 43, 2]. This sort of measurement is possible in a molecule because the electric field gradients inside a molecule are very larger at such a small length-scale inside the molecule, allowing for sensitivity to weak couplings to possible non-standard-model physics. Another application for cold molecules is the study of controlled chemical reactions[31, 41, 58, 44]. Cold molecules also have the possibility to be exploited for quantum computation[17, 59, 61] and quantum simulation[11, 39].

Many different molecules are being pursued as summarized in Tab. 1.1. The keen eye will notice a many of these molecules are alkali metals or alkaline earths fluorides. The reason for this is that the laser slowing methodology is easiest to apply to molecules that have an electronic structure that behaves in a way similar to an atom, that is a sole, single, highest-energy electron is undergoing optical transitions.

1.2 Interest in AlCl

A goal in the molecule-cooling community is to find the molecule that is most amenable to laser-cooling. AlCl was selected as a candidate for laser cooling because it is predicted to have favorable Franck-Condon factors of 99.88%-99.93% [33, 46, 55, 51] and a relatively short lifetime for the cooling transition of ≈5 ns. This means that not only will excited electrons quickly decay back into the ground electronic state, but they are very likely to not change vibrational state during these optical cycles. Such a change in vibrational state would result in that molecule not being receptive to excite with the same frequency laser.

In addition to being predicted to have favorable optical-cycling properties, there are a few other reasons why AlCl is interesting to study. AlCl could conceivably be used as a source for producing cold chlorine. Chlorine itself is not amenable to laser cooling, however one could use a cooling scheme by which AlCl is first laser cooled and then a 108 nm dissociation photon could separate the chlorine from the aluminum, thus creating a source of cold chlorine similar to the proposed method of cold fluorine production from BeF[32]. AlCl can also be found in rocket plumes[38] and in industrial reducing of photovoltaic-grade silicone (99.9999%)[56, 57] as

$$2\mathrm{AlCl}_{(g)} + \mathrm{SiCl}_{4(g)} \rightarrow \mathrm{Si}_{(s)} + 2\mathrm{AlCl}_{3(g)} \tag{1.1}$$

I mentioned above that cold molecules could be a platform for quantum computation. Specifically in AlCl, a possible scheme for computation would be to utilize the $X^1\Sigma^+ \leftrightarrow A^1\Pi$ transition for cooling and then switch to the $X^1\Sigma^+ \leftrightarrow a^3\Pi$ transition as a qubit. Qubits are required to be relatively long-lived, otherwise you will lose state coher-

ence long before any operation could be performed. The ≈5 ns lifetime of the $A^1\Pi$ state is convenient for slowing, however the $a^3\Pi$ state's lifetime is ≈1.5 ms (≈100 Hz linewidth) making it more useful for quantum computation experiments.

1.2.1 Variation of $\dot{\mu}$

One possible application of precision spectroscopy on AlCl is setting upper limits on time variations of the proton-to-electron mass ratio, μ (a phenomena predicted by some cosmological models). AlCl could be a candidate for such a test as it has been observed in the circumstellar envelope of carbon-rich stars, such as IRC+10216 [50, 12, 3, 60, 53]. In a manner similar to one presented for CO [16], AlCl could serve as a platform for such a measurment.

From [16], the $\dot{\mu}$ sensitivity constant of an absorption line i is given as

$$K_\mu^i = \frac{\mu}{E_e^i - E_g^i}\left(\frac{\partial E_e^i}{\partial \mu} - \frac{\partial E_g^i}{\partial \mu}\right) \tag{1.2}$$

where e and g denoted the excited and ground states respectively and the energies, E_e^i and E_g^i are expressed in terms of the Dunham expansion,

$$E^i = \sum_{k,l} Y_{kl}^i (\nu + 1/2)^k \left[J(J+1) - \Lambda^2\right]^l . \tag{1.3}$$

I fully explain the Dunham expansion in a later section, so I will not spend more time on it here. The μ dependence of this energy is contained in the Dunham coefficients, Y_{kl}^i, as

$$Y_{kl} \propto \mu^{-(l+k/2)} \tag{1.4}$$

such that the partial derivative only applies to Y_{kl}. This means that

$$\frac{\partial Y_{kl}^i}{\partial \mu} \approx -\frac{Y_{kl}^i}{\mu}(l + k/2) \tag{1.5}$$

and thus the full μ-dependent part of the sensitivity constant can be given as

$$\mu\frac{\partial E^i}{\partial \mu} = \sum_{kl} -Y^i_{kl}(l+k/2)(\nu+1/2)^k \left[J(J+1)-\Lambda^2\right]^l . \tag{1.6}$$

Plugging Eq. (1.3) and Eq. (1.6) back into Eq. (1.2) yields the sensitivity constant for a particular absorption line. The $X^1\Sigma^+ \rightarrow A^1\Pi$ transition itself is not the best candidate for performing such as measurement as the sensitivity constant is inversely proportional to the transition wavelength, however $X^1\Sigma^+ \rightarrow X^1\Sigma^+$ or $A^1\Pi \rightarrow A^1\Pi$ transitions would have a much higher sensitivity.

1.3 Is AlCl A Viable Candidate For Slowing?

This thesis will investigate the $A^1\Pi$ state of AlCl and assess the viability of laser cooling AlCl. This thesis will first present a detailed description of the AlCl hamiltonian terms for the $X^1\Sigma^+$ and $A^1\Pi$ that are relevant for laser cooling. I will then discuss the UV laser setup and the AlCl cryogenic-buffer-gas beam-source. I will then present absorption spectroscopy on the $X^1\Sigma^+ \rightarrow A^1\Pi$ transition including estimates of the Franck-Condon factors[15]. I will briefly discuss the precursor target that is ablated to produce AlCl[34]. I will present a description of the magneto-optical-trap mechanism and its testing on atomic ytterbium. I will conclude with a brief discussion of the remaining barriers to achieving slowing and trapping.

Chapter 2

AlCl Hamiltonian

To be able to properly analyze any observed spectra and to produce useful simulations it is necessary to generate the set of dominant Hamiltonian terms. In principle, there are many more terms than are discussed here, however all omitted terms have energy splittings <100 kHz. Due to the natural line width of the transition being on the order of 32 MHz, splittings of this order will be unresolved.

2.1 Electronic Structure

The two electronic states of interest to this work are $X^1\Sigma^+$ and $A^1\Pi$ with an energy spacing of ≈261 nm. The X designates that $X^1\Sigma^+$ is the ground electronic state, and the A designates that $A^1\Pi$ is the first strong excited state. There does exist a triplet state, $a^3\Pi$, between X and A, however since transitions to this state from a singlet state such as $X^1\Sigma^+$ or $A^1\Pi$ requires flipping an electron spin, dipole transitions to this triplet state are very weak. At energies higher than $A^1\Pi$, there exist additional higher electronic

Symbol	Range	Description
R	0, 1, 2, 3...	Molecular Rotation Angular Momentum
Λ	$\Sigma = 0$, $\Pi = 1$	Projection of Electron Angular Momentum along IA
J	$\lvert R - \Lambda \rvert, \lvert R - \Lambda \rvert + 1, ...$	$\mathbf{J} = \mathbf{R} + \mathbf{\Lambda}$ (only because $\Sigma = 0$)
F_1	$\lvert J - I_1 \rvert ... J + I_1$	$\mathbf{F}_1 = \mathbf{J} + \mathbf{I}_1$
F	$\lvert F_1 - I_2 \rvert ... F_1 + I_2$	$\mathbf{F} = \mathbf{F}_1 + \mathbf{I}_2$
M	$-F ... F$	$\langle F_z \rangle$

Table 2.1: Quantum vectors and numbers used throughout the following derivations.

states ($B^1\Sigma^+$, etc). In these molecular term symbols, Σ, Π, Δ... denotes the value of the projection (Λ) of the total electron orbital angular momentum ($\mathbf{L}$) onto the internuclear axis to be 0, 1, 2... respectively. This projection is used when coupling to other angular momentum as $\mathbf{L}$ precesses quickly around the inter-nuclear axis leaving only contributions from the component aligned with the inter-nuclear axis. In the case of a $^1\Sigma$ state the angular momentum is that of a rigid rotor and in a $^1\Pi$ state the angular momentum is characterized as that of a symmetric top. The superscript denotes the state's total spin multiplicity with the superscript being $2S + 1$ where S is the total electron spin. For both of the electronic states explored in this work, the superscript is 1, meaning that they are both singlet states ($S = 0$).

In addition to electronic states, molecules have vibrational (quantum number ν) and rotational states (quantum number R). These additional states increase the complexity of the energy structure.

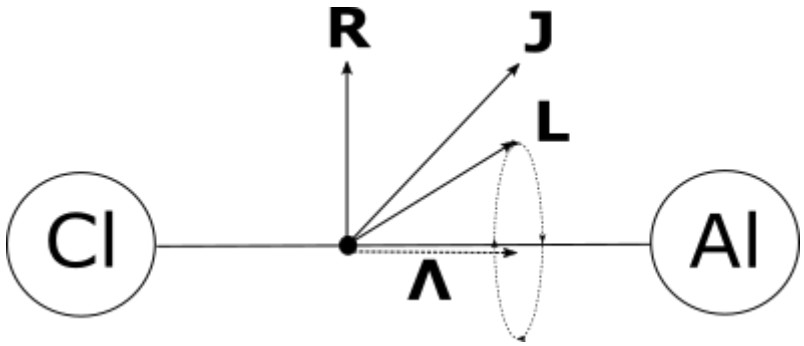

Figure 2.1: Angular momentum diagram for the singlet states of AlCl. Since **L** precesses rapidly about the inter-nuclear axis, the component, $\mathbf{\Lambda}$, of **L** along this axis is coupled to the molecular rotation, **R** to obtain the total angular momentum $\mathbf{J} = \mathbf{R} + \mathbf{\Lambda}$. All hyperfine interactions are excluded from this figure.

2.2 Basis Sets

Due to the singlet nature of the $X^1\Sigma^+$ and $A^1\Pi$ states, the usual Hund's coupling case consideration does not apply. Instead, in the case of the $X^1\Sigma^+$, **J** is pure molecular rotation angular momentum, and in the $A^1\Pi$, the symmetric top treatment applies as the molecules rotation is coupled to the projection of the electron's angular momentum onto the internuclear axis.

2.2.1 Primitive Basis Set

When computing matrix elements, the angular momentum quantum state is expressed in terms of the primitive basis set. This state vector is written as

$$|\eta, \Lambda, J, F_1, F, M\rangle \tag{2.1}$$

where η includes all other quantum numbers, such as the vibrational quantum number, ν, and the other hyperfine quantum numbers are detailed in Tab. 2.1.

2.2.2 Parity-Conserved Basis Set

It is trivial to construct the parity-conserved basis set from the primitive basis set as it expressed as a linear combination of primitive bases with alternating sign of Λ.

$$|\eta, \Lambda, J, F_1, F, M, \pm\rangle = \frac{1}{\sqrt{2}} |\eta, \Lambda, J, F_1, F, M\rangle \pm (-1)^p \frac{1}{\sqrt{2}} |\eta, -\Lambda, J, F_1, F, M\rangle \tag{2.2}$$

with $p = J + s$ where s is even for $^1\Sigma^+$ and $\Lambda > 0$. This means that for both the $X^1\Sigma^+$ and $A^1\Pi$ states s can be left to be zero, simplifying the parity conserved basis set definition to be

$$|\eta, \Lambda, J, F_1, F, M, \pm\rangle = \frac{1}{\sqrt{2}} |\eta, \Lambda, J, F_1, F, M\rangle \pm (-1)^J \frac{1}{\sqrt{2}} |\eta, -\Lambda, J, F_1, F, M\rangle \tag{2.3}$$

with the relative sign only being determined by J. Since the only difference between the primitive state vector components is the sign of Λ, any term that is diagonal in Λ will be the same in both the primitive and the parity-conserved basis sets, with only terms such as H_Λ depending on the parity of the state. Due to parity selection rules, parity must change during a dipole transition, dictating which parity states are utilized in the transition based on which rotational states are involved. For example, the $X^1\Sigma^+(\nu = 0, J = 1) \rightarrow A^1\Pi(\nu' = 0, J' = 1)$ Q-branch transition would be to even-parity in the $A^1\Pi$ state as $X^1\Sigma^+(\nu = 0, J = 1)$ has odd-parity.

2.3 $X^1\Sigma^+$ Hamiltonian

The Hamiltonian for the $X^1\Sigma^+$ state is expressed as a collection of its dominant terms. In principle, there could be further higher-order terms, however they are too small to be measured and resolved. The electro-ro-vibrational component of the $X^1\Sigma^+$ state

hamiltonian (H_0) has been extensively studied via $X^1\Sigma^+ \rightarrow X^1\Sigma^+$ microwave (rotational) and infrared (vibrational) spectroscopy[21]. The strongest hyperfine term, and the only one that has any existing constant knowledge is the electric quadrupole term (H_Q). [CITE]. Because the hyperfine structure of the $X^1\Sigma^+$ spans only about 11-12 MHz, $X^1\Sigma^+ \leftrightarrow A^1\Pi$ transitions, which have a width of about 32 MHz will render the $X^1\Sigma^+$ unresolved. This means that every $X^1\Sigma^+ \leftrightarrow A^1\Pi$ transition has access to the entire $X^1\Sigma^+$ state, governed by selection rules and dipole transition moments. The dominant terms of the hyperfine hamiltonian for the $X^1\Sigma^+$ state can be expressed as

$$H = H_0 + H_Q + H_Z \tag{2.4}$$

where H_Z is the Zeeman term that depends on the strength of an applied magnetic field.

2.4 $A^1\Pi$ Hamiltonian

The Hamiltonian for the $A^1\Pi$ state is also expressed as a collection of its dominant terms. Three of these terms, H_0, H_Q, and H_Z are analogous to terms in the $X^1\Sigma^+$ hamiltonian. The hyperfine term, H_{HF} and the lambda-doubling term, H_Λ both arise as a result of the Π nature of the $A^1\Pi$ state, i.e. the component of the electron-angular-momentum, Λ, that is projected along the internuclear axis, is nonzero. The dominant terms of the hyperfine hamiltonian for the $A^1\Pi$ state can be expressed as

$$H = H_0 + H_\Lambda + H_{HF} + H_Q + H_Z \tag{2.5}$$

2.5 Dunham Expansion

The Dunam expansion is a concise notation for describing the electronic, vibrational, and rotational energies of a molecule. The Dunham coefficients are defined such that the energy of a particular ro-vibrational state of a particular electronic state is expressed as

$$E(\nu, J, \Lambda) = \sum_{k,l} Y_{kl}(\nu + 1/2)^k [J(J+1) - \Lambda^2]^l \tag{2.6}$$

where the quantum numbers are as defined in Table 2.1. The dependence of the Dunham coefficients on the reduced mass of AlCl can be explicitly stated as

$$Y_{kl} = \mu^{-(k+2l)/2} \left(1 + \frac{m_e}{m_{\mathrm{Cl}}} \Delta_{kl}^{\mathrm{Cl}}\right) U_{kl} \tag{2.7}$$

where μ is the reduced mass of AlCl in atomic mass units, m_e is the electron rest mass, m_{Cl} is the mass of the chlorine nucleus, U_{kl} are the mass-reduced Dunham coefficients, and Δ_{kl}^{C} are the Born-Oppenheimer breakdown factors. These breakdown factors arise due to the reduced-mass dependence only being valid under the Born-Oppenheimer approximation that the order of magnitude of the electronic, vibrational, and rotational energies are different enough that they can be treated as independent. This empirical model becomes the expression of H_0,

$$H_0 = \delta_{MM'} \delta_{FF'} \delta_{F_1 F_1'} \delta_{JJ'} \delta_{\Lambda\Lambda'} E(\nu, J, \Lambda) \tag{2.8}$$

2.6 Λ-Doubling

The H_Λ term of the $A^1\Pi$ hamiltonian leads to Λ-doubling, a phenomena that splits each rotational state into two, based on the parity of the state. The Λ-doubling term for

singlet states is expressed as

$$H_\Lambda = -\sum_{q=\pm 1} e^{-2iq\phi} q T^2_{2q}(\mathbf{J},\mathbf{J}) \tag{2.9}$$

for which matrix elements can readily be calculated as

$$\begin{aligned}
\left\langle \eta,\Lambda,J,F_1,F,M \middle| -\sum_{q=\pm 1} e^{-2iq\phi} q T^2_{2q}(\mathbf{J},\mathbf{J}) \middle| \eta,\Lambda',J',F_1',F',M' \right\rangle = \\
\delta_{MM'}\delta_{FF'}\delta_{F_1F_1'} \left\langle \eta,\Lambda,J \middle| -\sum_{q=\pm 1} e^{-2iq\phi} q T^2_{2q}(\mathbf{J},\mathbf{J}) \middle| \eta,\Lambda',J' \right\rangle = \\
\delta_{MM'}\delta_{FF'}\delta_{F_1F_1'} \sum_{q=\pm 1} \delta_{\Lambda\Lambda'\mp 2} \frac{q}{2\sqrt{6}} (-1)^{J-\Lambda} \begin{pmatrix} J & 2 & J \\ -\Lambda & -2q & \Lambda' \end{pmatrix} \\
\sqrt{(2J-1)2J(2J+1)(2J+2)(2J+3)}
\end{aligned} \tag{2.10}$$

This simplification arise from the fact that

$$\left\langle \Lambda = \pm 1 \middle| e^{\pm 2i\phi} \middle| \Lambda = \mp 1 \right\rangle = -1 \tag{2.11}$$

Care should be taken to distinguish the coordinate q from the doubling constant q. In the final form, the sum is over the coordinate, of which the last remaining dependence is in the Wigner-3j term. The q that is divided by $2\sqrt{6}$ is the doubling constant.

2.7 Electric Quadrupole Term

The electric quadrupole term, H_Q, has previously been found to be the dominant hyperfine term for $X^1\Sigma^+$[23, 22]. Additionally, the quadrupole term is found to be significant, albiet weak, in the $A^1\Pi$ state in the similar structure of AlF, and as such can be

expected to be present in AlCl[48]. The form of this term is

$$H_Q = -e \sum_{\alpha} T^2(\nabla \mathbf{E}_\alpha) \cdot T^2(\mathbf{Q}_\alpha) \tag{2.12}$$

where $\alpha = 1$ indicates the Al nucleus and $\alpha = 2$ indicates the Cl nucleus. The explicit forms for each nuclei are derived here for completeness.

$$\begin{gathered}
\left\langle \eta, \Lambda, J, F_1, F, M \middle| -eT^2(\nabla \mathbf{E}_1) \cdot T^2(\mathbf{Q}_1) \middle| \eta, \Lambda', J', F_1', F', M' \right\rangle = \\
\delta_{MM'} \delta_{FF'} \left\langle \eta, \Lambda, J, F_1 \middle| -eT^2(\mathbf{Q}_1) \cdot T^2(\mathbf{Q}_1) \middle| \eta, \Lambda', J', F_1' \right\rangle = \\
-e \delta_{MM'} \delta_{FF'} \delta_{F_1 F_1'} (-1)^{J'+F_1+I_1} \begin{Bmatrix} I_1 & J' & F_1 \\ J & I_1 & 2 \end{Bmatrix} \left\langle \eta, \Lambda, J \middle|\middle| T^2(\nabla \mathbf{E}_1) \middle|\middle| \eta, \Lambda', J' \right\rangle \left\langle I_1 \middle|\middle| T^2(\mathbf{Q}_1) \middle|\middle| I_1 \right\rangle
\end{gathered} \tag{2.13}$$

The reduced matrix elements can be solved for individually.

$$\left\langle I_1 \middle|\middle| T^2(\mathbf{Q}_1) \middle|\middle| I_1 \right\rangle = \frac{Q}{2} \begin{pmatrix} I_1 & 2 & I_1 \\ -I_1 & 0 & I_1 \end{pmatrix}^{-1} \tag{2.14}$$

is a constant for all states, as nothing in our experiment changes the spin of the nuclei. The other reduced matrix element requires using a Wigner rotation term, $\mathcal{D}^{(2)}_{\cdot q}(\omega)^*$, to express the operator as a sum over molecule-fixed coordinates, q.

$$\begin{gathered}
\left\langle \eta, \Lambda, J \middle|\middle| T^2(\nabla \mathbf{E}_1) \middle|\middle| \eta, \Lambda', J' \right\rangle = \\
\left\langle \eta, \Lambda, J \middle|\middle| \sum_q \mathcal{D}^{(2)}_{\cdot q}(\omega)^* T^2_q(\nabla \mathbf{E}_1) \middle|\middle| \eta, \Lambda', J' \right\rangle = \\
\sum_q (-1)^{J-\Lambda} \sqrt{(2J+1)(2J'+1)} \begin{pmatrix} J & 2 & J' \\ -\Lambda & q & \Lambda' \end{pmatrix} \left\langle \eta, \Lambda \middle| T^2_q(\nabla \mathbf{E}_1) \middle| \eta, \Lambda' \right\rangle
\end{gathered} \tag{2.15}$$

In the case of $q = 0$,

$$\left\langle \eta, \Lambda \middle| T^2_{q=0}(\nabla \mathbf{E}) \middle| \eta, \Lambda \right\rangle = -\frac{q_0}{2} \tag{2.16}$$

The q_0 term is the only non-zero quadrupole term for $X^1\Sigma^+$. However for $A^1\Pi$ the $q = \pm 2$ term connects parities as

$$\left\langle \eta, \Lambda = \pm 1 \middle| T^2_{q=\pm 2}(\nabla \mathbf{E}) \middle| \eta, \Lambda = \mp 1 \right\rangle = -\frac{q_2}{2\sqrt{6}} \tag{2.17}$$

Substituting these back into Eq. (2.13), we obtain

$$\begin{aligned}
&\left\langle \eta, \Lambda, J, F_1, F, M \middle| -eT^2(\nabla \mathbf{E}_1) \cdot T^2(\mathbf{Q}_1) \middle| \eta, \Lambda', J', F_1', F', M' \right\rangle = \\
&\delta_{MM'}\delta_{FF'}\delta_{F_1F_1'}(-1)^{J+J'+F_1+I_1-\Lambda} \begin{Bmatrix} I_1 & J' & F_1 \\ J & I_1 & 2 \end{Bmatrix} \begin{pmatrix} I_1 & 2 & I_1 \\ -I_1 & 0 & I_1 \end{pmatrix}^{-1} \times \\
&\sqrt{(2J+1)(2J'+1)} \left[\frac{(eQq_0)_1}{4} \begin{pmatrix} J & 2 & J' \\ -\Lambda & 0 & \Lambda \end{pmatrix} + \frac{(eQq_2)_1}{4\sqrt{6}} \begin{pmatrix} J & 2 & J' \\ -\Lambda & \pm 2 & \Lambda' \end{pmatrix} \right]
\end{aligned} \tag{2.18}$$

which is the electric quadrupole term for the aluminum nucleus. The derivation for the chlorine nucleus is very similar.

$$\begin{aligned}
&\left\langle \eta, \Lambda, J, F_1, F, M \middle| -eT^2(\nabla \mathbf{E}_2) \cdot T^2(\mathbf{Q}_2) \middle| \eta, \Lambda', J', F_1', F', M' \right\rangle = \\
&-\delta_{FF'}\delta_{MM'}e(-1)^{F_1'+F+I_2} \begin{Bmatrix} I_2 & F_1' & F \\ F_1 & I_2 & 2 \end{Bmatrix} \left\langle \eta, \Lambda, J, F_1 \middle|\middle| T^2(\nabla \mathbf{E}_2) \middle|\middle| \eta, \Lambda, J', F_1' \right\rangle \left\langle I_2 \middle|\middle| T^2(\mathbf{Q}_2) \middle|\middle| I_2 \right\rangle
\end{aligned} \tag{2.19}$$

where the first reduced matrix element can be further decoupled as

$$\begin{aligned}
&\left\langle \eta, \Lambda, J, F_1 \middle|\middle| T^2(\nabla \mathbf{E}_2) \middle|\middle| \eta, \Lambda, J', F_1' \right\rangle = \\
&(-1)^{F_1'+J+I_1+2}\sqrt{(2F_1+1)(2F_1'+1)} \begin{Bmatrix} J' & F_1' & I_1 \\ F_1 & J & 2 \end{Bmatrix} \left\langle \eta, \Lambda, J \middle|\middle| T^2(\nabla \mathbf{E}_2) \middle|\middle| \eta, \Lambda, J' \right\rangle
\end{aligned} \tag{2.20}$$

and then the results from Eq. (2.15) through Eq. (2.17) are the same for the chlorine nucleus. Similarly, the result in Eq. (2.14) is analogous for the chlorine nucleus with

$$\left\langle I_2 \middle|\middle| T^2(\mathbf{Q}_2) \middle|\middle| I_2 \right\rangle = \frac{Q}{2} \begin{pmatrix} I_2 & 2 & I_2 \\ -I_2 & 0 & I_2 \end{pmatrix}^{-1} \tag{2.21}$$

Substituting these reduced matrix elements back into Eq. (2.19) yields the full form of the quadrupole term for the chlorine nucleus

$$\begin{aligned} &\left\langle \eta, \Lambda, J, F_1, F, M \middle| -eT^2(\nabla \mathbf{E}_2) \cdot T^2(\mathbf{Q}_2) \middle| \eta, \Lambda', J', F_1', F', M' \right\rangle = \\ &\delta_{FF'}\delta_{MM'}(-1)^{2F_1'+F+I_2+I_1-\Lambda}\sqrt{(2J+1)(2J'+1)(2F_1+1)(2F_1'+1)} \begin{Bmatrix} I_2 & F_1' & F \\ F_1 & I_2 & 2 \end{Bmatrix} \times \\ &\begin{Bmatrix} J' & F_1' & I_1 \\ F_1 & J & 2 \end{Bmatrix} \begin{pmatrix} I_2 & 2 & I_2 \\ -I_2 & 0 & I_2 \end{pmatrix}^{-1} \left[\frac{(eQq_0)_2}{4} \begin{pmatrix} J & 2 & J' \\ -\Lambda & 0 & \Lambda \end{pmatrix} + \frac{(eQq_2)_2}{2\sqrt{6}} \begin{pmatrix} J & 2 & J' \\ -\Lambda & \pm 2 & \Lambda' \end{pmatrix} \right] \end{aligned} \tag{2.22}$$

Previous experimental work has been done to estimate the value of eQq_0 for $X^1\Sigma^+$ for both nuclei[23, 22] which measures these constants at -30.4081 MHz for the aluminum nucleus and -8.8290 MHz for the chlorine nucleus. To my knowledge, this is the most recent measurement of these constants.

2.8 Hyperfine Term

The coupling of the electron orbital angular momentum to the spins of the nuclei is expected to be the dominant term for $A^1\Pi$ hyperfine structure. This expectation arises from observations performed on the similar structure in AlF[48] and is confirmed by preliminary

results from the McCarron group at the University of Connecticut. This hyperfine term can be expressed as

$$H_{HF} = \sum_{\alpha} a_{\alpha} T^1(\mathbf{L}) \cdot T^1(\mathbf{I}_{\alpha}) \tag{2.23}$$

where $\alpha = 1, 2$ corresponds to the aluminum and chlorine nuclei respectively. The matrix elements of H_{HF} can be calculated as

$$\begin{aligned} &\left\langle \eta, \Lambda, J, F_1, F, M \middle| a_1 T^1(\mathbf{L}) \cdot T^1(\mathbf{I}_1) \middle| \eta, \Lambda', J', F_1', F', M' \right\rangle = \\ &\delta_{FF'} \delta_{MM'} a_1 \left\langle \eta, \Lambda, J, F_1 \middle| T^1(\mathbf{L}) \cdot T^1(\mathbf{I}_1) \middle| \eta, \Lambda', J', F_1' \right\rangle = \\ &\delta_{FF'} \delta_{MM'} \delta_{F_1 F_1'} (-1)^{J'+F_1+I_1} \begin{Bmatrix} I_1 & J' & F_1 \\ J & I_1 & 1 \end{Bmatrix} \left\langle \eta, \Lambda, J \middle|\middle| a_1 T^1(\mathbf{L}) \middle|\middle| \eta, \Lambda', J' \right\rangle \left\langle I_1 \middle|\middle| T^1(\mathbf{I}_1) \middle|\middle| I_1 \right\rangle \end{aligned} \tag{2.24}$$

with the reduced matrix element

$$\left\langle I_1 \middle|\middle| T^1(\mathbf{I}_1) \middle|\middle| I_1 \right\rangle = \sqrt{I_1(I_1+1)(2I_1+1)} \tag{2.25}$$

and

$$\left\langle \eta, \Lambda, J \middle| \, |a_1 T^1(\mathbf{L})| \, \middle| \eta', \Lambda', J' \right\rangle = \tag{2.26}$$

$$\left\langle \eta, \Lambda, J \middle| \, |a_1 \sum_q \mathcal{D}^{(1)}_{\cdot q}(\omega)^* T^1_q(\mathbf{L})| \, \middle| \eta', \Lambda', J' \right\rangle = \tag{2.27}$$

$$\sum_q (-1)^{J-\Lambda} \begin{pmatrix} J & 1 & J' \\ -\Lambda & q & \Lambda \end{pmatrix} \sqrt{(2J+1)(2J'+1)} \left\langle \eta, \Lambda \middle| \, a_1 T^1_q(\mathbf{L}) \, \middle| \eta', \Lambda' \right\rangle \tag{2.28}$$

for which we can set $q = 0$. This yields a full form of the hyperfine term for the aluminum nucleus to be

$$\begin{aligned}\left\langle \eta, \Lambda, J, F_1, F, M \middle| a_1 T^1(\mathbf{L}) \cdot T^1(\mathbf{I}_1) \middle| \eta, \Lambda', J', F_1', F', M' \right\rangle = \\ \delta_{FF'}\delta_{F_1F_1'}\delta_{MM'} a_1 \Lambda (-1)^{J+J'+F_1+I_1-\Lambda} \times \\ \sqrt{I_1(I_1+1)(2I_1+1)(2J+1)(2J'+1)} \begin{Bmatrix} I_1 & J' & F_1 \\ J & I_1 & 1 \end{Bmatrix} \begin{pmatrix} J & 1 & J' \\ -\Lambda & 0 & \Lambda \end{pmatrix}\end{aligned} \tag{2.29}$$

In a similar manner the matrix element for the chlorine nucleus can be calculated to be

$$\begin{aligned}\left\langle \eta, \Lambda, J, F_1, F, M \middle| a_2 T^1(\mathbf{L}) \cdot T^1(\mathbf{I}_2) \middle| \eta, \Lambda', J', F_1', F', M' \right\rangle = \\ \delta_{FF'}\delta_{MM'} a_2 \Lambda (-1)^{2F_1'+F+I_2+I_1+1-\Lambda} \times \\ \sqrt{(2F_1+1)(2F_1'+1)(2J+1)(2J'+1)I_2(I_2+1)(2I_2+1)} \times \\ \begin{Bmatrix} I_2 & F_1' & F \\ F_1 & I_2 & 1 \end{Bmatrix} \begin{Bmatrix} J' & F_1' & I_1 \\ F_1 & J & 1 \end{Bmatrix} \begin{pmatrix} J & 1 & J' \\ -\Lambda & 0 & \Lambda \end{pmatrix}\end{aligned} \tag{2.30}$$

The values of a_1 and a_2 can be obtained from fitting the R(0) absorption line. Specifically this is the $X^1\Sigma^+(\nu = 0, J = 0) \rightarrow A^1\Pi(\nu' = 0, J' = 1)$ transition. Spectroscopy on this transition is particularly useful for determining $A^1\Pi$ hyperfine constants due due to the fact that $J = 0$. The $X^1\Sigma^+$ dominant hyperfine structure is the electric quadrupole term which is proportional to the wigner-3j term

$$\begin{pmatrix} J & 2 & J \\ -\Lambda & 0 & \Lambda \end{pmatrix} \tag{2.31}$$

Remembering that the top row of a wigner-3j term obeys a triangle relation, the sum of any two elements must be greater than the third, else the term computes to be zero. In

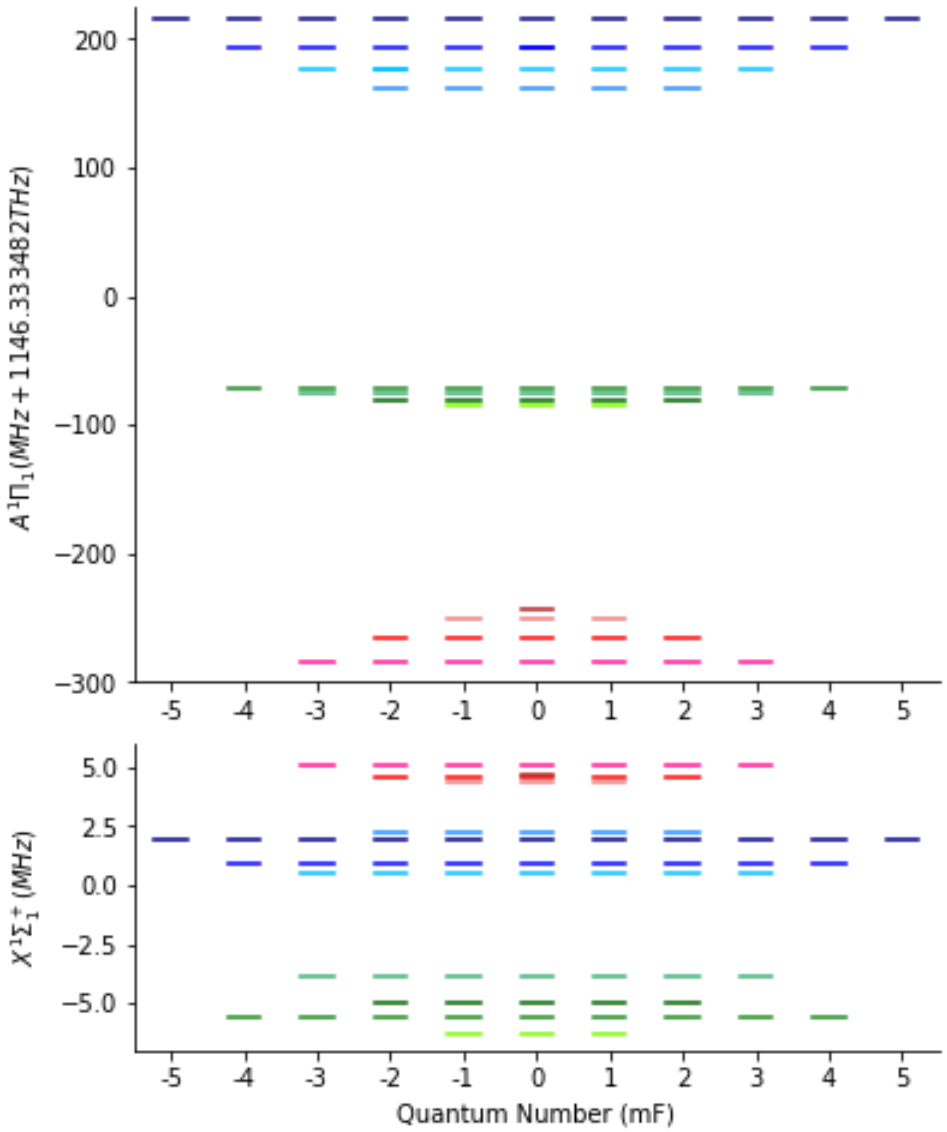

Figure 2.2: $X^1\Sigma^+$ and $A^1\Pi$ hyperfine states for $J = J' = 1$. Shades of red correspond to $F_1 = 3/2$, shades of green correspond to $F_1 = 5/2$, and shades of blue correspond to $F_1 = 7/2$.

the case of $J = 0$, the top row of this term doesn't satisfy the triangle rule, and thus the quadrupole term evaluates to zero. Explicitly, when $J = \Lambda = 0$,

$$\begin{pmatrix} J & 2 & J \\ -\Lambda & 0 & \Lambda \end{pmatrix} = (-1)^{J-\Lambda} \frac{2[3\Lambda^2 - J(J+1)]}{\sqrt{(2J-1)(2J)(2J+1)(2J+2)(2J+3)}} = 0 \tag{2.32}$$

Considering that any other hamiltonian terms are too small to lead to appreciable splitting, the ground state can be treated as a single state. All structure observed arrives from the $A^1\Pi$ state. During the fitting procedure, it became clear that there was a significant term missing. Since the electric quadrupole term is the next strongest term, it was also included in the fit. Both the $q = 0$ terms, depending on $(eQq_0)_1$ and $(eQq_0)_2$, are negligible, along with the $q = 2$ term for the chlorine nucleus, proportional to $(eQq_2)_2$. The dominant term is the $q = 2$ term for the aluminum nucleus, proportional to $(eQq_2)_1$. Including this term in the fit greatly improves the quality of the fit.

2.9 Zeeman Term

The Zeeman term of the hamiltonian, H_Z, is the term that interacts with an applied magnetic field. For the $X^1\Sigma^+$ state, the dominant terms are the interactions between the nuclear spins and the magnetic field. For the aluminum nucleus with g-factor g_{Al}, the

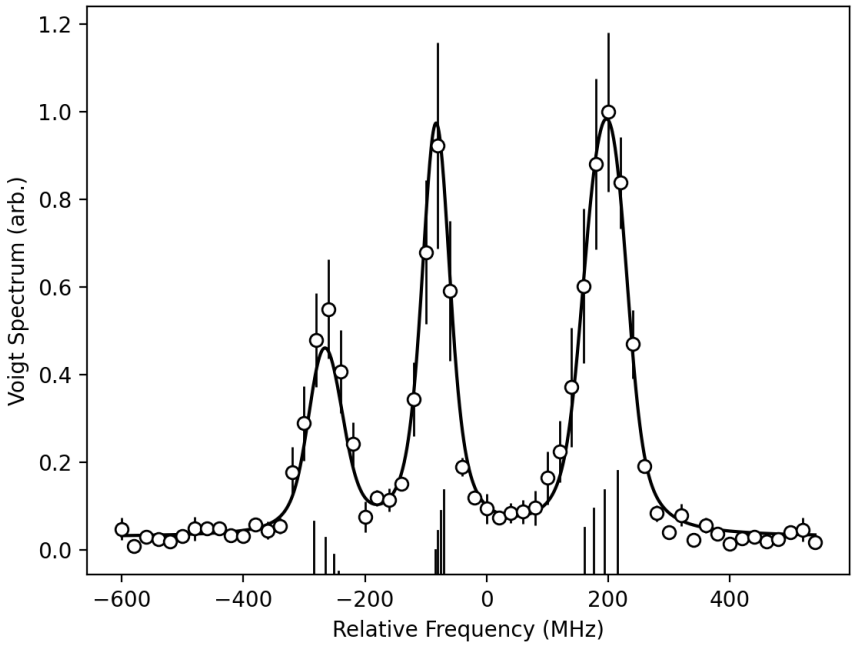

Figure 2.3: A least-squares fit of R(0) fluorescence data provided by the McCarron lab at the University of Connecticut. The circles are the data with error bars. The vertical lines at the bottom indicate where the $A^1\Pi$ hyperfine states lie and their relative intensities.

aluminum nuclear-spin Zeeman term is

$$\left\langle \eta, \Lambda, J, F_1, F, M \middle| -g_{Al}\mu_{Al} \sum_p T^1_p(\mathbf{I}_1) T^1_{-p}(\mathbf{B}) \middle| \eta, \Lambda', J', F_1', F', M' \right\rangle =$$

$$g_{Al}(3.64151)\mu_N B_z \delta_{JJ'} (-1)^{F+F'+2F_1+I_1+I_2+J-M} \times$$

$$\sqrt{I_1(I_1+1)(2I_1+1)(2F+1)(2F'+1)(2F_1+1)(2F_1'+1)} \times$$

$$\begin{Bmatrix} F_1' & F' & I_2 \\ F & F_1 & 1 \end{Bmatrix} \begin{Bmatrix} I_1 & F_1' & J \\ F_1 & I_1 & 1 \end{Bmatrix} \begin{pmatrix} F & 1 & F' \\ -M & q & M' \end{pmatrix} \tag{2.33}$$

The chlorine nuclear-spin Zeeman term, with g-factor g_{Cl}, is found similarly to be

$$\left\langle \eta, \Lambda, J, F_1, F, M \middle| -g_{Cl}\mu_{Cl} \sum_p T^1_p(\mathbf{I}_2) T^1_{-p}(\mathbf{B}) \middle| \eta, \Lambda', J', F_1', F', M' \right\rangle =$$

$$g_{Cl}(0.82187)\mu_N B_z \delta_{JJ'} \delta_{F_1 F_1'} (-1)^{2F+F_1+I_2+1-M} \times$$

$$\sqrt{I_2(I_2+1)(2I_2+1)(2F+1)(2F'+1)} \begin{Bmatrix} I_2 & F' & F_1 \\ F & I_2 & 1 \end{Bmatrix} \begin{pmatrix} F & 1 & F' \\ -M & q & M' \end{pmatrix} \tag{2.34}$$

It turns out that the magnetic moments of these two interactions are proportional to the nuclear magneton, which is defined relative to the Bohr magneton as

$$\mu_N = \mu_B \frac{m_e}{m_p} = \frac{m_e}{m_p}(1.39962449361\,\text{MHz Gs}^{-1}) = 7.6225932291 \times 10^{-4}\,\text{MHz Gs}^{-1} \tag{2.35}$$

with m_e being the electron rest mass and m_p being the proton rest mass. Since the Bohr magneton is used in the $A^1\Pi$ Zeeman term, this renders the Zeeman splitting of the $X^1\Sigma^+$ state be negligible.

The dominant Zeeman term for the $A^1\Pi$ state is the interaction between the electron's angular momentum and the magnetic field. The matrix elements of this term are

given as

$$\left\langle \eta, \Lambda, J, F_1, F, M \middle| g_L \mu_B \sum_p T^1_p(\mathbf{L}) T^1_{-p}(\mathbf{B}) \middle| \eta, \Lambda', J', F_1', F', M' \right\rangle =$$

$$g_L \mu_B B_z \Lambda (-1)^{F+F'+F_1+F_1'+I_1+I_2-\Lambda-M} \times$$

$$\sqrt{(2F+1)(2F'+1)(2F_1+1)(2F_1'+1)(2J+1)(2J'+1)} \times$$

$$\begin{pmatrix} F & 1 & F' \\ -M & q & M' \end{pmatrix} \begin{Bmatrix} F_1' & F' & I_2 \\ F & F_1 & 1 \end{Bmatrix} \begin{Bmatrix} J' & F_1' & I_1 \\ F_1 & J & 1 \end{Bmatrix} \begin{pmatrix} J & 1 & J' \\ -\Lambda & 0 & \Lambda \end{pmatrix} \tag{2.36}$$

where the space-fixed z-axis is defined by the magnetic field to be $p = 0$. When the Zeeman term interacts with different field strengths, the result is a shift in the energy levels. Typically this magnetic effect is discussed in three different regimes: weak-field, intermediate field, and strong-field. For the first tens of Gauss of magnetic field, the energy shift dependence on the magnetic field is linear and hyperfine levels can still be distinguished. Additionally the magnetic hyperfine quantum numbers m_F play an important roll here. In the strong-field regime, the hyperfine quantum numbers are no longer good quantum numbers as the Zeeman term overpowers the zero-field terms. At these field-strengths the magnetic field dependence is proportional to m_J rather than m_F. In the intermediate region, the behavior is not linear.

Clearly, the magnetic structure of the $A^1\Pi$ is very complicated due to all of the different hyperfine states. To be able to effectively trap AlCl in a magneto-optical-trap or to employ slowing methods such as Zeeman slowing will require special care.

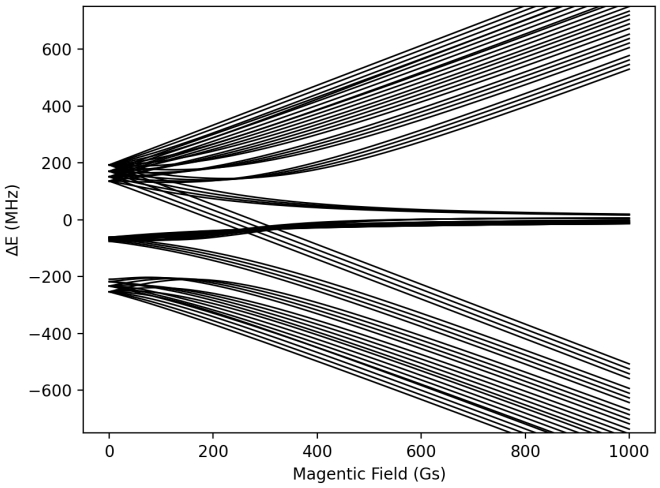

Figure 2.4: Simulated Zeeman splitting of the hyperfine structure for $A^1\Pi(\nu' = 0, J' = 1)$ state of AlCl.

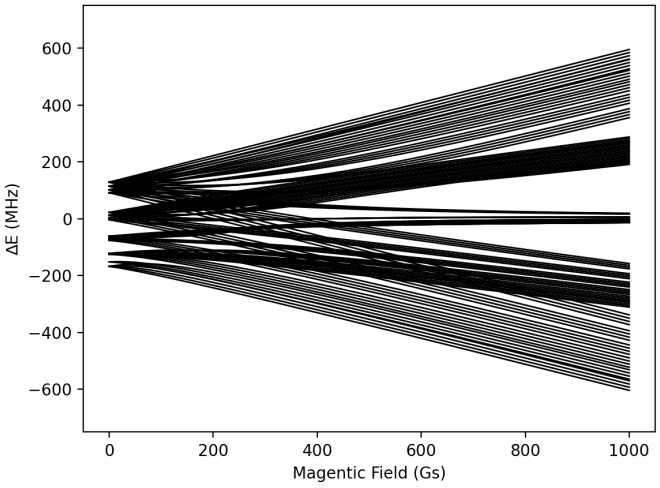

Figure 2.5: Simulated Zeeman splitting of the hyperfine structure for $A^1\Pi(\nu' = 0, J' = 2)$ state of AlCl.

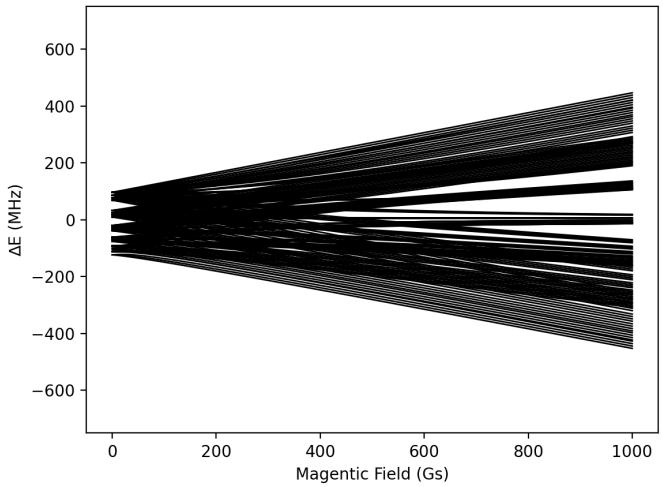

Figure 2.6: Simulated Zeeman splitting of the hyperfine structure for $A^1\Pi(\nu' = 0, J' = 3)$ state of AlCl.

2.10 $a^3\Pi$

The Hamiltonian of the triplet state that lies between the $X^1\Sigma^+$ and $A^1\Pi$ is more complicated that either of the two singlet states. The biggest reason for this is that the projection, $\mathbf{\Sigma}$, of the electron spin, $\mathbf{S}$, along the internuclear axis is 1. This means that the Hund's coupling case must be considered. Previous work has suggested that this coupling is likely to be case (a) Hund's coupling[45]. In case (a), the the total electron orbital angular momentum, $\mathbf{L}$, is precessing rapidly around the internuclear axis as before and the non-zero, total electron spin angular momentum, $\mathbf{S}$, is also precessing rapidly about the internuclear axis. The coupling between $\mathbf{\Lambda}$ and $\mathbf{\Sigma}$ is stronger than coupling to the molecular rotation, $\mathbf{R}$. This leads to the total electron angular momentum, $\mathbf{\Omega} = \mathbf{\Lambda} + \mathbf{\Sigma}$, which is aligned with the internuclear axis. This $\mathbf{\Omega}$ then couples to the rotation, yielding the total angular momentum, $\mathbf{J} = \mathbf{\Omega} + \mathbf{R}$ with values of $J = |R - \Omega|, ..., R + \Omega$. This means that the ground

state configuration of the $a^3\Pi$ state is split into four: $a^3\Pi_2$, $a^3\Pi_1$, and a parity doublet of $a^3\Pi_0^+$ and $a^3\Pi_0^-$.

The $a^3\Pi$ state zero-field hamiltonian contains additional terms as a result of the non-zero $\mathbf{\Sigma}$. The strongest of these is the spin-orbit coupling

$$H_{so} = AT^1_{q=0}(\mathbf{L})T^1_{q=0}(\mathbf{S}) \tag{2.37}$$

that couples the total electron orbital angular momentum to the total electron spin angular momentum. Additional smaller terms include spin-spin coupling

$$H_{ss} = \lambda\frac{2\sqrt{6}}{3}T^2_{q=0}(\mathbf{S},\mathbf{S}), \tag{2.38}$$

spin-rotation coupling

$$H_{sr} = \gamma T^1(\mathbf{N})\cdot T^1(\mathbf{S}) \tag{2.39}$$

and other even smaller higher-order terms. In addition there are two additional terms that appear in the Λ-doubling term such that this term is now

$$H_\Lambda = \sum_{q=\pm1} e^{-2iq\phi}\left\{pT^2_{2q}(\mathbf{N},\mathbf{S}) - oT^2_{2q}(\mathbf{S},\mathbf{S}) - qT^2_{2q}(\mathbf{N},\mathbf{N})\right\} \tag{2.40}$$

The hyperfine term of the Hamiltonian also gains additional terms, making this term

$$H_{HF} = \sum_\alpha \left\{ a_\alpha T^1_{q=0}(\mathbf{I}_\alpha)T^1_{q=0}(\mathbf{L}) + b_F^\alpha T^1(\mathbf{I}_\alpha)\cdot T^1(\mathbf{S}) + \frac{\sqrt{6}}{3}c_\alpha T^2_{q=0}(\mathbf{I}_\alpha,\mathbf{S}) + \sum_{q=\pm1} d_\alpha T^2_{2q}(\mathbf{I}_\alpha,\mathbf{S}) \right\} \tag{2.41}$$

with new hyperfine constants b_F, c, and d that must be determined in addition to the a constants that were used in the singlet states. The matrix elements of each term can readily be calculated using the same methods presented here for the singlet states. Each term will have an extra decoupling step resulting in an additional Wigner-6j symbol and additional contents in the square root and in the exponent of -1.

The Zeeman part of the $a^3\Pi$ state Hamiltonian gains additional terms corresponding to the electron spin, the most significant of which is

$$g_S \mu_B B_Z T^1_{p=0}(\mathbf{S}). \tag{2.42}$$

There are additional small terms, however the terms proportional to $T^1(\mathbf{L})$ and $T^1(\mathbf{S})$ usually dominate the observable features at the field strengths one typically uses in these experiments.

Chapter 3

UV Laser System

The $X^1\Sigma^+ \rightarrow A^1\Pi$ transition exists in the UV regime with $X^1\Sigma^+(\nu = 0) \rightarrow A^1\Pi(\nu'=0)$ around 261.5 nm and the first re-pump transition, $X^1\Sigma^+(\nu=1) \rightarrow A^1\Pi(\nu'=0)$, around 265 nm. The existing measurements and predictions for the frequency of these lines was not well enough known to simply purchase a narrow band laser system, thus we opted for a home-built third-harmonic generation (THG) laser system. The THG process is a result of sequential application of second-harmonic generation (SHG) and sum-frequency generation (SFG). The source laser frequency, ω_1, is first doubled in a SHG cavity to produce $\omega_2 = 2\omega_2$. Then ω_2 and some of the source frequency, ω_1 are combined with SFG to produce $\omega_3 = \omega_1 + \omega_2$. This produces laser light with frequency $\omega_3 = 3\omega_1$.

A tripled Titanium:Sapphire (Ti:Sapph) solid-state laser serves as an optimal first laser to address AlCl. There are many other ways to reach the 261 nm transition, for example the McCarron group at UConn has developed a system that quadrupoles a fiber laser to obtain 2 W of 261 nm laser light[36]. The advantage in beginning with a tripled

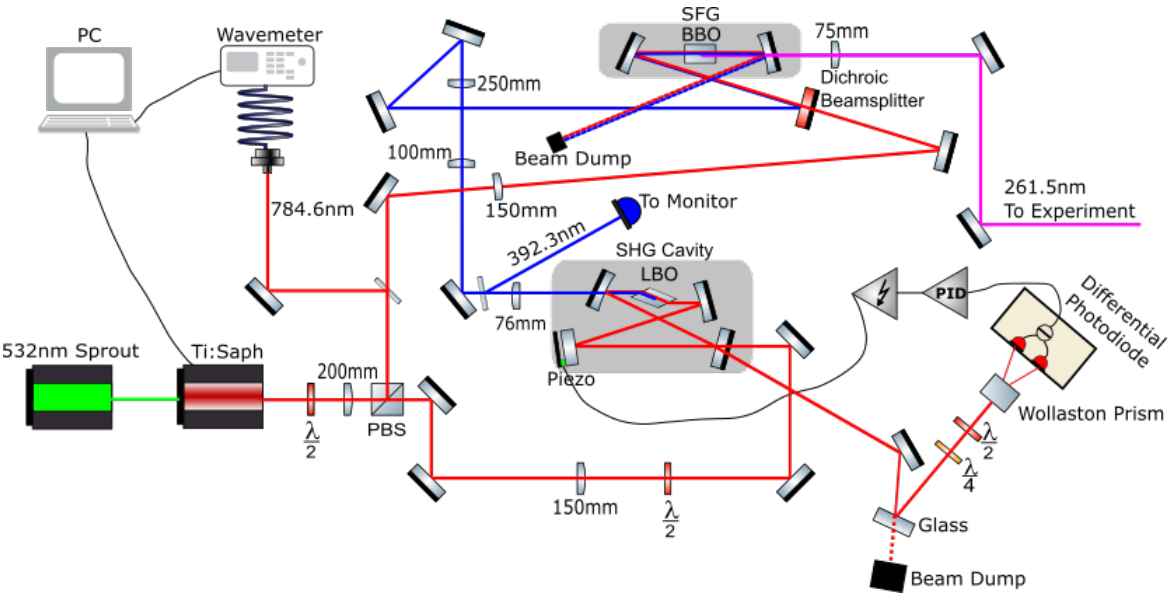

Figure 3.1: A schematic of the THG system that utilizes an LBO crystal in a bowtie cavity to frequency-double the 784.5 nm Ti:Sapph output (red) to 392.3 nm (blue). These two frequencies are summed in an LBO crystal to produce 261.5 nm UV light (magenta) for absorption spectroscopy of the $X^1\Sigma^+ \rightarrow A^1\Pi$ transition of AlCl.

Ti:Sapph lies in its large tuning range. This large tuning range allows the laser system to not only reach the 261 nm transition of AlCl, but can also be tuned to reach the repumping transitions, and, with a different crystal set, can be applied to address other molecules. Another advantage of using a tripled Ti:Sapph is that we can pick off the doubled output from the SHG cavity, and apply it to atoms such as ytterbium and molybdenum, and it can even reach the $a^3\Pi$ state of AlCl.

The Ti:Sapph lasers used for this work are Coherent-899 model solid state lasers. They are both pumped by Lighthouse Photonics Sprout-H lasers. The Sprouts produce a 532 nm beam with one Sprout outputting up to 10 W and the other outputting a max of 18 W. With the mirror set installed in the Ti:Sapph following the 18 W Sprout, going higher than 14 W did not increase the output power of the Ti:Sapph, and thus we kept the output

capped at 14 W. With a 14 W pumping power, we obtained a max Ti:Sapph output of 2 W.

3.1 Second-Harmonic Generation

The first step of the THG process is the SHG process. Our SHG setup utilizes a lithium triborate (LBO) crystal in a bowtie enhancement cavity to convert the incident near-infrared light to blue light. In the crystal two photons of laser light with frequency ω_1 are converted into a single photon of light with twice the frequency, ω_2.

The output power of the second-harmonic conversion of laser light with frequency ω_1 to frequency ω_2 with

$$\omega_2 = 2\omega_1 \tag{3.1}$$

can be calculated from properties of the non-linear crystal and input laser as

$$P_{\mathrm{SHG}} = \left(\frac{2\omega_1^2 d_{\mathrm{eff}}^2 L_c k_1}{\pi \epsilon_0 c^3 n_1^2 n_2} \cdot P_1^2 \right) \cdot h_{\mathrm{SHG}}(\sigma, \xi, B) \tag{3.2}$$

with crystal properties of the appropriate non-linear coefficient for SHG, d_{eff}, its length, L_c, and the indices of refraction in the crystal for the input laser, n_1, and the doubled output, n_2. The input laser's frequency, ω_1, wavenumber, k_1, and power, P_1 are included in the calculation. In application, this boils down to a mess of constants multiplying a function, $h_{\mathrm{SHG}}(\sigma, \eta, B)$, with σ relating to the confocal parameter of the crystal, b, and the phase mismatch, $\Delta k = 2k_1 - k_2$, as $\sigma = b\Delta k/2$. η relates the crystal length to the confocal parameter as $\eta = L_c/b$. B is the walk-off parameter and depends on the crystal length, input laser wavenumber, and the walk-off angle of the crystal, ρ, as $B = (\rho\sqrt{L_c k_1})/2$. The

full form of h_{SHG} is given as

$$h_{\mathrm{SHG}}(\sigma,\xi,B)=\frac{1}{4\xi}\int_{-\xi}^{+\xi}\mathrm{d}\tau_1\int_{-\xi}^{+\xi}\mathrm{d}\tau_2\frac{e^{i\sigma\cdot(\tau_1-\tau_2)}\cdot e^{-\frac{B^2(\tau_1-\tau_2)^2}{\xi}}}{(1+i\tau_1)\cdot(1-i\tau_2)} \tag{3.3}$$

The polarization of input laser in the cavity is rotated with a $\lambda/2$-waveplate (HWP) to be close to, but not perfectly, p-polarized. It is necessary to retain a small portion of the s-polarized light for locking the cavity as is explained later.

The SHG bowtie cavities consist of four mirrors and a non-linear crystal, in this case LBO. The mirrors are arranged to create a resonance cavity for the input laser light from the Ti:Sapph. Three of the mirrors are highly reflective to red light. The fourth mirror, the incoupling mirror, is only mostly reflective. After some experimentation, we used a mirror that is 98% reflective as an incoupler. Our mirror coatings are in integer reflectance and both 97% and 99% reflectivity only reduced the output power of the cavity.

The crystal is mounted on a rotation stage which is mounted on a translation stage. The combination of these two stages allows for fine control of the XYZ position of the crystal in the cavity and the orientation of the crystal lattice with the optical axis. The LBO crystal's end faces are Brewster-cut. This means that the face is cut such that the incoming p-polarized laser has no reflection off of the crystal face and all incident power is refracted through the crystal. It is important to optimize the crystal orientation such that the angle between the face and the incident laser is as close to Brewster's angle as possible as this minimizes a power loss channel. The rotation of the crystal about the optical axis must also be optimized. This is called the phase-matching angle as it rotated the ordinary and extraordinary axes of the non-linear crystal to optimize the SHG process. The output SHG power is very susceptible to changes in this angle. The output of the crystal creates a strong

astigmatism which is compensated for with a pair of mode-shaping cylindrical mirrors, one focusing horizontally and one focusing vertically. The optimal result is a properly collimated

The length of the cavity is stabilized using a Hansch-Couillaud (HC) lock. The reflection of the input laser light off of the back of the incoupling mirror is directed to a piece of glass to dump power. The almost-normal back-reflection off of this piece of glass then passes through a $\lambda/4$-waveplate (QWP) and a HWP. Then the resulting polarization mix is split by polarization at an angle of 10 degrees by a Wollaston prism. These two beams, one s- and one p-polarized are directed onto a differential photodiode circuit that takes the intensity difference between the two polarizations. This output error signal is captured by a Red Pitaya FPGA controller. The Red Pitaya contains a programmable PID controller that is applied to the error signal to create the control voltage feedback signal that is amplified and sent to the piezo. The piezo's length is proportional to the applied voltage, thus allowing for stabilization of the cavity length to resonance.

The output of the SHG part of the system can easily be diverted to be used for other absorption measurements. The tuning range of the LBO crystal is large enough that we were easily able to tune the Ti:Sapph to reach absorption lines for ytterbium, molybdenum, and aluminum. We even attempted to use the SHG output to scan for $X^1\Sigma^+ \rightarrow a^3\Pi$ absorption, however we were unable to find these lines. The frequencies of these $X^1\Sigma^+ \rightarrow a^3\Pi$ lines are not precisely known. This uncertainty, combined with the 100 MHz linewidth and forbidden nature of the transition led to the inability to find the line at present.

3.2 Sum-Frequency Generation

The SFG process utilizes a barium borate (BBO) crystal to convert two photons of laser light with different frequencies, ω_1 and ω_2, into a single photon of light with a frequency ω_3 such that

$$\omega_3 = \omega_1 + \omega_2 \tag{3.4}$$

Unlike the LBO crystal used for the SHG setup, the BBO crystal is not cut to Brewster's angle, as this angle would be different for each frequency of source light. For all the work presented here, the SFG setup is used in single-pass configuration with no resonant enhancement. This means that the produced UV light is on the order of tens of μW. While this may seem small, it is plenty to perform absorption spectroscopy on the strong lines in the $X^1\Sigma^+ \rightarrow A^1\Pi$ transition.

For single pass configuration, the two flat mirrors from a bowtie cavity are omitted. The curved mirrors on each side of the crystal are still necessary to maintain a good focus inside the crystal. Where the incoupling mirror used to be, a dichroic beamsplitter is installed. This component reflects blue light and lets red light pass. This allows for the overlap of the two incident frequencies as the red light passes through the back of the dichroic at the same spot that the blue is reflecting. Care is taken to ensure a good overlap as the output UV power in this configuration very strongly depends on the laser overlap volume inside the crystal.

For fluorescence measurements and for eventual slowing, much more laser power is required. The bowtie enhancement cavity must be closed and the cavity must be made resonant for both laser frequencies present inside. This requires some sort of dispersion

compensation. A solution currently being explored is to utilized a PID-controlled pair of actuators to rotate a pair Brewster plates inside of the cavity. When moved in conjunction, these plates can change the length of the cavity by different amounts for each frequency, thus allowing for the dual resonance to occur.

3.3 Wavemeter Calibration

It is a well-known fact that wavemeters are sensitive to changes in ambient temperature and pressure. Since the lab is neither a temperature-controlled nor pressure-controlled environment, it is important to determine the wavemeter offset before and after measuring a spectrum. For longer runs, intermediate calibration checks are necessary. To calibrate the wavemeter a universally-known value must be measured. In our lab we have two setups to perform such a calibration measurement for our Toptica WS-7 wavemeter.

3.3.1 Temperature-Stabilized HeNe

The quickest and easiest measurement to perform is to measure the output frequency of a temperature-controlled helium-neon (HeNe) laser. The output from the laser is directed into a fiber. The other end of the fiber is connected to the wavemeter. Once the HeNe has had ample time to warm up and stabilize to its temperature-controlled frequency, this frequency is measured. The wavemeter offset is determined by comparing the measured frequency to an expected value of 473.612512 THz. This value was determined using a rubidium pump-probe spectroscopy setup.

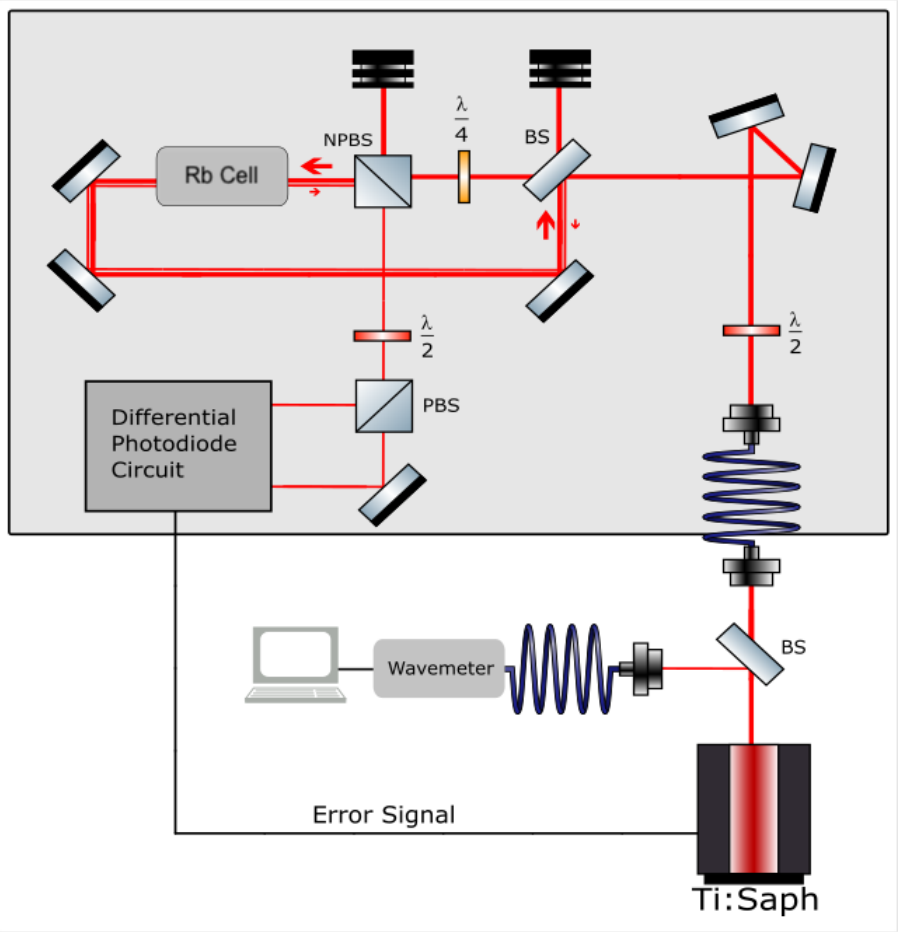

Figure 3.2: Pump-Probe absorption spectroscopy setup using a heated, rubidium vapor cell as an atomic reference.

3.3.2 Rb Pump-Probe Spectroscopy

An atomic reference is periodically used to check the frequency of the HeNe and to calibrate the wavemeter. To perform this calibration, we use a rubidium pump-probe saturated absorption spectroscopy setup. A strong "pump" beam and a weak "probe" beam are overlapped in a counter-propagating configuration through a heated Rb vapor cell. The Ti:Sapph is output is routed to the setup through a fiber. The Rb transition is thermally broadened such that hyperfine transitions are not normally resolved. This is where the

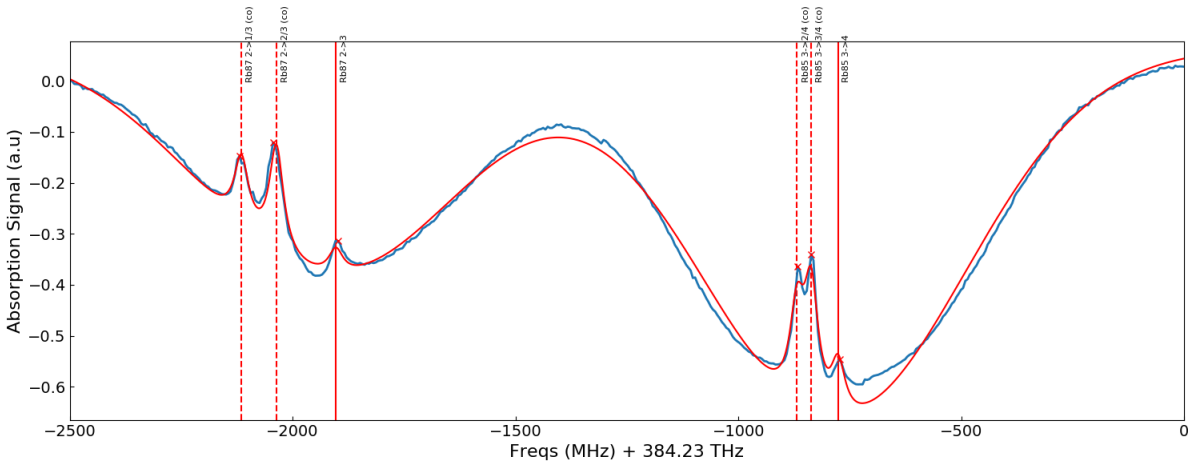

Figure 3.3: Rb Pump-Probe Absorption Spectroscopy Data

pump beam comes in. The pump beam drives the Rb such that some hyperfine states are occupied to the point of suppressing absorption to them. This leads to much narrower features that are burned into the absorption signal. The structure of these burned lines can be fit to high precision measurements and a wavemeter calibration offset can be determined.

Chapter 4

Cryogenic Buffer-Gas Beam Source

AlCl is a radical. This means that it is highly reactive with compounds it comes in contact with and wants to form other bonds. This means that it is not a substance that can be bought, but rather needs to be produced while running the experiment. Previous work on AlCl used a hot source for production[45] such as heating $AlCl_3$. For this work, gas-phase AlCl is produced via laser ablation of a solid precursor target into a cryogenic helium buffer-gas, i.e. a CBGB (cryogenic buffer-gas beam).

A common way to produce an atomic beam from metals is with an oven source. In these types of sources a solid chunk of that metal is heated via a method such as resistive heating to such that it starts evaporating. When the heating element is a stainless steel tube, with the sample inside, then the result is a hot atomic beam that is ready to be laser cooled and trapped. An oven source is simple and robust on the beam side, but requires more laser effort due to the initial high temperature of the source. On the other hand, a cryogenic buffer-gas beam source (CBGB)[25] generates a much colder beam source

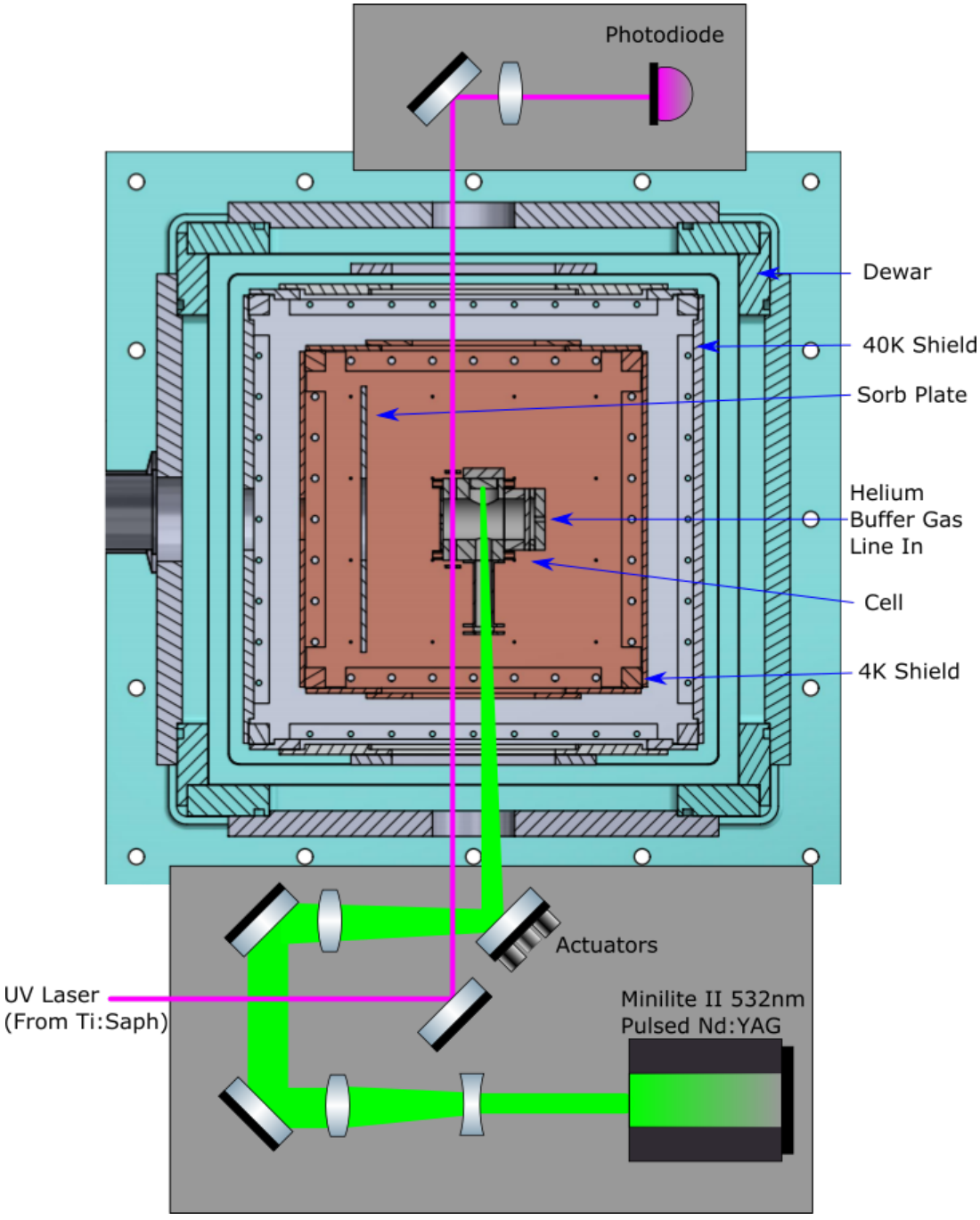

Figure 4.1: Dewar horizontal cross-section. Cell is depicted in single-stage configuration. Also depicted is the optical setup of the ablation laser.

by spending more effort on the beam production side, allowing for a larger percentage of the produced sample to be below the capture velocity of a magneto-optical trap. A CBGB utilizes collisional cooling between an otherwise hot source and a cryogenically-cooled buffer gas. The hot source can be an oven, a gas line, or, in our case, pulsed-laser ablation of a solid target.

4.1 Cryogenic System

Fortunately, in this century, cryogenic temperatures are much easier to achieve than in the era of Dewar and Onnes, competing to liquify helium. We have the luxury of a Cryomech closed-system helium pulse tube that produces 4 K temperatures at the push of a button (and some mild plumbing). In addition to the pulse tube, which produces the cryogenic temperatures, we have a set of shields to thermally isolate the central cell. This cell is the primary experimental environment for the work presented here. Note that for the following descriptions, "front" refers to the side from which the molecular beam is emitted.

4.1.1 Compressor

The pulse tube is a Cryomech PT-420 pulse tube. It has two temperature stages, one nominally at 40 K and one nominally at 4 K. I say "nominally" here as the actual base temperature is very dependent on the heat load of the system. When cooling with no heat load, the stages reached 25 K and 3.4 K (shown in Fig. 4.2), whereas with all shields installed, the base temperatures are around 40 - 50 K and 4.2 - 5 K.

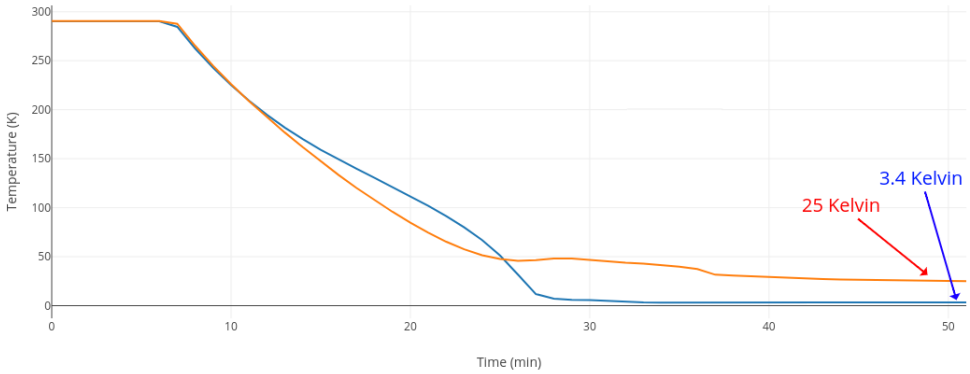

Figure 4.2: Cooldown of the 40K (orange) and 4K (blue) stages of the cryogenic system in an empty dewar with super-insulation thermally isolating each stage. This test was without any attached heat load, i.e. no thermal shields, cell, etc.

To accommodate the length of the pulse tube, a custom stainless steel nipple with aluminum adapting collar is used to mount the pulse tube to the top of the dewar. This design results in the 40K stage terminating inside the nipple, so a copper construction is used to extend the 40K foot of the pulse tube beyond the extent of the nipple into the chamber where it can be thermally connected to the shields.

4.1.2 Shields

There are three layers of thermal shielding to isolate the central cell from the thermal load of the lab environment. The outermost set of shields is a commercial dewar vacuum chamber (teal in Fig. 4.1). These external shields remain around the ambient temperature in the lab and are sealed with o-rings to enable a minimum pressure of $\approx 10^{-7}$ Torr. This vacuum is created by pumping with a TwisTorr Turbopump, backed by a Agilent IDP-15 Dry Scroll Pump. The shields inside are adapted from a CalTech design.

The 40K shields are suspended from the top plate of the dewar with #10-32 steel all-threads. The use of steel here is to exploit its relatively low thermal conductivity to reduce the system's heat load. The 40K shields are made from aluminum (Al 6061). There is a 2-inch circular hole in the front for the molecular beam to pass. The side panels constructed of multiple pieces. There is an outer frame that is used to maintain the rigidity of the box assembly and serve to make the removable panel easier to access. The removable panel on the spectroscopy side must be removed each time the target is replaced, so easy access is a necessity. Mounted on each of these removable panels is a window mount. There is one 50×50 mm window on the spectroscopy side. The ablation side has two 50×50 mm windows side by side to effectively make a single 100×50 view area. This extra area is to allow optical access for both the ablation laser and several locations both in and in front of the cell for absorption spectroscopy.

Suspended from the top plate of the 40K aluminum shields are a set of copper shields, dubbed the 4K shields. These shields, and all copper that is cooled to around 4K, are constructed of oxygen-free copper (Cu-101 OFE) to maximize thermal conductivity.

To further reduce the heat load on the shields, a material referred to as "super-insulation" is used. This super-insulation is composed of a multi-layer foil-like material that serves to insulate the inner components from radiative heat transfer from warmer stages. Both the 40K and 4K shields have their sides and bottom wrapped in this material.

Good thermal connection is required to keep the shields cryogenic. We cannot directly mount the shields to the pulse tube as the pulse tube is relatively delicate and it doesn't take much torque to damage it. Thus, the shields are all suspended from the

top and heat links are used to connect the top plate of each shield to the pulse tube temperature stage. Each heat link is composed of two L-shaped copper pieces and a short segment of copper braid. The copper braid gives an excellent structural flexibility and thermal conductivity. Each shield is attached to its corresponding pulse tube stage with four of these heat links. In the case of the 40K shields, these heat links attach to the aforementioned copper construction.

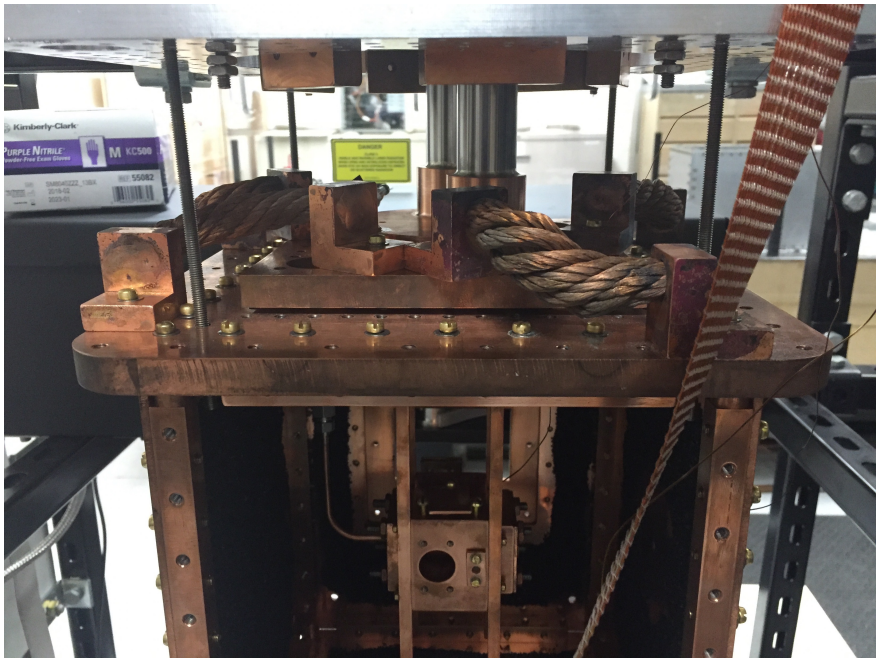

Figure 4.3: Heat Links connecting 4K pulse tube foot to the top plate of the 4K shields.

4.1.3 Cell

At the heart of the assembly of shields is the central cell. It is here that the solid precursor target is loaded for laser ablation into a cryogenic buffer-gas. A good choices for a buffer-gas is The yield from a field-standard single stage cell is typically ≈150 m/s. With

an added second stage, the buffer gas cell should yield a beam with velocity of ≈60 m/s. I say "should" here as the debugging process is ongoing as to why the second stage doesn't seem to be doing anything and the 2-stage cell is producing the expected output of a single stage.

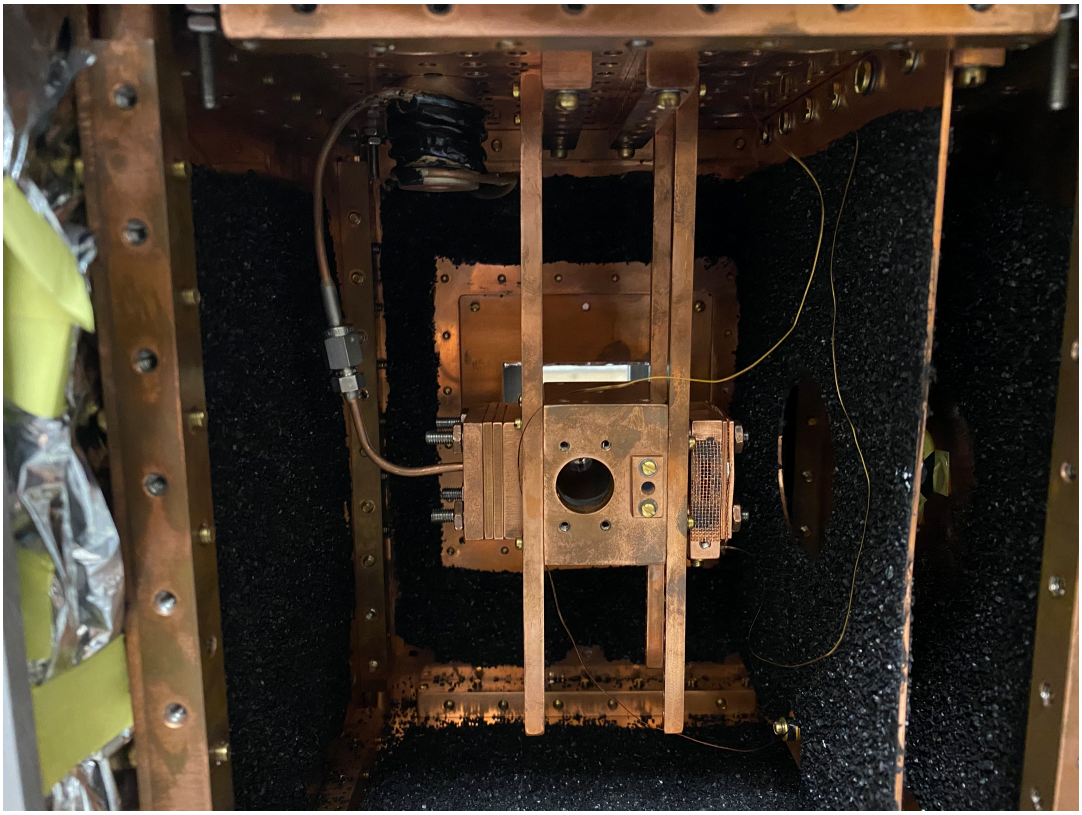

Figure 4.4: 2-Stage Cell

The cell design is largely based on the one used at Harvard. The basic characteristics are a 1" diameter circular bore to serve as the bulk of the interior volume. The hole pattern through all components through which the all-threads are used with nuts and spring washers is a 1" x 1" square for #10-32 screw clearance. All copper used is copper

101-OFE. For all the work presented here, Apiezon vacuum grease is used between all surfaces to form good thermal contact. The assembled 2-stage cell is shown in Fig. 4.4, and the disassembled 2-stage cell components are shown in Fig. 4.5. Listed from left to right in Fig. 4.5, these components are as follows:

- **Cell Back:** Helium line into the cell. 1/8" copper tube is brazed to a 1/4" x 1.5" x 1.5" piece of copper with a 1/8" center hole to allow the helium to enter the cell. The other end of the copper tube is a Swagelock VCR connection to attach to the rest of the helium line.

- **Small Spacer:** A spacer to separate the diffuser from the helium line input. Consists of a 1" diameter circle cut into the center of a 1/8" x 1.5" x 1.5" piece of copper.

- **Diffuser:** The diffuser serves to diffuse the incoming helium flow. Without this component, you would have a jet of helium traveling through the center of the cell. The part consists of four slots cut into a 1/8" x 1.5" x 1.5" piece of copper. Each slot spans a little less than 90 degrees, with an outer diameter of 1". This disrupts the jet-like flow and converts it to a more diffuse flow through the cell. This component has been modified from previous designs to have each slot rounded at the ends instead of with sharp corners. This design change was made to allow for easier machining of the component.

- **Large Spacer:** This spacer serves to augment the volume of the main body of the cell. This spacer consists of a 1" circle cut through a 1/2" x 1.5" x 1.5" copper piece.

- **Main Body:** The main body of the cell is a block of copper with a 1" bore cut through center. Perpendicular to the main bore are two additional bores: a large one upstream (relative to the helium flow) for ablation access and target insertion, and a small one downstream for in-cell spectroscopic probing.

- **1st-Stage Aperture:** The first stage aperture is the exit from which the sample (and helium) is extracted from the main cell. The aperture is 6 mm in diameter. The component is constructed from a 1/16" x 1.5" x 1.5" piece of copper. On the inside of the aperture, a 45 degree chamfer is applied to mitigate interference of collisions off of the aperture walls on the sample beam. Sample extracted from this stage should have a forward velocity of ≈150 m/s.

- **Washers:** These washers are simply 1/2" wide, 1/8" thick copper cylinders with a clearance hole for a #10-32 screw in the center.

- **2nd-Stage Body:** The second stage body has the same 1" center bore. The body is constructed from a piece of copper. There are two vents on the sides. Each vent has a piece of copper mesh covering it, attached with the two-component Stycast 2850 epoxy. Additionally, there are a few mounting holes around the bottom of the component to mount a temperature sensor.

- **2nd-Stage Aperture:** The second stage aperture is the exit from which the sample (and helium) is extracted from the second stage. The aperture is 7 mm in diameter. The component is constructed from a 1/16" x 1.5" x 1.5" piece of copper.

- **Mesh:** The mesh covers the second stage aperture. Indium is pressed into the mesh to form a good thermal contact with the copper pieces holding the mesh in place.
- **Mesh Holder:** The mesh holder has an aperture diameter of 9 mm. The component is constructed from 1/16" x 1.5" x 1.5" piece of copper. The sole purpose of this component is to hold the mesh on by creating a sandwich between this component and the second stage aperture.
- **Snorkel:** The snorkel is the name given to the tube that serves to displace the window through which the ablation laser enters the cell. The reason for this is to ensure the ablation laser passes through the window when less focused and thus reduce the risk of passing the damage threshold for the window.
- **Spectroscopy Windows:** The 5mm spectroscopy windows are held in place on the sides of the main cell body by 1/16" copper pieces that clamps them in place.
- **Target Holder:** The target holder consists of two pieces and serves to mount the precursor target in the cell. The target is affixed with Stycast to the removable, round part of the target holder.

This cell design is far from perfect. It suited our needs well for the work presented here, however work is still being done to make it ready for use for laser cooling. The ongoing problem is the lack of an observable second stage output. Only the 150 m/s output is observed from the first stage. I will leave the work done to fix this dilemma to the dissertation of the student who is performing the troubleshooting. The current best theory is that the sorbs are decayed to the point of requiring replacement which is driving the

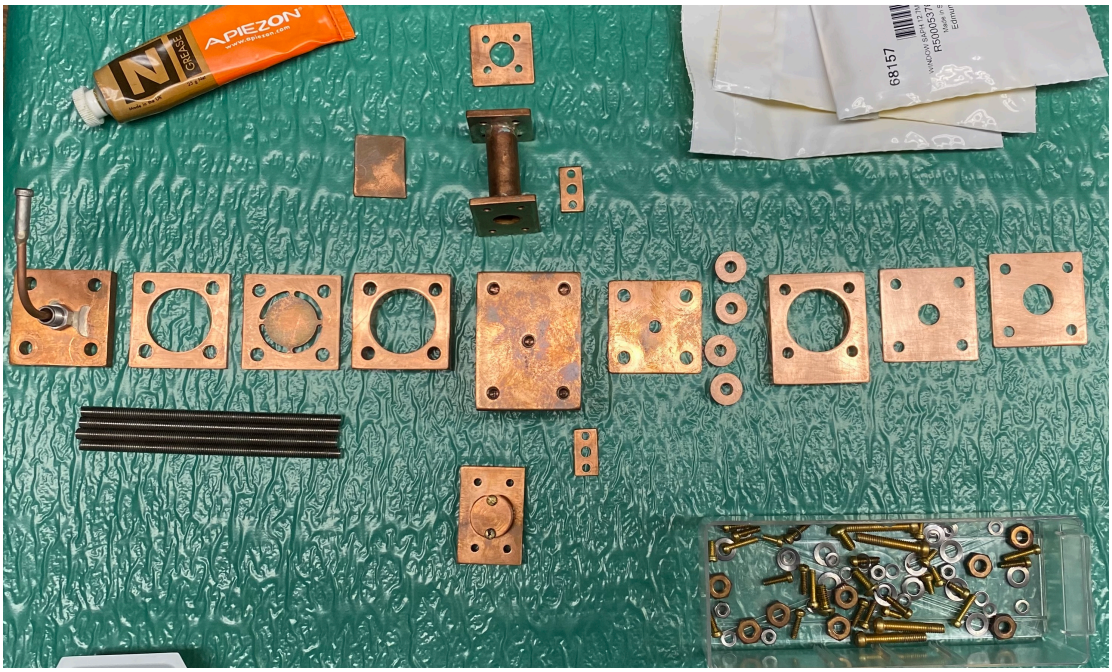

Figure 4.5: Disassembled 2-Stage Cell showing (from left to right) the cell back with helium line entry, 1/8" spacer, diffuser, 1/2" spacer, main cell body with snorkel and glass clamps above and target holder and glass clamp below, first stage aperture, round spacers, second stage body, second stage aperture, and finally the mesh holder.

pressure in the dewar high enough to destroy the beam, however I will leave the details of the trouble-shooting to future students as they were the ones to perform the tests.

4.1.4 Temperature Monitoring

There are eight temperature sensors installed on the cryogenic system to confirm the temperatures and provide an early-warning system for impending sorb release. These sensors use a configuration of temperature-dependent-diodes similar to a Wheatstone bridge to accurately measure the cryogenic temperature at which we work. The temperature sensors are read out and recorded on the lab server.

4.2 Helium Buffer Gas

We utilize purified ^{4}He as our cryogenic buffer gas. The helium flow is regulated with a Unit flow controller which can control the helium flow from 0-10 sccm as measured in Fig. 4.6. The helium line passes into the chamber through a feedthrough at the top

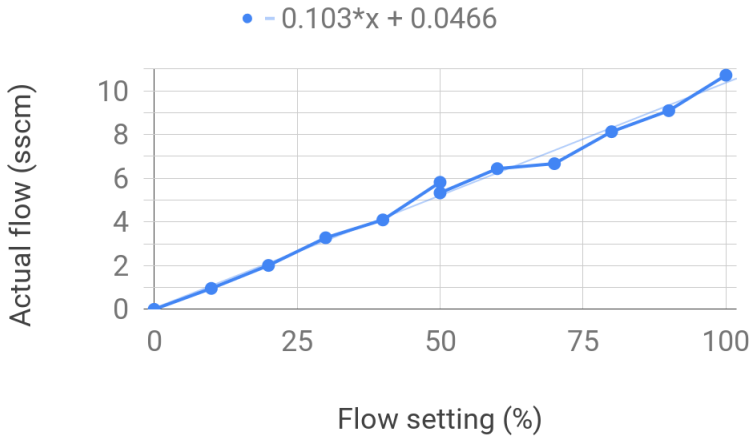

Figure 4.6: Unit controller helium flow characterization

of the dewar. Once inside the dewar, we utilize 1/8" tubing, connected with Swage-Lock VCR (gasket) connections. Copper (Cu 101-OFE) bobbins are used to thermally anchor the helium line to the pulse tube temperature stages by coiling 1/8" copper tubing around a groove in a copper cylinder and utilizing a braze joint for good thermal contact. The bobbins are attached to the top plate of the aluminum (40K) shield and two to the top plate of copper (4K) shield as shown in Fig. 4.7.

1/8" stainless steel tubing is used for thermal insulation between temperature stages. The two 4K bobbins are mounted on the top and bottom of the 4K top plate (see

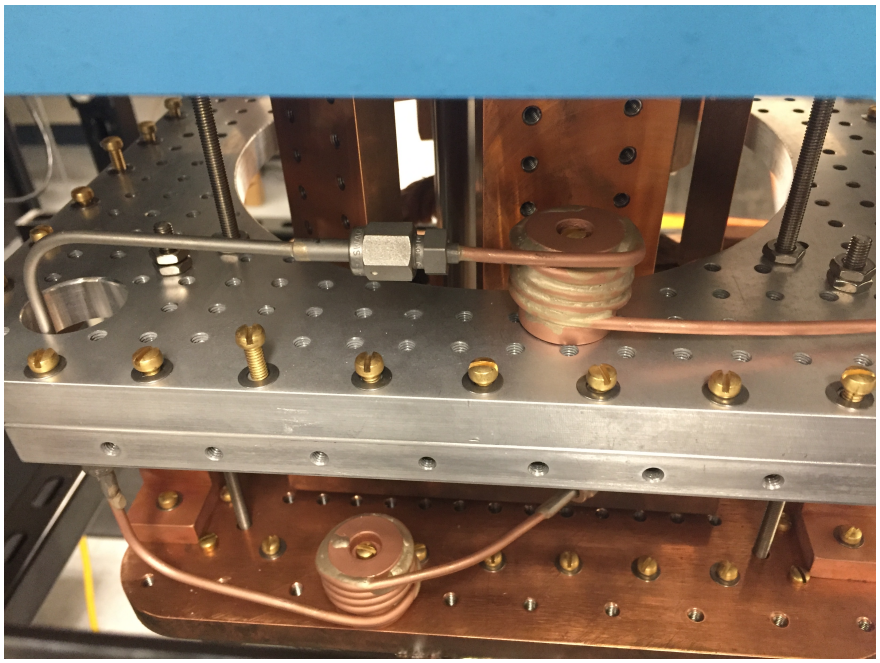

Figure 4.7: 40K and first of two 4K copper thermal bobbins, connected by a stainless steel piece for thermal insulation. Helium flows in from the top right copper tubing and continues down into the cell.

Fig. 4.7 and Fig. 4.4). After the last bobbin, the helium line continues into the back of the cell as can be seen in Fig. 4.4.

The number density of helium atoms inside the cell, n, depends on the helium flow into the cell, f, the area of the cell aperture, A, and the mean thermal velocity of the helium, $\bar{v} = \sqrt{8k_BT/\pi m}$[25] as

$$n = \frac{4f}{A\bar{v}} \tag{4.1}$$

which implies that our first stage should have a 4K helium number density per sccm of flow of

$$\frac{n}{f} = \frac{4 \times (4.5 \times 10^{17} \text{atoms}\,\text{s}^{-1}\,\text{sccm}^{-1})}{(0.282\text{cm}^2) \times (145\text{m}\,\text{s}^{-1}) \times (100\text{cm}\,\text{m}^{-1})} = 4.38 \times 10^{14}\text{cm}^{-3}\,\text{sccm}^{-1} \tag{4.2}$$

This means that the in-cell helium pressure per sccm of flow can be estimated using the

ideal gas law as

$$\frac{P}{f} = \frac{n}{f} k_B T = 0.181\,\mathrm{mTorr\,sccm^{-1}} \tag{4.3}$$

for a 4K gas flow.

4.2.1 Yb Demonstration of Buffer-Gas Cooling

Immediately after ablation, the produced puff of hot gas undergoes collision interactions with the cryogenic buffer-gas and begins to cool down. This effect can be measured by fitting the decreasing line-width of the spectrum as time evolves. A simple test of the functionality of the buffer-gas was performed to verify that the bobbins were providing sufficient cooling power to produce an appropriately cryogenic helium flow. For this test, we ablated a solid Yb target and performed in-cell absorption spectroscopy. The amount of absorption for a particular frequency set-point drops with time as Yb exits the cell aperture, and, more pertinent to this test, the width of the doppler broadening changes. From the doppler broadening, as shown in detail later, the temperature is extracted.

This doppler fit was not able to fit the first millisecond or so of data due to the non-gaussian shape of the lines from ablation-laser after-glow and Yb absorption saturation. This saturation could have been eliminated by reducing the power, however the later signals were of more interest, and reducing ablation power would reduce the produced Yb and thus the signal-to-noise threshold would be reached sooner. As is, this measurement shows the thermalization of the Yb sample with the He buffer gas down to a temperature of around 6 K. As this was warmer than desired, we responded by adding the second 4K bobbing to the inside-top of the 4K shield as detailed above.

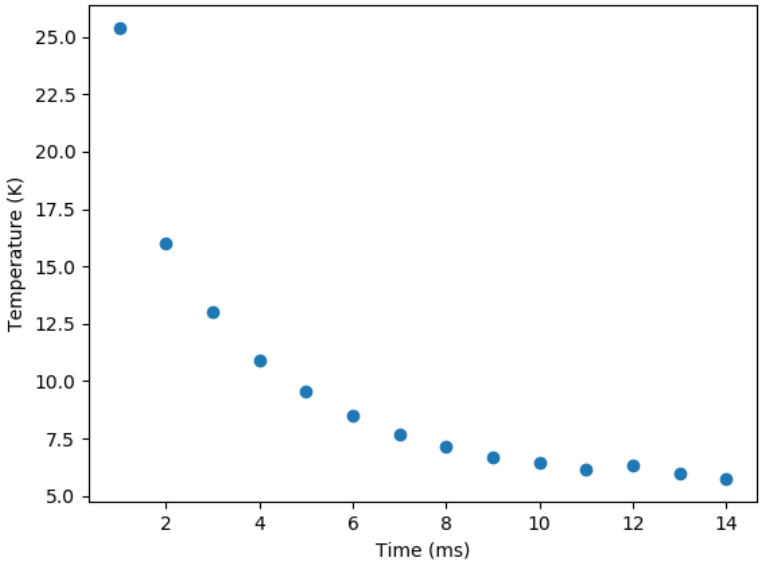

Figure 4.8: Example Yb cooling by buffer gas collisions deduced from doppler broadening of in-cell absorption lines for times after ablation. Ablation occurs at $t = 0$ ms.

4.2.2 Sorbs

While running the experiment, we are constantly flowing 3-4 sccm of helium into the system. When flowing in helium, the turbopump alone does not provide sufficient pumping power to maintain a pressure of 10^{-6} Torr. To remedy this, we utilize sorb plates. These sorb plates consist of a 4K copper surface on which coconut charcoal has been affixed using Stycast 2850 two-component epoxy. The Stycast is mixed with Catalyst 24LV at a ratio of 100:7.5 by mass. There is no known explanation as to why coconut charcoal is preferable over other kinds of charcoal, however it is known in the CBGB community that this is the case.

The sorb plates are prepared by spreading and even, thin layer of the stycast/catalyst mix over the copper piece of the dewar that is getting a sorb. A straight edge is used to

ensure an even spread. If the spread is too thick, it will be difficult to cool the charcoal. If the spread is too thin, the charcoal will not adhere well to the surface. Once the stycast is spread, coconut charcoal is sprinkled over the plate, fully covering all the stycast that has just been spread. After 12 hours of curing, it is safe to shake off any loose charcoal. The panel is now ready to be installed in the dewar.

4.3 Laser Ablation

To produce gas-phase AlCl, we utilize pulsed-laser ablation of a solid precursor target. To achieve this, we us a Continuum MInilite II 532 nm pulsed Nd:Yag laser. The pulse width is 5±2 ns and with a maximum of 25 mJ per pulse. It should be noted that while the specified max energy is 25 mJ per pulse, attempts to confirm this consistently yield upward of 32 mJ per pulse.

4.3.1 Laser Setup

The Minilite is installed on a breadboard that is mounted to the uni-strut framing surrounding the Dewar. The breadboard has an attached aluminum box to reduce the risk of a stray reflection. The optical configuration is shown in Fig. 4.1. The output beam of the Minilite is first expanded and collimated using a paired diverging and converging lens. (This is chosen over the standard telescope configuration as an in-air focus of the Minilite can ionize the air). Two planar mirrors direct the expanded beam through a focusing lens. After this lens, an actuator-controlled mirror steers the converging beam into the cell with the focus at the target location.

Chapter 5

Absorption Spectroscopy

To be able to apply our UV laser system to AlCl, we need to know where the absorption lines for the $X^1\Sigma^+ \rightarrow A^1\Pi$ transition. Previous measurements of these lines[45] were performed at high temperatures such that thermal populations limited observations of lines to $\nu \geq 3$ and $J \geq 10$. The first order of business when starting to work with AlCl was to measure the low-ν and low-J transitions as these are the states with the largest occupation numbers at the few-K temperatures at which this work is performed. Ram extrapolates the band origin of the $X^1\Sigma^+(\nu=0) \rightarrow A^1\Pi(\nu'=0)$ to be at 38237.00(5) cm^{-1} (1146.316(1) THz). This provided a sufficient estimate to purchase the appropriate crystals, however it did take some searching to find the first line of the $X^1\Sigma^+(\nu=0) \rightarrow A^1\Pi(\nu'=0)$ manifold. The first observed AlCl absorption signature turned out to be a line in the R branch ($\Delta J = +1$). After finding the first line, the rest of the manifold followed quickly and it wasn't long before we found the Q branch ($\Delta J = 0$) and the P branch ($\Delta J = -1$). These lines, along with a handful of lines from the $X^1\Sigma^+(\nu=1) \rightarrow A^1\Pi(\nu'=1)$ manifold allowed

for fitting of the low-order Dunham coefficients for the $A^1\Pi$ state. Using these molecular constants, an estimate of the Franck-Condon factors is determined for the cooling transition to be 99.88%, confirming theory predictions that the vibrational transitions are amenable to laser cooling.

5.1 Measurement Procedure

The in-cell absorption spectroscopy was performed using the previously described THG Ti:Saph with laser alignment depicted in Fig. 4.1 through the spectroscopy windows of the cell. The experiment is controlled via a script programmed in python for operation with the Artiq framework.

5.2 Line Broadening Mechanisms

Each absorption line has broadening mechanisms that contribute to the frequency width of its absorption. They contribute a Lorentzian characteristic, a Gaussian characteristic, or a convolution of both, a Voigt characteristic.

5.2.1 Lorentzian Broadening

There are two observed mechanisms that contribute to a Lorentzian-type broadening of a spectral line: collisional pressure-broadening and natural broadening. Once the sample leaves the cell, the pressure is low enough that the pressure-broadening is neglected and the entirety of the Lorentzian broadening is taken to be due to natural broadening.

The form of Lorentzian broadening is

$$\phi_L(x;\gamma) \equiv \frac{\gamma}{\pi(x^2+\gamma^2)} \tag{5.1}$$

where $x = f - f_0$ and $\gamma = \Gamma/4\pi$ where Γ is related to the lifetime, τ, by $\tau = 1/(2\pi\Gamma)$.

5.2.2 Gaussian Broadening

$$\phi_G(x;\sigma) \equiv \frac{e^{-x^2/(2\sigma^2)}}{\sigma\sqrt{2\pi}} \tag{5.2}$$

The most prevalent source of Gaussian broadening in our system is Doppler broadening. In this case,

$$\sigma(T; f_0, m) = \sqrt{\frac{k_B T}{mc^2}} f_0 \tag{5.3}$$

where T is the temperature in K, m is the mass of AlCl, and f_0 is the center line frequency of the line.

5.2.3 Voigt Broadening

In our temperature and pressure regime, all spectral lines will contain both Gaussian and Lorentzian broadening effects. When these two effects are convolved together, the result is a Voigt profile, defined as

$$\phi_V(x;\sigma,\gamma) \equiv \int_{-\infty}^{\infty} \phi_G(x';\sigma)\phi_L(x-x';\gamma)dx' \tag{5.4}$$

where σ is the gaussian broadening width amd γ is the Lorentzian broadening width. This integral can be evaluated using the Faddeeva function into the (computationally) simpler form of

$$\phi_V(x;\sigma,\gamma) = \frac{\mathrm{Re}[\mathrm{erfcx}(\frac{\gamma - ix}{\sigma\sqrt{2}})]}{\sigma\sqrt{2\pi}} \tag{5.5}$$

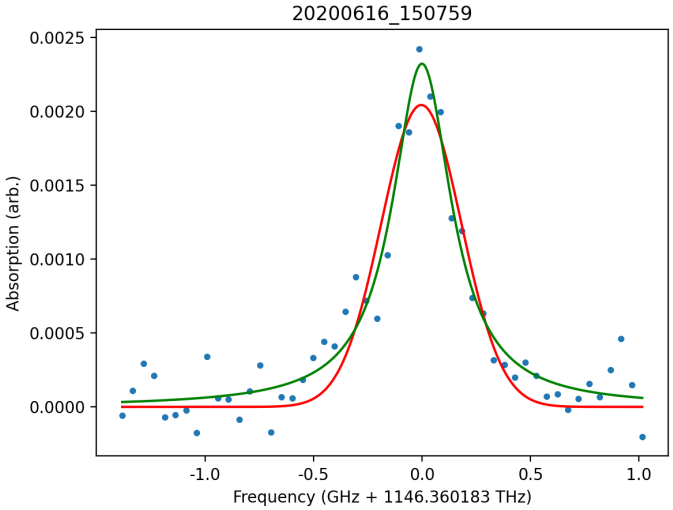

Figure 5.1: Comparison between utilization of a Doppler fit (red) and a Voigt fit (green) when fitting absorption data (blue) for line centers.

where erfcx is the scaled complimentary error function. When we fit our absorption lines, we initially assumed a Doppler-dominated regime, and only included Gaussian broadening mechanisms, however we found that many of the lines were better fit by a Voigt profile, implying that there are significant Lorentzian broadening effects from Pressure-broadening (the natural line width is much less than the Doppler-broadening at our temperature scale. In principle, one would expect that if you have symmetric absorption data that both a Gaussian fit and a Voigt fit would produce the same line center. In our case, there was enough noise fluctuation relative to our frequency set-point density to cause the data to not be symmetric enough for the fits to produce the same line center, and we adopted the Voigt profile for fitting the data.

5.3 Line Intensities

5.3.1 Franck-Condon Factors

Franck-Condon factors indicate the transition probability between vibrational states. For an optical-cycling scheme in which cycling is performed on the $X^1\Sigma^+(\nu{=}0) \leftrightarrow A^1\Pi(\nu'{=}0)$ transition, the Franck-Condon factor must be as close to 1.0 as possible to minimize leakage into the $X^1\Sigma^+(\nu = 1)$ ground vibrational state. Any molecules in this state are no longer accessible to the main cooling laser, and must be treated with an auxiliary re-pump laser set to the frequency of the $X^1\Sigma^+(\nu{=}1) \rightarrow A^1\Pi(\nu'{=}0)$ transition.

The magnitude of the Franck-Condon factors can be estimated through numerical simulation[CITE] and utilizing molecular constants extracted from a fit to a measured spectrum. The Franck-Condon factors for small ν are estimated using the overlap of simple harmonic oscillator approximation wave functions.

$$\mathrm{FCF} = |\langle\psi_{v'}|\psi_v\rangle|^2 \tag{5.6}$$

5.3.2 Hönl-London Factors

Hönl-London factors give the transition probability between rotation states and arise directly from the dipole transition hamiltonian

$$H = -T^1(\boldsymbol{\mu}_e) \cdot T^1(\mathbf{E}) = -\sum_p (-1)^p T^1_p(\boldsymbol{\mu}_e) T^1_{-p}(\mathbf{E}) \tag{5.7}$$

where $\boldsymbol{\mu}_e$ is the electric dipole moment and $\mathbf{E}$ is the applied electric field. When we define the space-fixed $p = 0$ coordinate to be aligned with the electric field, the dependency on Λ

and J is proportional to

$$\left\langle \Lambda, J \middle|\middle| T^1_{p=0}(\boldsymbol{\mu}_e) \middle|\middle| \Lambda', J' \right\rangle^2 =$$

$$\left\langle \Lambda, J \middle|\middle| \sum_q \mathcal{D}^{(1)}_{.q}(\omega)^* T^1_q(\boldsymbol{\mu}_e) \middle|\middle| \Lambda', J' \right\rangle =$$

$$(2J+1)(2J'+1) \begin{pmatrix} J & 1 & J' \\ -\Lambda & q & \Lambda' \end{pmatrix}^2 T^1_q(\boldsymbol{\mu}_e) \tag{5.8}$$

from which the Hönl-London factors can be read off as

$$\text{HLF} = (2J+1)(2J'+1) \begin{pmatrix} J & 1 & J' \\ -\Lambda & q & \Lambda' \end{pmatrix}^2 \tag{5.9}$$

5.3.3 Hyperfine Transistion Probability

To determine the transition probabilities for the full hyperfine hamiltonian, the primitive basis sets are used to evaluate the matrix elements of the transition dipole with

$$d^q_{ij} E_q = \left\langle \eta, \Lambda, J, F_1, F, M \middle| -T^1_q(\boldsymbol{\mu}_e) T^1_{-q}(\mathbf{E}) \middle| \eta, \Lambda', J', F_1', F', M' \right\rangle \tag{5.10}$$

Utilizing the Wigner-Eckart theorem as before, the matrix elements can be derived as

$$d^q_{ij} = (-1)^{F+F'+F_1+F_1'+I_1+I_2+1-\Lambda-M} \times$$

$$\sqrt{(2F+1)(2F'+1)(2F_1+1)(2F_1'+1)(2J+1)(2J'+1)} \times$$

$$\begin{pmatrix} F & 1 & F' \\ -M & q & M' \end{pmatrix} \begin{Bmatrix} F_1' & F' & I_2 \\ F & F_1 & 1 \end{Bmatrix} \begin{Bmatrix} FJ' & F_1' & I_1 \\ F_1 & J & 1 \end{Bmatrix} \times$$

$$\left[\begin{pmatrix} J & 1 & J' \\ -\Lambda & -1 & \Lambda \end{pmatrix} + \begin{pmatrix} J & 1 & J' \\ -\Lambda & 1 & \Lambda \end{pmatrix} \right] \tag{5.11}$$

The utilization of d_{ij}^q here allows for calculation of the branching ratios as

$$\Gamma_{ij} = \Gamma \frac{\left| d_{ij}^q \right|^2}{\sum_i \left| d_{ij}^q \right|^2} \tag{5.12}$$

where Γ_{ij} is the decay to a particular state with Γ as the total transition linewidth.

5.4 Data Analysis

5.4.1 Signal Quality Improvement

After initial observations of absorption, two major signal quality improvements were made before recording publishable spectroscopy data.

Blue Noise

A significant amount of the signal noise was determined to arise from laser intensity fluctuations from the locking of the SHG cavity. To mitigate this noise source, a pick-off from the SHG output is directed into a photodiode to measure the time dependent intensity fluctuations. These fluctuations are then scaled and subtracted from absorption signal, resulting in a reduction in signal noise.

Ablation Flash

Early time traces on the absorption photodiode showed a strong, short spike immediately after the ablation laser fires, followed by the expected voltage dip corresponding to absorption. This spike is attributed to a green (532 nm) afterglow from the ablation laser. To remove this unwanted feature from the absorption signal, we utilize two different

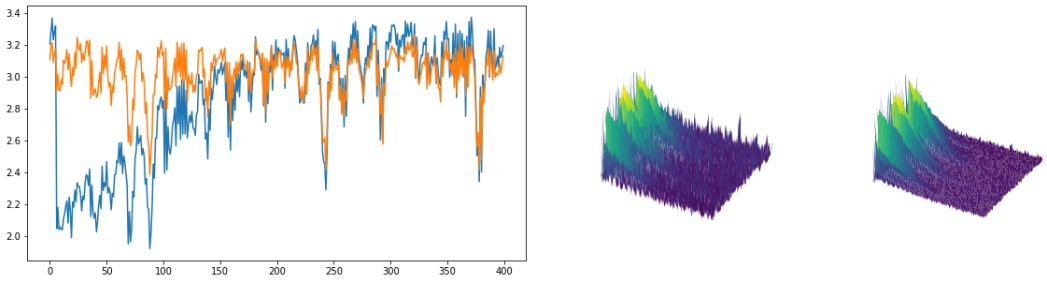

Figure 5.2: Comparison between Yb absorption signals. The left plot is an overlay of a typical absorption signal (blue) with the power fluctuations of the SHG cavity. The surface plots are a 3D representation of a sample Yb spectroscopy without (left) and with (right) blue-noise subtraction to illustrate the smoothing benefit of this blue-noise subtraction.

filters, depending on application. When using the 261 nm UV laser as for AlCl absorption measurements, a 261 nm notch filter was used, effectively blocking all frequencies except those within a few nm of 261 nm. When measuring K (red, 767 nm) and Al (blue, 395 nm) absorption, a green filter was used to block just the ablation flash. Both of these filters were effective at removing the ablation flash and leaving the absorption signal intact.

5.4.2 Line Centers

The end goal of this absorption spectroscopy is to measure the molecular constants (Dunham coefficients) for the $A^1\Pi$ state. Running a single naive least-squares fit to all the absorption data at once failed to converge. Thus, each individual line was fit individually to a Voigt function using a least-squares method to obtain the line centers. The lines that were fit are shown in Fig. 5.4. The Q branches were omitted from these fits. The structure of AlCl is such that while individual rotational transitions in the R and P branches can be distinguished, the spread of the Q branch lines is less than the broadening effects all to be resolved. Thus, the Q lines appear as a single absorption signature, composed of many Q

lines, or Q-forest, between the P and R branches. Our in-cell data was thermally broadened such that the majority of the hyperfine features were unresolved. The complicated nature of this Q-forest is shown in Fig. 5.3.

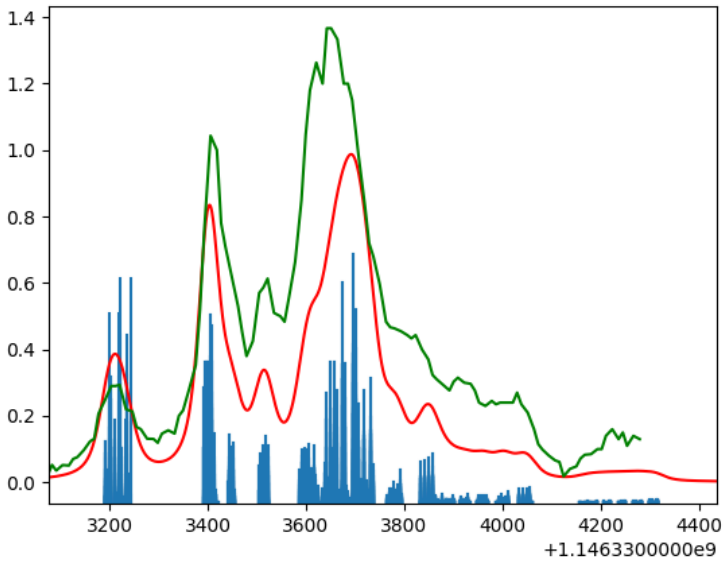

Figure 5.3: An estimation of the structure of the Q-forest (unresolved overlap of Q(0), Q(1), Q(2), etc). Shown is an overlay of preliminary fluorescence data provided by the McCarron lab at the University of Connecticut (green) with the aggregate simulated fluorescence at around 2.5 K (red) of the strongest Q-forest lines (vertical blue lines).

5.4.3 Molecular Constants

Fitting each individual line center yielded a simplified data set line centers. Using the ro-vibrational quantum numbers and line centers, the Dunham coefficients were obtained from applying a least-squares fit two different ways. The first fit was applied separately to the Al_{35} and Al_{37} data to obtain a set of Y_{kl} for each isotope. Due to insufficient signal-to-noise capabilities, the only line centers we had available to fit were from $X^1\Sigma^+(\nu = 0) \rightarrow$

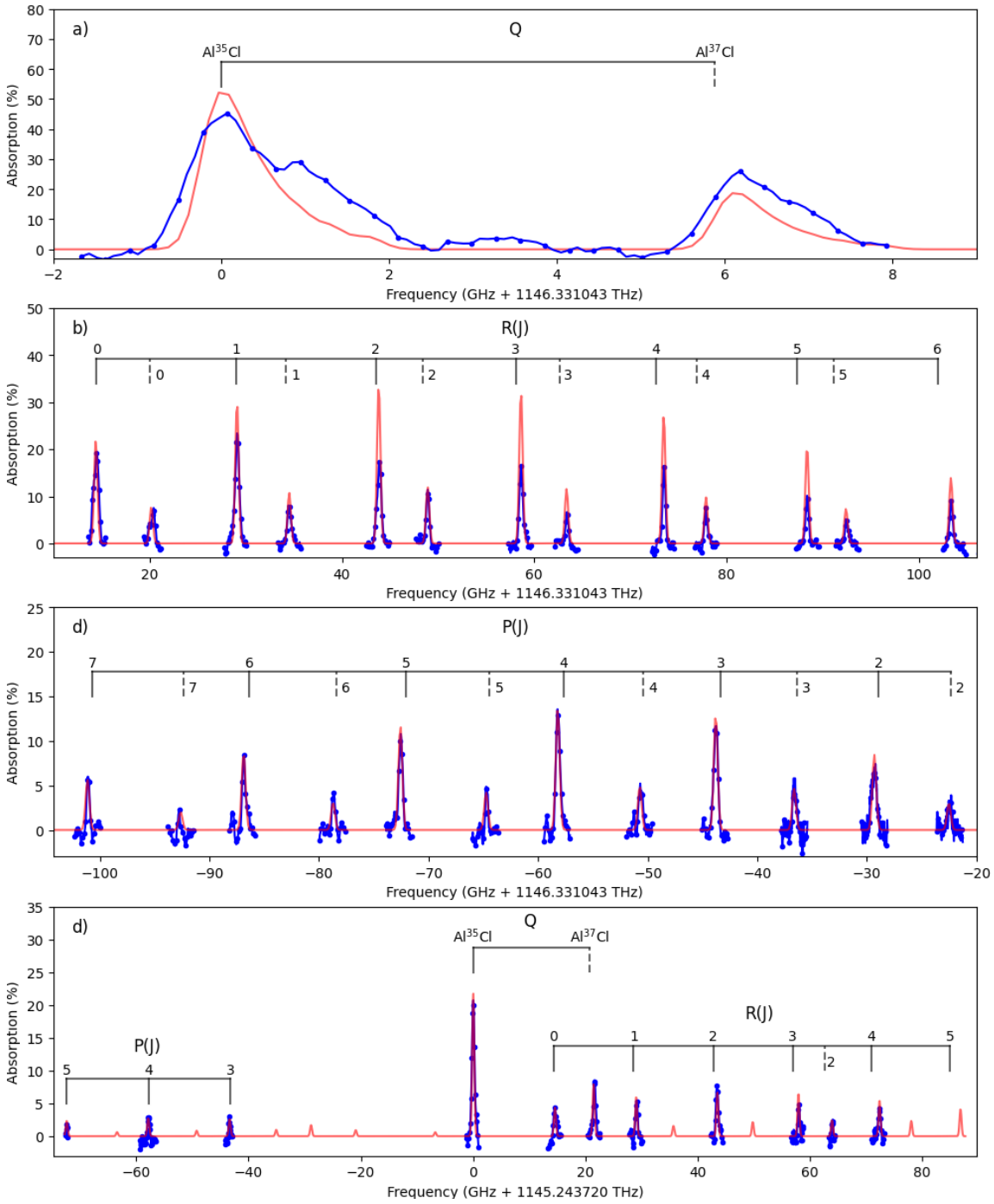

Figure 5.4: Absorption signals for the $X^1\Sigma^+(\nu=0) \rightarrow A^1\Pi(\nu'=0)$ manifold Q (a), R (b), and P (c) branches and $X^1\Sigma^+(\nu=1) \rightarrow A^1\Pi(\nu'=1)$ manifold (d). Data (blue) is shown after a moving 3-point average has been applied. A simulated spectrum (red) created with the molecular constants obtained from fitting the P and R branches is plotted over the data. Theoretical line center calculations (black) are labeled according to J of the $X^1\Sigma^+$ for the $Al^{35}Cl$ (solid) and $Al^{37}Cl$ (dashed) isotopologues.

$A^1\Pi(\nu'=0)$ and $X^1\Sigma^+(\nu=1) \rightarrow A^1\Pi(\nu'=1)$. Thus, to fit the $A^1\Pi$ state, we utilize high precision Dunham coefficients that had previously been measured[21] for the $X^1\Sigma^+$ state.

	$Al^{35}Cl$ (cm^{-1})	$Al^{37}Cl$ (cm^{-1})
Y_{00}	38257.4210(4)	38257.3401(7)
Y_{10}	441.3320(6)	436.2127(6)
Y_{01}	0.25434(2)	0.23833(2)
Y_{11}	-0.00265(3)	

Table 5.1: The fitted Dunham coefficients obtained from individually fitting the line centers for the two isotopologues of AlCl.

The second fit was applied to all the line centers, both isotopes simultaneously, to obtain the mass-reduced Dunham coefficients, U_{kl}. This fit was also a least-squares fit.

U_{00}	38253.33(2)	38253.31(2)
U_{10}	1764.9(2)	1766.1(2)
U_{20}	-83.0(4)	-85.4(4)
U_{01}	3.7377(3)	3.7367(3)
U_{11}	-0.165(2)	-0.157(2)
Δ_{00}^{Cl}		-0.158(7)

Table 5.2: The fitted mass-reduced Dunham coefficients for AlCl with and without the inclusion of a Born-Oppenheimer-breakdown coefficient, Δ_{00}^{Cl}.

The errors for the constants were determined using a Monte-Carlo method. Using the resulting constants, the absorption lines were calculated to verify consistency. Without the inclusion of a Born-Oppenheimer-breakdown coefficient the mean line reproduction error is 72 MHz. When one is included, this error is reduced to 31 MHz. It should be states that introducing this breakdown coefficient

The Dunham coefficients determined above can be used to make estimates of other molecular constants such as the equilibrium bond length, R_e and the Franck-Condon

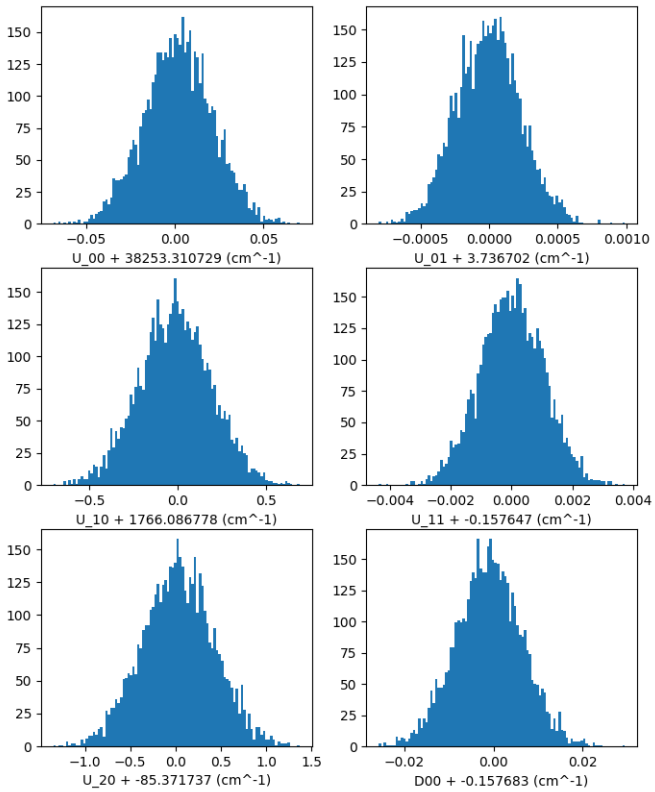

Figure 5.5: Monte-Carlo simulation to determine the error from fitting the mass-reduced Dunham coefficients.

factors. Additionally, they provide predictive power for at which frequency other absorption lines are expected to be observed. For example, the McCarron group at the University of Connecticut located the first vibrational re-pump transition, $X^1\Sigma^+(\nu=1) \rightarrow A^1\Pi(\nu'=0)$, exactly where these constants predicted it to lie.

5.5 Franck-Condon Factors

The Franck-Condon Factors are estimated using harmonic oscillator wave functions. These wave functions depend on the equilibrium bond length (R_e) and the vibrational constant (ω_ν) for the particular vibrational level. The equilibrium bond length can be inferred from the rotational constant (B_ν) using the rigid rotor approximation as

$$R_e = \sqrt{\frac{\hbar}{4\pi\mu B_\nu}} \tag{5.13}$$

where μ is the reduced mass and B_ν can be obtained from the Dunham expansion with

$$B_\nu \approx Y_{01} + Y_{11}(\nu + 1/2) \tag{5.14}$$

The vibrational constant can similarly be obtained with

$$\omega_\nu \approx Y_{10} + Y_{20}(\nu + 1/2) \tag{5.15}$$

There are higher order terms of course, however their order of magnitude is below the level of precision that we can reasonably claim with our data. To compute the Frank-Condon factors, these R_e and ω_ν are plugged in for $A^1\Pi$ and $X^1\Sigma^+$ states and

$$f_{\nu,\nu'} = \langle \psi_\nu | \psi_{\nu'} \rangle \tag{5.16}$$

is evaluated with ψ_ν being the appropriate vibrational wave function. These are normalized such that the sum of the Franck-Condon factors for each excited state is equal to 1.

5.6 Temperature Measurement

Using the P-branch of the $0 \rightarrow 0$ manifold we can measure the rotational temperature. Since we are driving the transition with only tens of μW, the majority of the

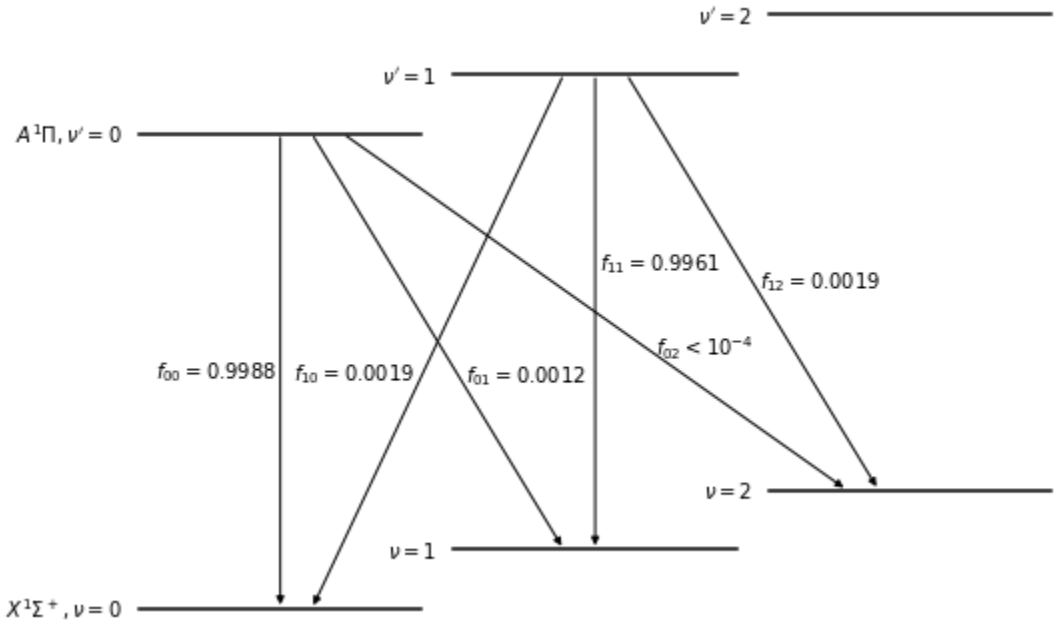

Figure 5.6: Franck-Condon factors, $f_{\nu,\nu'}$, inferred from molecular constants and simple harmonic oscillator wave functions for $\nu' = 0, 1$ transitions.

population resides in the ground electronic state and thus the dependence of the line intensity ($I(J,T)$) can be described using the Hönl-London factors (S_J) and the rotational state thermal populations ($N_J(T)$). For the P-branch, $J = J' - 1$, which when plugged into Eq. (5.9) along with $\Lambda = 0$ results in

$$S_J = \frac{(J - \Lambda - 1)(J - \Lambda)}{2J} = \frac{(J-1)}{2} \tag{5.17}$$

It should be noted, to properly normalize S_J an addition factor of $2J + 1$ is divided out. Under the rigid-rotor approximation, the rotational thermal population's dependent on the temperature (T) can be described as

$$N_J(T) = \frac{(2J+1)e^{-E_J/k_BT}}{Q_{\text{rot}}} \tag{5.18}$$

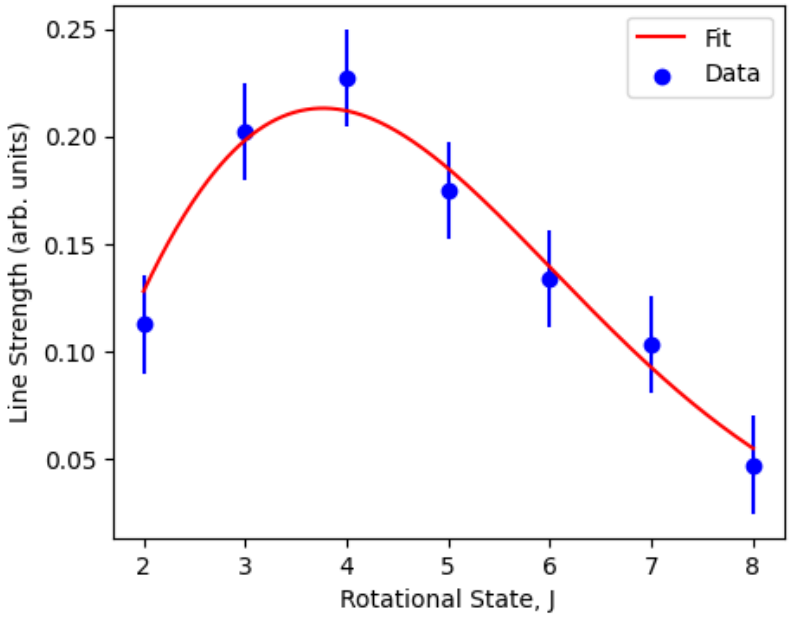

Figure 5.7: Fit (red) for in-cell rotational temperature to line strength data (blue) for the P branch of the X state of AlCl. The fit shown here yields a rotational temperature of 8.3(4) K.

The P-branch is selected for this fit as the data was taken with the same target in the same day, thus preserving the most coherent relative line intensity. The peak height from each line is individually obtained, and then the intensity vs rotational state is fit with a least-squares fit, yielding a rotational temperature of 8.3(4) K.

We found an interesting discrepancy in the ratio of the R-branch lines to the P-branch lines. Even after factoring in the Hönl-London factors the R-branch absorption signals were more pronounced than the P-branch lines. It possible that this could be due to source preparation differences. Another suggested causes is that there is unexpected population in the $A^1\Pi$ state. Since the $A^1\Pi$ has a lifetime of only a few ns, and we are measuring with 50 μW of power (nowhere near saturation limits), it is possible that during the ablation process electronic states higher than $A^1\Pi$ are becoming populated (such as

$B^1\Sigma^+$, etc). To better study this requires a pronounced AlCl signal in the beam, which is a matter of ongoing improvement.

Chapter 6

Target Study

The choice solid precursor target that is ablated to create gas-phase AlCl is not trivial. Due to the highly reactive nature of AlCl, it must be created at the time of the experiment. The initial spectroscopy data presented above was obtained using a hydraulically-pressed pellet of $AlCl_3$. Upon ablation, an observable amount of AlCl was created. This readily available white powder served as a starting point to find absorption lines, however $AlCl_3$ suffers from its reaction with water vapor in the air as can be seen in Fig. 6.1.

Pellets left exposed to atmosphere show signs of degradation within only a few hours and over time, our supply of $AlCl_3$ slowly degraded until the point that we were not able to observe any AlCl being produced. Our chemist collaborators tell us that degradation is due to the salt hydrolysis process

$$AlCl_{3(s)} + 2H_2O_{(l)} \rightarrow AlCl(OH)_{2(l)} + 2HCl_{(l)} \tag{6.1}$$

which produces a noticeable odor of HCl in the storage container for the $AlCl_3$.

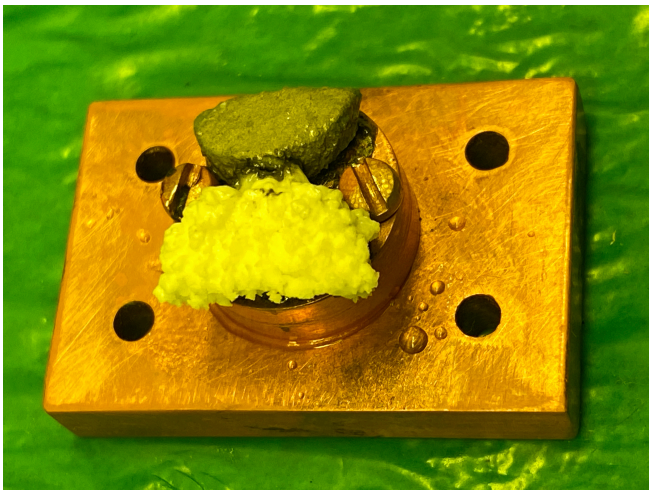

Figure 6.1: A precursor target that has reacted with moisture in the air. The white half of the target was an $AlCl_3$ pellet.

In the search for alternative precursors, we briefly explored aluminum phthalocyanine chloride (chemical structure shown in Fig. 6.2) as a possible precursor. The thought was that with an aluminum and chlorine atom already bonded, it could be easier to extract AlCl from target. As it turns out, this was a gross mis-representation of the nature of the ablation process. The ablation process is not selective in vaporization, so having such a small ratio of AlCl to unwanted byproducts resulted in a nasty, black sludge covering the inside of the cell. Clearly, not every compound that contains aluminum and chlorine is viable for use in an ablation-style vaporization procedure.

6.1 Al:KCl Mixing

Mixing aluminum powder with potassium chloride (KCl) was considered as a precursor due to existing experience with the easy pellet-forming characteristics of KCl. Our lab had prior experience working with KCl to test the ablation laser and scanning capa-

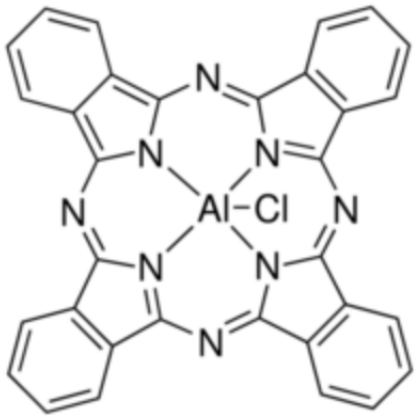

Figure 6.2: Chemical structure for aluminum phthalocyanine chloride. This organic compound was explored as a precursor due to the existence of an Al-Cl bond, however all the carbon and nitrogen renders this organic not viable for AlCl production via ablation.

bilities of the Ti:Sapph laser as potassium's D1 and D2 lines are easily reachable by the Ti:Sapph at 766.701 nm and 770.108 nm. Mixing aluminum powder into the potassium chloride at a molar ratio of 1:1 Al:KCl resulted in observable AlCl from a target that is much slower to react with water in the air. The next step was to determine which Al:KCl molar mixing ratio was optimal for maximal yield of AlCl.

6.2 Laser Setup

To attempt to best capture the results of the ablation process, we prepared a variety of Al:KCl mixes, pressed them into targets, and performed ablation-location-dependent (ALD) absorption measurement. When performing the previous spectroscopy on AlCl, the ablation laser was set to randomly raster over the target to evenly erode the surface. For the target study, we carefully direct the ablation laser to a grid of locations on the target using the actuators on the last mirror that the ablation laser hits before entering the dewar.

Unlike a spectroscopy measurement, the frequency of the measurement laser is not scanned, but rather kept constant at a value corresponding to a large amount of absorption in the atom or molecules being observed. In addition to observing ALD absorption signals from AlCl at 261.5 nm (≈1146.33104 THz), we perform ALD absorption measurements on aluminum and potassium. As previously mentioned, potassium has a $^2S_{1/2} \rightarrow^2 P_{3/2}$ transition that is conveniently within easy tuning range of the raw Ti:Sapph output at 767 nm (≈391.0160 THz). Doubly-convenient, aluminum has an absorption line within easy reach of the output of the SHG cavity at 395 nm (≈759.9052 THz). This means that by utilizing a series of flip-mirror-mounts, the same THG setup detailed above can be easily modified to obtain all three absorption measurements as is shown in Fig. 6.3. All the yield measurements were made using in-cell absorption signals with a helium flow of 4 sccm and an ablation pulse energy of 14 mJ. An interesting side-note: the Stycast 2850 that is used to affix the targets to the target holder has aluminum oxide as an active ingredient. This means that when observing aluminum absorption signals at 395 nm, missing the target yield some aluminum so long as exposed stycast was vaporized. This means that it is important to use the potassium or AlCl data sets to accurately determine the edges of each target.

6.3 Results

ALD data was compared for a range of Al:KCl molar ratios, from 1:25 to 10:1, and fit to a model[34]. Initial expectations were that we would see optimal AlCl yield for a 1:1 molar mixing ratio, as there would be an equal density of aluminum and chlorine atoms in

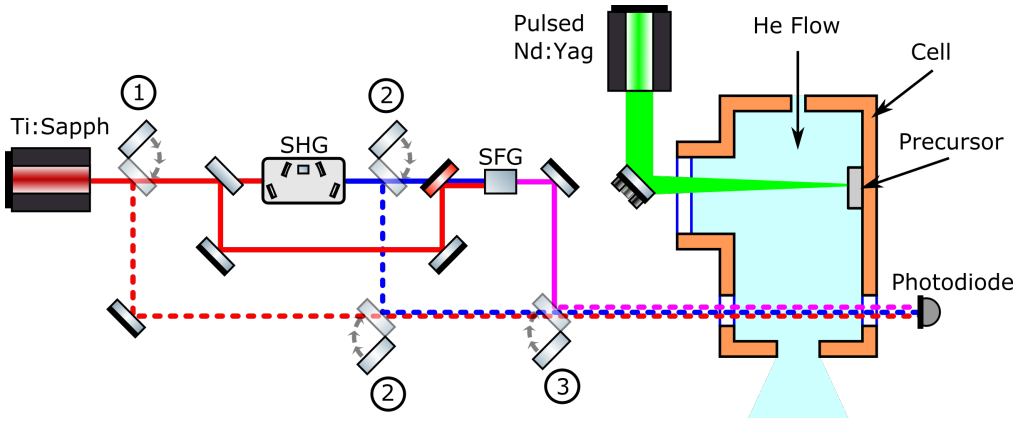

Figure 6.3: Laser setup schematic for the target study. Flip mirrors are added the the existing setup to allow for multiple configurations. Configuration (1) directs the Ti:Sapph output, set to 767 nm, through the cell to measure K absorption. Configuration (2) directs the output of the SHG cavity through the cell to observe Al at 395 nm. Configuration (3) uses the full THG system detailed above to observe AlCl at 261.5 nm.

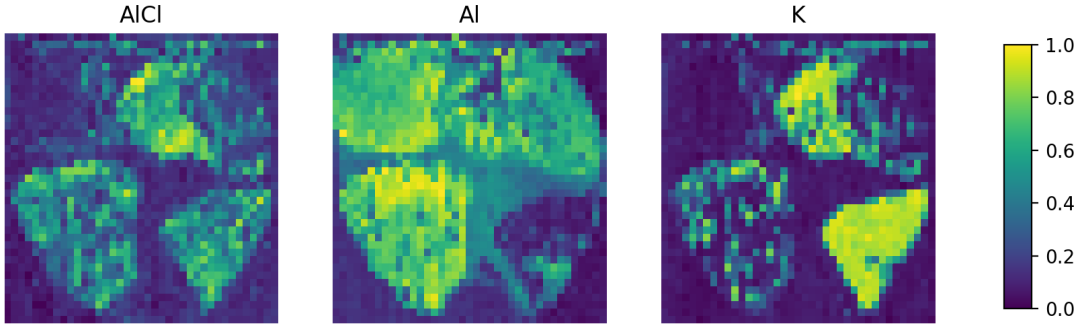

Figure 6.4: A Sample data set including four sub-targets with Al:KCl molar ratios 10:1, 8:1, 5:1, and 1:4 (top left, bottom left, top right, bottom right). From left to right, the images are ALD absorption images of AlCl at 261.5 nm, Al at 395 nm, and K at 767 nm. Each pixel represents the amount of absorption at a location on the target.

Figure 6.5: A photo of a used target that had recently been removed from the dewar. You can clearly see the shiny features near where the three targets meet. We deduce that this must be aluminum that has recondensed onto the surface.

the target. While taking data, we started noticing that in some cases when we removed a used target we noticed shiny patches. The aluminum powder was the logical suspect. Due to the excess build-up of aluminum on the surface, a recondensation model was pursued over an equilibrium model. Fitting this model to the data yielded an optimal molar mixing ratio of 1:1.55[34].

Al:KCl molar ratios were measured out utilizing molecular weights. 1 mol of Al weighs 26.982g and 1 mol of KCl weighs 74.551g. This means that to generate a 1:1 molar ratio a mixing ratio of 1:2.763 by weight is used.

Chapter 7

Slowing and Trapping Yb

As a preliminary to future slowing and trapping of AlCl, it was necessary to test our magneto-optical trap (MOT) coils. We chose ytterbium to perform this test as it has a good cycling transition within easy reach of the LBO crystal in our SHG cavities. This meant no additional crystals needed to be bought. We tested the MOT functionality using a home-built ytterbium oven source and permanent ferromagnet Zeeman slower and successfully created UCR's first MOT!

7.1 Zeeman Slower

In a sentence, Zeeman slowing is the process of exploiting the Zeeman effect to compensate for doppler shift to keep a laser on resonance while laser cooling. When the velocity of the atom is non-zero, the laser light in the molecule-fixed frame is blue-shifted.

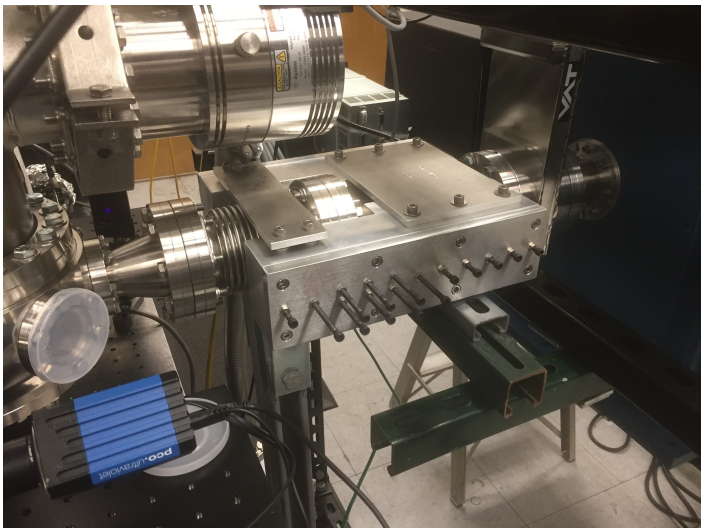

Figure 7.1: A photo of the installed Zeeman slower assembly. The dewar can be seen on the right and the UHV chamber can be seen on the left.

The laser frequency can be red-shifted to compensate, such that

$$\omega = \omega_0 - kv \tag{7.1}$$

where ω is the laser frequency, ω_0 is the resonance frequency of the transition, k is the wavenumber of the laser, and v is the magnitude of the velocity component aligned with the laser axis. In principle, by red-shifting the laser to the appropriate detuning, we can compensate for a single velocity. However, as the molecule slows, the reducing doppler shift will move the laser off-resonance. There are several possible ways to address multiple velocities, including white-light slowing, chirped slowing, and the method presented here, Zeeman slowing. For Zeeman slowing, a spatial-varying magnetic field is applied to address multiple different velocities. This magnetic field, $B(z)$ is chosen such that the Zeeman effect shifts the energy of the transition to meet the condition

$$\omega = \omega_0 - kv + \mu_B B(z) \tag{7.2}$$

When undergoing constant deceleration, the velocity as a function of z is described as

$$v = v_0 \left(1 - \frac{z}{L_0}\right)^{1/2} \tag{7.3}$$

where v_0 is the initial velocity and L_0 is the stopping distance defined as

$$L_0 = \frac{v_0^2}{a_{\max}} \tag{7.4}$$

where $a_{\max}$ is the maximum acceleration the molecule undergoes when cycling photons and is

$$a_{\max} = \frac{F_{\max}}{M} = \frac{\hbar k}{M}\frac{\Gamma}{2} \tag{7.5}$$

where M is the molecule mass, k is the wavenumber of the transition, and Γ is the natural linewidth. Combining everything, the required magnetic profile required to achieve zeeman slowing is

$$\mu_B B(z) = \Delta + k v_0 \left(1 - \frac{z}{v_0^2}\frac{\hbar k}{M}\frac{\Gamma}{2}\right)^{1/2} \tag{7.6}$$

where $\Delta = \omega - \omega_0$.

This magnetic field profile was experimentally implemented by constructing a ferromagnetic Zeeman slower. This slower uses an array of cylindrical ferromagnets. The base body of the slower is aluminum (Al-6061). The ferromagnets are all aligned with their magnetic field pointing in the same direction to generate an approximately uniform magnet field perpendicular to the beam line. The magnets are epoxied to a nut attached to the end of a bolt. The bolt is held by a threaded hole in the side of the slower, allowing for a hex driver to be used to adjust the plunge depth of the magnets. Each magnet moves inside of a channel machined into the aluminum.

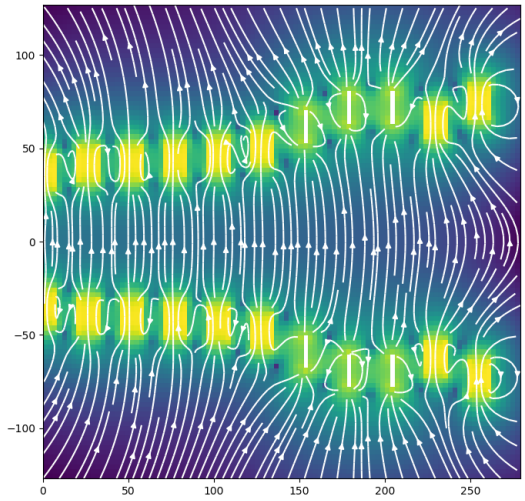

Figure 7.2: A simulation of the Zeeman slower magnetic field through the plane of the magnets. You can clearly see here that some regions are appropriately uniform, however at the ends of the slower the field direction depends on distance from the beam axis.

While this design of Zeeman slower has a very customizable magnetic field profile, it has some design limitations. The resolution of magnetic field shape is limited to by the relatively large size of the ferromagnets used. It is unclear whether or not this field resolution will be useful for something with such a short stopping distance as AlCl (only a few cm), however it should work for a wide variety of atoms. A issue that has arisen using this slower with the CBGB is the large beam-line length that is required to accommodate the slower. Removing the slower allows for a much shorter distance from cell to coils. The long distance could undo any advantage gained by using such a slower.

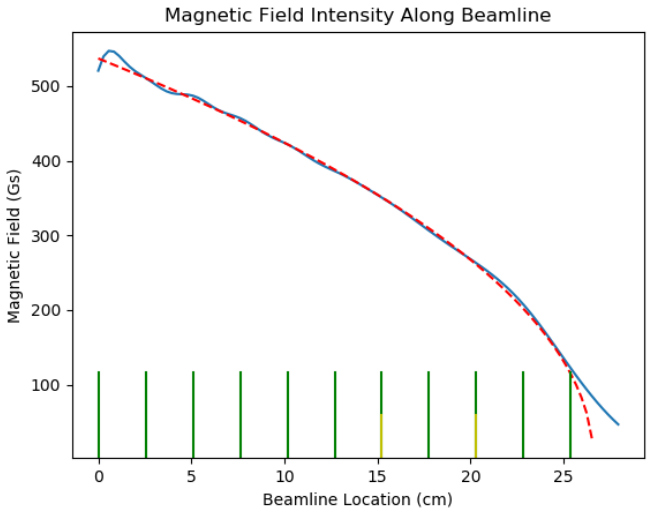

Figure 7.3: On-axis magnetic field intensity comparison between the simulated field (blue) and the ideal slower profile (red dash).

7.2 Magnetic Coils

Instead of opting for in-air magnetic coils that can require hundreds of amps of current and liquid cooling, we use in-chamber coils. The coils are cut with an EDM from a copper plate (Cu 101-OFE). The coils are adhered using the two-component epoxy Stycast 2850 onto an alumina ceramic plate with two coils per ceramic (one on each side). The alumina is mounted onto a copper feedthrough with a piece of kapton sandwiched inside for thermal conductivity. The kapton-wrapped wires are soldered on with flux-less solder to preserve the vacuum and connected to an electrical feedthrough with barrel clamps. The coils are connected such that each piece of alumina has a pair of coils in anti-Helmholtz configuration with the each pair oriented in Helmholtz configuration.

The magnetic field produced by this assembly was simulated to determine the current required to generate the required magnetic field gradient for trapping (≈40 Gs/cm

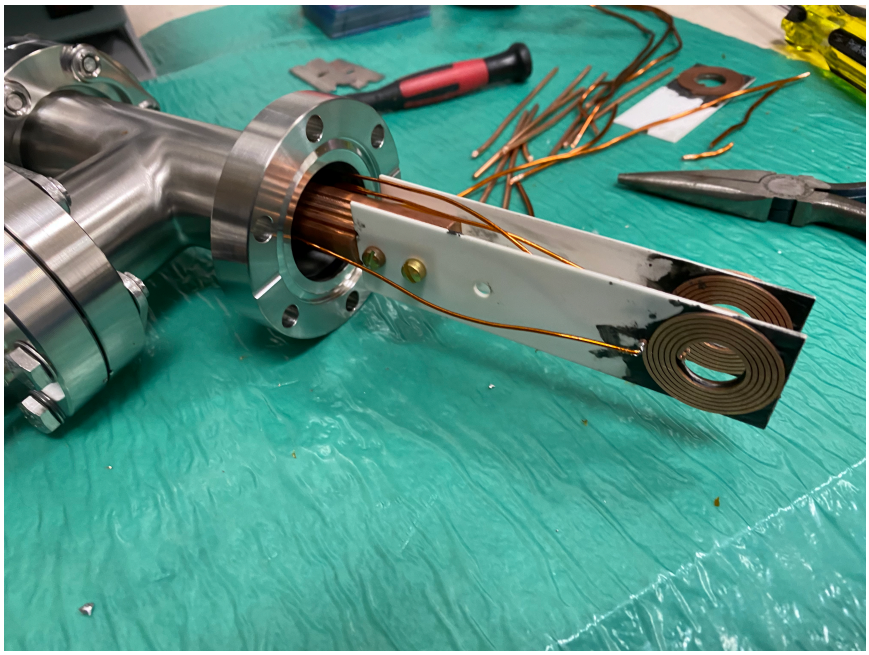

Figure 7.4: MOT coil assembly just prior to being installed in the UHV chamber.

for Yb). I used four sets of five concentric current loops with increasing radius to model the copper coils. The top two sets represent the coils attached to the top and bottom of the top piece of alumina and the bottom sets represent the coils attached to the top and bottom of the bottom piece of alumina.

As can clearly be seen in Fig. 7.5, the current coil produces the desired quadrupole field. The validity of the model was tested in Helmholtz configuration by reversing the current in one of the pieces of alumina and using a magnetometer to measure the field strength in the trapping region for a range of currents. These measurements were compared to a simulation of the Helmholtz configuration with good agreement, indicating that the anti-Helmholtz configuration should be a good model of the system.

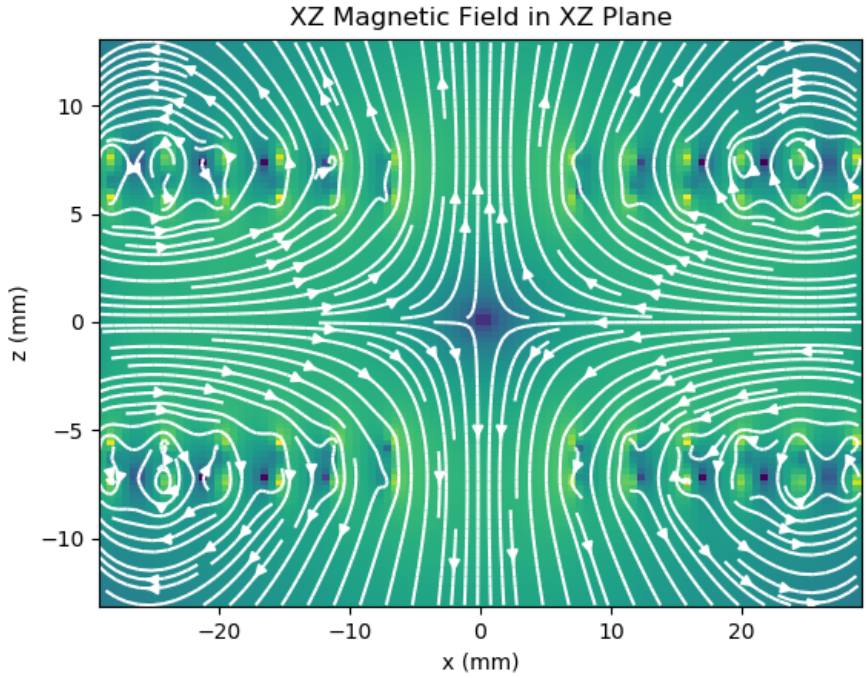

Figure 7.5: Cross section of the simulated MOT coil magnetic field through the XZ plane. Due to the symmetry of the system, these field lines will be approximately the same (up to deviations from the concentric-loop model) for any angle of rotation around the z-axis.

7.3 Laser Setup

The MOT laser setup utilizes a single Ti:Saph laser for all six of the beams. The output of the SHG system is linearly polarized. The combination of a half-wave-plate and polarized-beam-splitter (HWP 1 + PBS 1) is used to split off approximately a third of the incident power for the vertical beams. The remaining 2/3 of the power continues to another half-wave-plate and polarized-beam-splitter (HWP 2 + PBS 2) where it is even split between the two sets of horizontal beams. Each beam in the MOT has the same principle of design. The linearly polarized beam is directed through a quarter-wave-plate (QWP 1, 3, and 5) oriented to convert the linear polarization to circular when passing

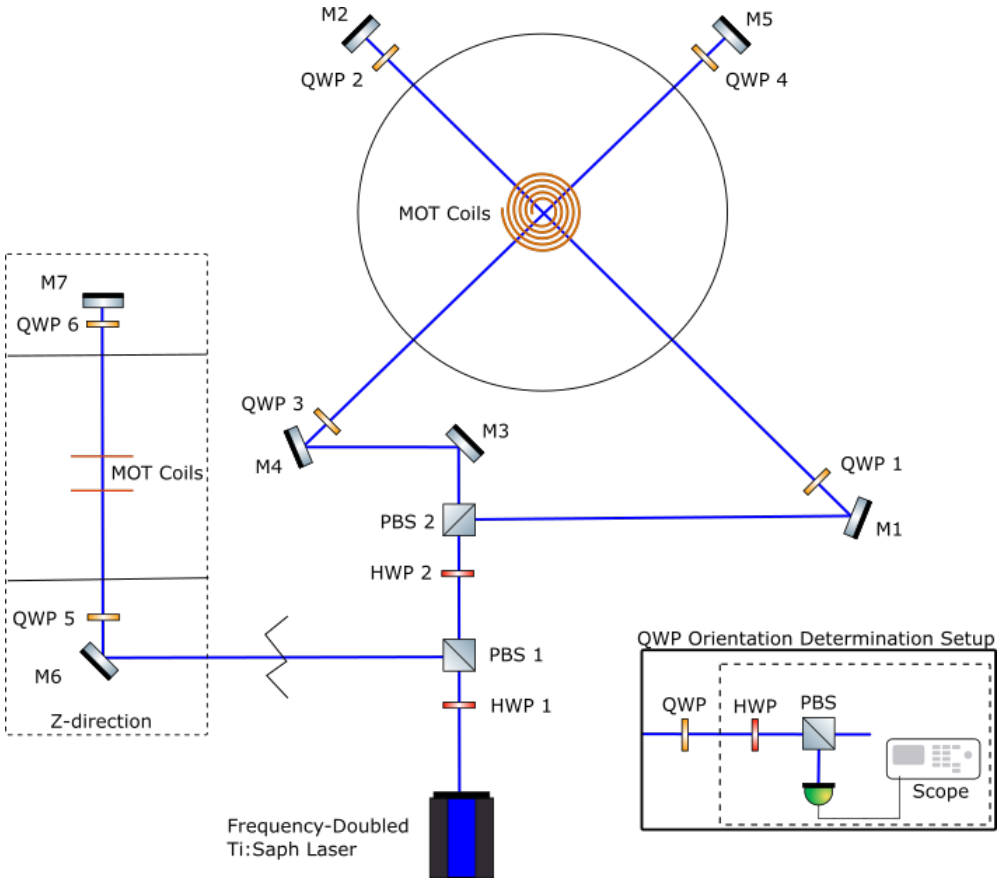

Figure 7.6: MOT Laser Setup

through the trapping region. On the other side of the chamber, another quarter-wave-plate (QWP 2, 4, 6) and a mirror at normal incidence (M2, M5, M7) act as a retroreflector. The quarter-wave-plate converts the circularly-polarized light back to linear, which then reflects off the mirror, back through the quarter-wave-plate converting it to the same handed-ness of circularly-polarized light, however traveling antiparallel to the incident beam. The result is a set of six beams with the appropriate circular polarizations for trapping. For a MOT coil such as this, there are two possible polarizations configurations that are valid. The two incident beams parallel to the optical table must have the same handedness, and the

vertical beam must have the opposite. This necessity arises from the orientations of the magnetic field components in the trapping region.

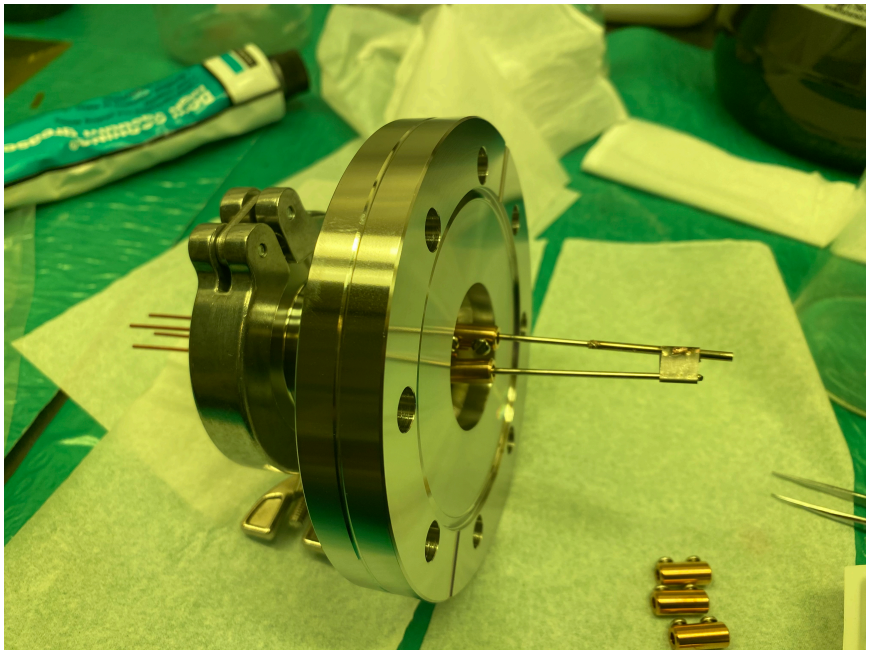

Figure 7.7: A photo of the resistive heating Yb oven used to test the MOT coils.

7.4 Yb MOT

Due to the temperamental nature of our cell, we elected to use an oven source to generate an ytterbium beam. This oven was homebuilt. The main heating element is a piece of 1/8" stainless steel tube. One end of the tube is spot-welded to welding wire and the other is spot-welded to a small strip of tantalum that is wrapped around the tube near the exit of the tube. The other side of the tantalum strip is spot-welded to more welding wire. The two wires are attached to two pins on a CF vacuum feedthrough. By attaching

a current driver to the air-side of these two pins, we are able to heat the oven and produce a hot beam of Yb.

The Zeeman slower is particularly helpful for a hot source such as this. Without the Zeeman slower, the population of Yb below the capture velocity of the trap will be small, and thus the MOT will be dim. Actively slowing allowed for trapping of a larger velocity-range of atoms. Using this oven source combined with the Zeeman slower, ytterbium atoms were successfully trapped, marking the first MOT to be created at the University of California, Riverside. This successful test shows that this MOT coils configuration is in working order and can be used for more traps.

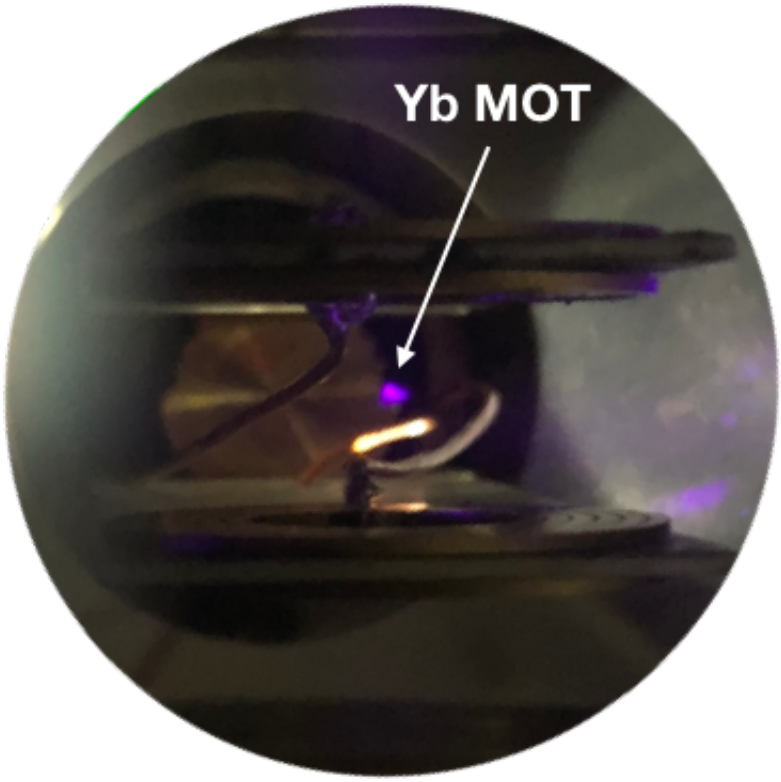

Figure 7.8: The University of California, Riverside's first MOT. This MOT was trapped by Zeeman slowing a hot ytterbium beam from an oven source.

Chapter 8

Conclusions

In this thesis I have derived the dominant $X^1\Sigma^+$ and $A^1\Pi$ Hamiltonian terms with a brief teaser of the $a^3\Pi$ state. I have described a laser system and cold source to perform the first precision studies of the $X^1\Sigma^+ \rightarrow A^1\Pi$ in AlCl. Using this system, I performed absorption spectroscopy on the $\nu = 0$ and $\nu = 1$ vibrational states, observing P,Q, and R branches. This lines were measured to a level of precision $\approx$100 times better than previous work. Knowing the locations of these lines to this new level of precision allows them to be easily relocated for use in cold experiments. From fitting these observed lines, I have obtained molecular constants for the $A^1\Pi$. Using these constants I have deduced Franck-Condon factors for the cycling transition of $X^1\Sigma^+(\nu = 0) \rightarrow A^1\Pi(\nu' = 0)$ to be 99.88% in good agreement with theoretical predictions. Since this Franck-Condon factor is close to 1, AlCl remains a good candidate for laser slowing. In this thesis I also discuss work done to select an optimal precursor target to ablate into AlCl using a mixture of aluminum powder and potassium chloride. Finally, I presented the magneto-optical-trap setup I constructed

and its successful test on ytterbium to create the University of California, Riverside's first MOT.

8.1 Dark States

A prevalent problem that must be addressed when laser cooling molecules is the existence of dark states. Dark states are quantum states that the molecule can be cycled into that do not have an exit pathway. If these states are accessible, it takes only a few photons to drive a molecule into a dark state, thus rendering it inert. Dark states must be addressed, otherwise they render a molecule unable to be slowed with a laser.

These dark states can be identified using two methods. One method would be to perform a numerical optical-Bloch-equation (OBE) calculation. One would expect dark states to accumulate population as the transition evolves. A more analytical discovery method would be to find the null-space of the matrix[20]

$$A_{ij} = \sum_{k,q} e^{-i\Delta_{k,F,F'}t}(-1)^q d^q_{ij} E^k_{-q} \tag{8.1}$$

where laser frequency ω_k, excited state frequency $\omega_{F'}$, and ground state frequency ω_F give $\Delta_{k,F,F'} = \omega_k - (\omega_{F'} - \omega_F)$. d^q_{ij} is the dipole transition matrix element and E^k_{-q} is the electric field of the laser. Numerically finding the null-space of this matrix yields the set of dark state vectors, $\mathbf{a}$ such that

$$\mathbf{A} \cdot \mathbf{a} = 0 \tag{8.2}$$

If the similarities between AlF and AlCl continue, then we would expect that there will be some dark states that are mixtures of different F_1 states. Understanding this better is a

matter of ongoing research. The Truppe group is in the process of trying to slow and trap AlF. They have had their preliminary spectroscopy results since 2019[48], however they have been unable to trap AlF as of yet. One of the primary technical hurdles they are trying to overcome is reportedly the need for laser upgrades to address dark states.

8.2 Laser Upgrades

The tens of μW of UV laser power that the single-pass SFG setup produces is simply insufficient to perform laser slowing experiments, let along worry about dark states. There are currently three efforts underway to create a 261.5 nm source with significantly more power. I will briefly mention them here, but leave the details to appear in future theses.

8.2.1 SFG Bowtie

The laser configuration used for this thesis utilizes a BBO crystal in single-pass configuration to undergo a SFG process to combine a 784.5 nm photon and a 392.3 nm photon to generate a 261.5 nm photon. This can be converted to a bowtie resonance cavity by replacing the dichroic with a mirror mounted on a ring piezo. The piezo must be a ring so that the red beam can pass through the center of it to enter the cavity.

There are complications involved with making a cavity resonant for two different wavelengths. To compensate for this, a pair of Brewster plates attached to galvo motors could be employed. These would be actively driven in reference to an HC lock using the back-reflection of the blue beam. This means there are two simultaneous HC locks at play

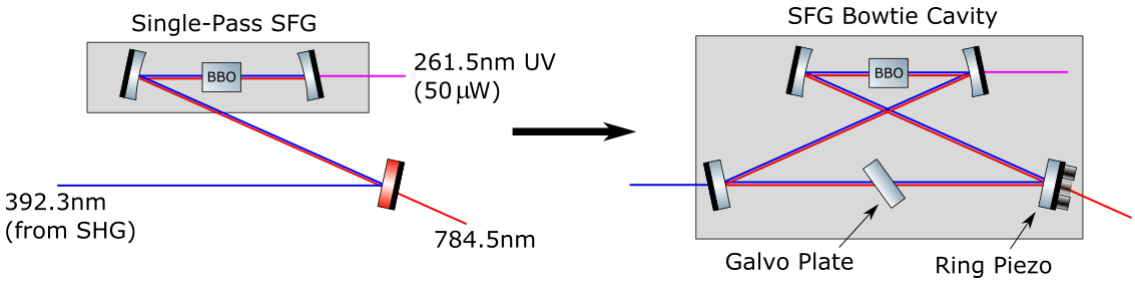

Figure 8.1: Sketch of how to upgrade the single-pass configuration into a possible bowtie resonance cavity configuration.

in the SFG setup, the red one locking via the piezo and the blue one locking via the galvo plate.

Successful locking of this bowtie cavity can turn the current 50 μW to tens or hundreds of mW of UV. This amount of power, while still less than other systems on the market, will allow for fluorescence measurements of AlCl and can be used to address repumping transitions.

8.2.2 Doubled Vexlum

Another system that is under construction at the moment is a frequency-doubled Vexlum. The Vexlum has a commercial internal doubling cavity to produce 523 nm green light. Then a home-built SHG doubling cavity is used to double the 523 nm light into 261.5 nm. A big upside to this system is that, aside from the laser, there is only one active component that needs to be electronically stabilized, as opposed to the three HC locks that are necessary for the completed THG system.

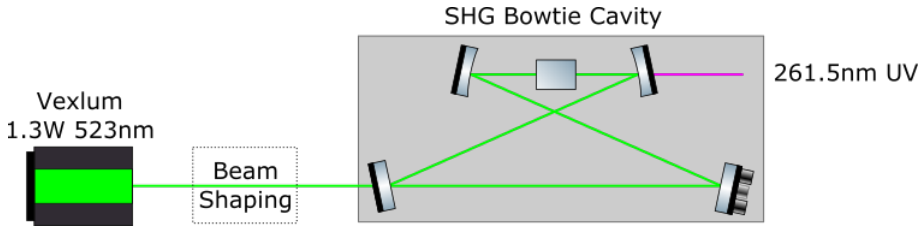

Figure 8.2: Sketch of how to use a SHG cavity to frequency-double a Vexlum laser.

8.2.3 Quadrupoled Fiber

The McCarron lab at the University of Connecticut has recently been successful in generating a 2W UV laser beam from a quadrupoled fiber laser (two sequential SHG processes)[36]. At present, this system represents the most powerful CW 261.5 nm UV system. This amount of power would be more than enough to further study laser slowing AlCl. As such the lab has purchased a pair similar laser systems which will be assembled in the near future.

8.3 Different Chloride Sources

I will only briefly mention here that a handful of other chlorides to mix with aluminum were preliminarily explored as precursor targets (i.e. Al + $MgCl_2$). Magnesium chloride mixed with aluminum was the only one to have comparable yield to the potassium chloride mix. Additionally, exploration is underway to determine if it is possible to use a pure aluminum precursor target and ablate it into a chloride gas that is flowed into the cell. Such a flow would require the addition of a thermally isolated gas fill line (to prevent freezing) and would require a gas containing adequate chlorine that can be worked with

safely. Finding such a gas and modifying the cell to flow in such a gas is an area would reduce the number of times that the dewar would need to be opened as a solid metal target ablates for longer than a pressed one. A reduction in opening frequency could reduce the speed at which the sorbs degrade.

8.4 Final Thoughts

When I started my studies as the first graduate student in the Hemmerling lab, I joined a lab with an empty optical table. As I finish my time in the Hemmerling lab, I

leave the lab a little different than when I started.

There is a saying that as a graduate student, you learn more and more, about less and less, until eventually you know everything about nothing at all. A proper scientist shouldn't say they know everything, however I have certainly learned enough to know AlCl very intimately. I will look back fondly on my time in the Hemmerling lab as I continue my career. Live long and prosper!

Bibliography

[1] The ACME ACME Collaboration, J Baron, W C Campbell, D DeMille, J M Doyle, G Gabrielse, Y V Gurevich, P W Hess, N R Hutzler, E Kirilov, I Kozyryev, B R O'Leary, C D Panda, M F Parsons, E S Petrik, B Spaun, A C Vutha, and A D West. Order of magnitude smaller limit on the electric dipole moment of the electron. *Science*, 343(6168):269–72, jan 2021.

[2] Parul Aggarwal, Hendrick L. Bethlem, Anastasia Borschevsky, Malika Denis, Kevin Esajas, Pi A.B. Haase, Yongliang Hao, Steven Hoekstra, Klaus Jungmann, Thomas B. Meijknecht, Maarten C. Mooij, Rob G.E. Timmermans, Wim Ubachs, Lorenz Willmann, and Artem Zapara. Measuring the electric dipole moment of the electron in BaF. *European Physical Journal D*, 72(11):197, nov 2021.

[3] M. Agúndez, J. P. Fonfría, J. Cernicharo, C. Kahane, F. Daniel, and M. Guélin. Molecular abundances in the inner layers of IRC∼+10216. *Astronomy and Astrophysics*, 543:A48, 2021.

[4] Ralf Albrecht, Michael Scharwaechter, Tobias Sixt, Lucas Hofer, and Tim Langen. Buffer-gas cooling, high-resolution spectroscopy, and optical cycling of barium monofluoride molecules. *Physical Review A*, 101(1):013413, jan 2021.

[5] Loïc Anderegg, Benjamin L. Augenbraun, Eunmi Chae, Boerge Hemmerling, Nicholas R. Hutzler, Aakash Ravi, Alejandra Collopy, Jun Ye, Wolfgang Ketterle, and John M. Doyle. Radio Frequency Magneto-Optical Trapping of CaF with High Density. *Physical Review Letters*, 119(10):103201, sep 2021.

[6] Benjamin L. Augenbraun, Zack D. Lasner, Alexander Frenett, Hiromitsu Sawaoka, Calder Miller, Timothy C. Steimle, and John M. Doyle. Laser-cooled polyatomic molecules for improved electron electric dipole moment searches. *New Journal of Physics*, 22(2):22003, feb 2021.

[7] J. T. Bahns, W. C. Stwalley, and P. L. Gould. Laser cooling of molecules: A sequential scheme for rotation, translation, and vibration. *Journal of Chemical Physics*, 104(24):9689, 2021.

[8] J. F. Barry, D. J. McCarron, E. B. Norrgard, M. H. Steinecker, and D. DeMille. Magneto-optical trapping of a diatomic molecule. *Nature*, 512(7514):286–289, aug 2021.

[9] Louis Baum, Nathaniel B. Vilas, Christian Hallas, Benjamin L. Augenbraun, Shivam Raval, Debayan Mitra, and John M. Doyle. 1D Magneto-Optical Trap of Polyatomic Molecules. *Physical Review Letters*, 124(13):133201, mar 2021.

[10] William B. Cairncross, Daniel N. Gresh, Matt Grau, Kevin C. Cossel, Tanya S. Roussy, Yiqi Ni, Yan Zhou, Jun Ye, and Eric A. Cornell. Precision Measurement of the Electron's Electric Dipole Moment Using Trapped Molecular Ions. *Phys. Rev. Lett.*, 119(15):153001, oct 2021.

[11] Lincoln D Carr, David DeMille, Roman V Krems, and Jun Ye. Cold and ultracold molecules: science, technology and applications. *New Journal of Physics*, 11(5):055049, may 2021.

[12] J Cernicharo and M Guelin. Metals in IRC +10216 : detection of NaCl, AlCl, and KCl, and tentative detection of AlF. *Astronomy and Astrophysics*, 183:L10–L12, sep 2021.

[13] Tao Chen, Wenhao Bu, and Bo Yan. Radiative deflection of a BaF molecular beam via optical cycling. *Physical Review A*, 96(5):053401, nov 2021.

[14] Alejandra L. Collopy, Shiqian Ding, Yewei Wu, Ian A. Finneran, Loïc Anderegg, Benjamin L. Augenbraun, John M. Doyle, and Jun Ye. 3D Magneto-Optical Trap of Yttrium Monoxide. *Physical Review Letters*, 121(21):213201, nov 2021.

[15] J. R. Daniel, C. Wang, K. Rodriguez, T. Lewis, A. Teplukhin, B. Kendrick, C. Bardeen, and B. Hemmerling. Spectroscopy on the X1Σ+ - A1Π Transition of Buffer-Gas Cooled AlCl. *Physical Review A*, 104:012801, may 2021.

[16] M. Daprà, M. L. Niu, E. J. Salumbides, M. T. Murphy, and W. Ubachs. Constraint on a cosmological variation in the proton-to-electron mass ratio from electroinc CO absorption. *The Astrophysical Journal*, 826(2):192, jul 2021.

[17] D. DeMille. Quantum Computation with Trapped Polar Molecules. *Physical Review Letters*, 88(6):067901, jan 2021.

[18] Maximilian Doppelbauer, Nicole Walter, Simon Hofsäss, Silvio Marx, H. Christian Schewe, Sebastian Kray, Jesús Pérez-Ríos, Boris G. Sartakov, Stefan Truppe, and Gerard Meijer. Characterisation of the $b3\Sigma+, v = 0$ State and Its Interaction with the $A1\Pi$ State in Aluminium Monofluoride. *Molecular Physics*, 119(1-2):e1810351, aug 2021.

[19] N. J. Fitch, J. Lim, E. A. Hinds, B. E. Sauer, and M. R. Tarbutt. Methods for measuring the electron EDM using ultracold YbF molecules. *Quantum Sci. Technol.*, 6:014006, sep 2021.

[20] N J Fitch and M R Tarbutt. Laser cooled molecules. *arXiv:2103.00968*, 2021.

[21] H. G. Hedderich, M. Dulick, and P. F. Bernath. High resolution emission spectroscopy of AlCl at 20 μ. *The Journal of Chemical Physics*, 99(11):8363–8370, dec 2021.

[22] Kristine D. Hensel, Christian Styger, Wolfgang Jäger, A. J. Merer, and M. C.L. L. Gerry. Microwave spectra of metal chlorides produced using laser ablation. *The Journal of Chemical Physics*, 99(5):3320–3328, sep 2021.

[23] J. Hoeft, T. Törring, and E. Tiemann. Hyperfeinstruktur von AlCl und AlBr / Hyperfine Structure of AlCl and AlBr. *Zeitschrift für Naturforschung A*, 28(7):1066–1068, jan 2021.

[24] Nicholas R. Hutzler. Polyatomic molecules as quantum sensors for fundamental physics. *Quantum Science and Technology*, 5(4):44011, oct 2021.

[25] Nicholas R. Hutzler, Hsin-I I. Lu, and John M. Doyle. The Buffer Gas Beam: An Intense, Cold, and Slow Source for Atoms and Molecules. *Chemical Reviews*, 112(9):4803–4827, sep 2021.

[26] T. A. Isaev, S. Hoekstra, and R. Berger. Laser-cooled RaF as a promising candidate to measure molecular parity violation. *Physical Review A*, 82(5):052521, 2021.

[27] G. Z. Iwata, R. L. McNally, and T. Zelevinsky. High-resolution optical spectroscopy with a buffer-gas-cooled beam of BaH molecules. *Physical Review A*, 96(2):022509, aug 2021.

[28] Ivan Kozyryev, Louis Baum, Leland Aldridge, Phelan Yu, Edward E. Eyler, and John M. Doyle. Coherent Bichromatic Force Deflection of Molecules. *Physical Review Letters*, 120(6):063205, feb 2021.

[29] Ivan Kozyryev, Louis Baum, Kyle Matsuda, Benjamin L. Augenbraun, Loic Anderegg, Alexander P. Sedlack, and John M. Doyle. Sisyphus Laser Cooling of a Polyatomic Molecule. *Physical Review Letters*, 118(17):173201, apr 2021.

[30] Ivan Kozyryev and Nicholas R. Hutzler. Precision Measurement of Time-Reversal Symmetry Violation with Laser-Cooled Polyatomic Molecules. *Physical Review Letters*, 119(13):133002, sep 2021.

[31] R. V. Krems. Cold controlled chemistry. *Physical Chemistry Chemical Physics*, 10(28):4079, jul 2021.

[32] Ian C. Lane. Ultracold fluorine production via Doppler cooled BeF. *Physical Chemistry Chemical Physics*, 14(43):15078, oct 2021.

[33] Stephen R. Langhoff, Charles W. Bauschlicher, and Peter R. Taylor. Theoretical studies of AlF, AlCl, and AlBr. *The Journal of Chemical Physics*, 88(9):5715–5725, may 2021.

[34] Taylor N. Lewis, Chen Wang, John R. Daniel, Madhav Dhital, Christopher J. Bardeen, and Boerge Hemmerling. Optimizing Pulsed-Laser Ablation Production of AlCl Molecules for Laser Cooling. *Physical Chemistry Chemical Physics*, 23:22785, aug 2021.

[35] J. Lim, J.R. Almond, M.A. Trigatzis, J.A. Devlin, N.J. Fitch, B.E. Sauer, M.R. Tarbutt, and E.A. Hinds. Laser Cooled YbF Molecules for Measuring the Electron's Electric Dipole Moment. *Physical Review Letters*, 120(12):123201, mar 2021.

[36] D. J. McCarron, J. C. Shaw, and S. Hannig. Stable 2 W continuous-wave 261.5 nm laser for cooling and trapping aluminum monochloride. *Optics Express, Vol. 29, Issue 23, pp. 37140-37149*, 29(23):37140–37149, nov 2021.

[37] Daniel McCarron. Laser cooling and trapping molecules. *Journal of Physics B: Atomic, Molecular and Optical Physics*, 51(21):212001, oct 2021.

[38] W. K. McGregor, J. A. Drakes, K. S. Beale, and F. G. Sherrell. The AICI absorption feature in solid rocket plume radiation. In *AIAA 27th Thermophysics Conference, 1992*. American Institute of Aeronautics and Astronautics Inc, AIAA, 2021.

[39] A. Micheli, G. K. Brennen, and P. Zoller. A toolbox for lattice-spin models with polar molecules. *Nature Physics*, 2(5):341–347, may 2021.

[40] Debayan Mitra, Nathaniel B Vilas, Christian Hallas, Loïc Anderegg, Benjamin L Augenbraun, Louis Baum, Calder Miller, Shivam Raval, and John M Doyle. Direct laser cooling of a symmetric top molecule. *Science*, 369(6509):1366–1369, sep 2021.

[41] K.-K. K. Ni, S. Ospelkaus, D. Wang, G. Quéméner, B. Neyenhuis, M. H.G. G. De Miranda, J. L. Bohn, J. Ye, and D. S. Jin. Dipolar collisions of polar molecules in the quantum regime. *Nature*, 464(7293):1324–1328, apr 2021.

[42] E. B. Norrgard, E. R. Edwards, D. J. McCarron, M. H. Steinecker, D. DeMille, Shah Saad Alam, S. K. Peck, N. S. Wadia, and L. R. Hunter. Hyperfine structure of the B 3 Π1 state and predictions of optical cycling behavior in the XB transition of TlF. *Physical Review A*, 95(6):062506, jun 2021.

[43] Matthew J. O'Rourke and Nicholas R. Hutzler. Hypermetallic polar molecules for precision measurements. *Physical Review A*, 100(2):022502, aug 2021.

[44] S. Ospelkaus, K-K K. Ni, D. Wang, M. H.G. G de Miranda, B. Neyenhuis, G. Quéméner, P. S. Julienne, J. L. Bohn, D. S. Jin, and J. Ye. Quantum-state controlled chemical reactions of ultracold potassium-rubidium molecules. *Science*, 327(5967):853, feb 2021.

[45] Ram Samujh Ram, S B Rai, K N Upadhya, and D K Rai. The A 1 Π- X 1 Σ + , a 3 Π- X 1 Σ + and b 3 Σ + - a 3 Π Systems of AlCl. *Physica Scripta*, 26(5):383–397, nov 2021.

[46] Xiao Ying Ren, Zhi Yu Xiao, Yong Liu, and Bing Yan. Configuration interaction study on the low-lying states of AlCl molecule. *Chinese Physics B*, 30(5):053101, dec 2021.

[47] Benjamin K. Stuhl, Brian C. Sawyer, Dajun Wang, and Jun Ye. Magneto-optical Trap for Polar Molecules. *Physical Review Letters*, 101(24):243002, dec 2021.

[48] S. Truppe, S. Marx, S. Kray, M. Doppelbauer, S. Hofsäss, H. C. Schewe, N. Walter, J. Pérez-Riós, B. G. Sartakov, and G. Meijer. Spectroscopic characterization of aluminum monofluoride with relevance to laser cooling and trapping. *Physical Review A*, 100(5):052513, nov 2021.

[49] S. Truppe, H. J. Williams, M. Hambach, L. Caldwell, N. J. Fitch, E. A. Hinds, B. E. Sauer, and M. R. Tarbutt. Molecules cooled below the Doppler limit. *Nature Physics*, 13(12):1173–1176, aug 2021.

[50] T Tsuji. Molecular abundances in stellar atmospheres. II. *Astronomy and Astrophysics*, 23:411, mar 2021.

[51] Mingjie Wan, Di Yuan, Chengguo Jin, Fanhou Wang, Yujie Yang, You Yu, and Juxiang Shao. Laser cooling of the AlCl molecule with a three-electronic-level theoretical model. *The Journal of Chemical Physics*, 145(2):024309, jul 2021.

[52] H J Williams, S Truppe, M Hambach, L Caldwell, N J Fitch, E A Hinds, B E Sauer, and M R Tarbutt. Characteristics of a magneto-optical trap of molecules. *New Journal of Physics*, 19(11):113035, nov 2021.

[53] Jian Gang Xu, Cong Ying Zhang, and Yun Guang Zhang. Vibronic spectra of aluminium monochloride relevant to circumstellar molecule. *Chinese Physics B*, 29(3):033102, mar 2021.

[54] Liang Xu, Yanning Yin, Bin Wei, Yong Xia, and Jianping Yin. Calculation of vibrational branching ratios and hyperfine structure of 24Mg19 F and its suitability for laser cooling and magneto-optical trapping. *Physical Review A*, 93(1):013408, jan 2021.

[55] Rong Yang, Bin Tang, and Tao Gao. Ab intio study on the electronic states and laser cooling of AlCl and AlBr. *Chinese Physics B*, 25(4):043101, apr 2021.

[56] Kouji Yasuda, Kunio Saegusa, and Toru H. Okabe. New Method for Production of Solar-Grade Silicon by Subhalide Reduction. *Materials Transactions*, 50(12):2873–2878, dec 2021.

[57] Kouji Yasuda, Kunio Saegusa, and Toru H. Okabe. Production of solar-grade silicon by halidothermic reduction of silicon tetrachloride. *Metallurgical and Materials Transactions B: Process Metallurgy and Materials Processing Science*, 42(1):37–49, feb 2021.

[58] Xin Ye, Mingyang Guo, Maykel L. González-Martínez, Goulven Quéméner, and Dajun Wang. Collisions of ultracold 23Na87Rb molecules with controlled chemical reactivities. *Science Advances*, 4(1):eaaq0083, jan 2021.

[59] S. F. Yelin, K. Kirby, and Robin Côté. Schemes for robust quantum computation with polar molecules. *Physical Review A*, 74(5):050301(R), nov 2021.

[60] Mahdi Yousefi and Peter F. Bernath. Line Lists for AlF and AlCl in the X 1 Σ + Ground State . *The Astrophysical Journal Supplement Series*, 237(1):8, jul 2021.

[61] Phelan Yu, Lawrence W. Cheuk, Ivan Kozyryev, and John M. Doyle. A scalable quantum computing platform using symmetric-Top molecules. *New Journal of Physics*, 21(9):093049, sep 2021.

[62] Phelan Yu and Nicholas R. Hutzler. Probing Fundamental Symmetries of Deformed Nuclei in Symmetric Top Molecules. *Physical Review Letters*, 126(2):023003, jan 2021.

Appendix A

Constants

Constant	Value	Unit	Description
e	1.602176462(63)	10^{-19} C	Electron Charge
$\hbar$	1		Planck Constant
k_B	2.083661912	10^4 MHz $\cdot$ K^{-1}	Boltzmann Constant
m_e	9.1093837015	10^{-31} kg	Electron Mass
amu	1.66053873(13)	10^{-27} kg	Atomic Mass Unit
c	299792458	m $\cdot$ s^{-1}	Speed of Light
μ_N	7.6225932291	10^{-4} MHz $\cdot$ Gs^{-1}	Nuclear Magneton
μ_B	1.39962449361	MHz $\cdot$ Gs^{-1}	Bohr Magneton
g_s	2.0023193043737(82)		Free Electron g-factor

Table A.1: Universal Constants of Nature

Atom	Iso.	Mass(amu)	Abun(%)	Spin($\hbar$)	MM(μ_N)	g-factor
Al	27	26.981539	100.0	5/2	+3.64151	+1.4566028
Cl	35	34.968852	75.77	3/2	+0.82187	+0.5479162
	37	36.965903	24.23	3/2	+0.68412	+0.4560824

Table A.2: Nuclear properties for Al and Cl obtained from Appendix B of Brown and Carrington. MM is the nuclear magnetic moment and EQM is the electric quadrupole moment. Nuclear g-factors were obtained from easyspin.org.

MR Dunham (cm^{-1})	$X^1\Sigma^+$[21]	$A^1\Pi$[15]
U_{00}	0.0	38253.31(2)
U_{10}	1880.20216(282)	1766.1(2)
U_{20}	-32.01210(103)	-85.4(4)
10^1U_{30}	3.95186(714)	
10^3U_{40}	-4.802(161)	
U_{01}	3.71517408(165)	3.7367(3)
10^2U_{11}	-9.5756544(573)	-15.7(2)
10^3U_{21}	1.087167(714)	
10^6U_{31}	-4.384(244)	
10^5U_{02}	-5.80214265	
10^7U_{12}	3.87217711	
10^8U_{22}	2.84009761	
10^9U_{32}	-1.37741377	
$10^{10}U_{03}$	-1.57686816	
$10^{11}U_{13}$	2.12545554	
$10^{12}U_{23}$	-1.05413605	
$10^{14}U_{04}$	-0.35748725	
$10^{16}U_{14}$	5.98550331	
$10^{17}U_{24}$	-3.16634502	
$10^{20}U_{05}$	3.85240049	
$10^{20}U_{15}$	-1.355155 50	
$10^{24}U_{06}$	2.99990752	
$10^{25}U_{16}$	-2.93174963	
$10^{29}U_{07}$	5.14820733	
$10^{34}U_{08}$	5.65735166	
Δ_{00}^{Cl}	-	-0.158(7)
Δ_{10}^{Cl}	-1.2238(951)	
Δ_{01}^{Cl}	-1.4432(287)	
Hyperfine (MHz)	$X^1\Sigma^+$[22]	$A^1\Pi$
a_{Al}	-	153.1(8)
a_{Cl}	-	32(2)
$(eQq_0)_{Al}$	-30.4081(27)	
$(eQq_0)_{Cl}$	-8.8290(35)	
$(eQq_2)_{Al}$	-	96(14)
Misc		
Γ	32.12 MHz	
m_{35}	61.950391 amu	
μ_{35}	15.230145 amu	
m_{37}	63.947442 amu	
μ_{37}	15.597136 amu	

Table A.3: A summary of AlCl constants.

Appendix B

Spherical Tensors

The following is a brief summary of the spherical tensor notation that is used by Brown and Carrington. The general notation for a spherical tensor is $T^k_p(\mathbf{A})$ where k denotes the rank of the tensor, p denotes the component of the tensor, and $\mathbf{A}$ is the operator. k takes integer values from 0 to k. p takes integer values from $-k$ to $+k$.

Rank	**Spherical Operator**	**Cartesian Operator**
1	$T^1_0(\mathbf{A})$	A_z
	$T^1_{\pm1}(\mathbf{A})$	$\mp\frac{1}{\sqrt{2}}(A_x \pm \imath A_y)$
2	$T^0_0(\mathbf{A})$	$-\frac{1}{\sqrt{3}}(A_{xx} + A_{yy} + A_{zz})$
	$T^1_0(\mathbf{A})$	$\frac{\imath}{\sqrt{2}}(A_{xy} - A_{yx})$
	$T^1_{\pm1}(\mathbf{A})$	$\mp\frac{\imath}{2}\{(A_{yz} - A_{zy}) \pm \imath(A_{zx} - A_{xz})\}$
	$T^2_0(\mathbf{A})$	$\frac{1}{\sqrt{6}}(2A_{zz} - A_{xx} - A_{yy})$
	$T^2_{\pm1}(\mathbf{A})$	$\mp\frac{1}{2}\{(T_{xz} + T_{zx}) \pm \imath(T_{yz} + T_{zy})\}$
	$T^2_{\pm2}(\mathbf{A})$	$\frac{1}{2}\{(T_{xx} - T_{yy}) \pm \imath(T_{xy} + T_{yx})\}$

Table B.1: Spherical tensors for rank 1 (vector) and 2 (tensor) operators.

From this table, there are three entries in particular that are very useful for a $^1\Sigma^+$ state.

Spherical Operator	Useful Operator
$T^1_0(\mathbf{J})$	J_z
$T^1_{\pm1}(\mathbf{J})$	$\mp\frac{1}{\sqrt{2}}J_\pm$
$T^2_0(\mathbf{J},\mathbf{J})$	$\frac{1}{\sqrt{6}}(3J_z^2-\mathbf{J}^2)$
$T^2_{\pm1}(\mathbf{J},\mathbf{J})$	$\mp\frac{1}{2}J_\pm(2J_z\pm1)$
$T^2_{\pm2}(\mathbf{J},\mathbf{J})$	$\frac{1}{2}J_\pm^2$

Table B.2: Useful spherical tensors for an angular momentum operator $\mathbf{J}$

B.1 Wigner

B.1.1 The Wigner-Eckart Theorem

For angular momentum with magnitude j and z-component m, the matrix element of a spherical tensor $T^k_q(\mathbf{A})$ can be expressed in terms of a Wigner 3j symbol as

$$\langle j,m|\,T^k_q(\mathbf{A})\,|j',m'\rangle = (-1)^{j-m}\begin{pmatrix} j & k & j' \\ -m & q & m'\end{pmatrix}\langle j|\,\left|T^k(\mathbf{A})\right|\,|j'\rangle$$

where $\langle j|\,\left|T^k(\mathbf{A})\right|\,|j'\rangle$ is a reduced matrix element that no longer depends on the tensor element in question, q. To determine the value of the reduced matrix element, it is typically simplest to use the $q=0$ component for your tensor.

B.1.2 Common Matrix Elements

$$\langle J,\Lambda,M|\,\mathcal{D}^{(k)}_{pq}(\omega)^*\,\left|J',\Lambda',M'\right\rangle = [(2J{+}1)(2J'{+}1)]^{1/2}(-1)^{M-\Lambda}\begin{pmatrix} J & k & J' \\ -M & p & M'\end{pmatrix}\begin{pmatrix} J & k & J' \\ -\Lambda & q & \Lambda'\end{pmatrix} \tag{B.1}$$

where p is for space-fixed coordinates and q is for molecule-fixed coordinates. Converting an

operator between molecule-fixed and space-fixed (and vice versa) coordinates is done using

$$T_p^k(\mathbf{A}) = \sum_q \mathcal{D}_{pq}^{(k)}(\omega)^* T_q^k(\mathbf{A}) \tag{B.2}$$

$$T_q^k(\mathbf{A}) = \sum_p \mathcal{D}_{pq}^{(k)}(\omega) T_p^k(\mathbf{A}) \tag{B.3}$$

$$= \sum_p (-1)^{p-q} \mathcal{D}_{-p,-q}^{(k)}(\omega)^* T_p^k(\mathbf{A}) \tag{B.4}$$

B.1.3 Common Reduced Matrix Elements

$$\langle J| \left|T^1(\mathbf{J})\right| |J'\rangle = \delta_{J,J'}[J(J+1)(2J+1)]^{1/2} \tag{B.5}$$

$$\langle J| \left|T^2(\mathbf{J})\right| |J'\rangle = \delta_{J,J'}[(2J-1)2J(2J+1)(2J+2)(2J+3)]^{1/2} \tag{B.6}$$

B.1.4 Common Wigner 3j Symbols

$$\begin{pmatrix} J & 1 & J \\ -M & 0 & M \end{pmatrix} = (-1)^{J-M} \frac{M}{[J(J+1)(2J+1)]^{1/2}} \tag{B.7}$$

$$\begin{pmatrix} J & 1 & J \\ -M \mp 1 & \pm 1 & M \end{pmatrix} = (-1)^{J-M} \left[\frac{(J \pm M)(J \mp M+1)}{2J(J+1)(2J+1)} \right]^{1/2} \tag{B.8}$$

$$\begin{pmatrix} J & 2 & J \\ -M & 0 & M \end{pmatrix} = (-1)^{J-M} \frac{2[3M^2 - J(J+1)]}{[(2J-1)(2J)(2J+1)(2J+2)(2J+3)]^{1/2}} \tag{B.9}$$

$$\begin{pmatrix} J & 2 & J \\ -M \mp 1 & \pm 1 & M \end{pmatrix} = (-1)^{J-M} (1 \pm 2M) \left[\frac{6(J \pm M+1)(J \mp M)}{(2J-1)(2J)(2J+1)(2J+2)(2J+3)} \right]^{1/2} \tag{B.10}$$

$$\begin{pmatrix} J & 2 & J \\ -M \mp 2 & \pm 2 & M \end{pmatrix} = (-1)^{J-M} \left[\frac{6(J \mp M-1)(J \mp M)(J \pm M+1)(J \pm M+2)}{(2J-1)(2J)(2J+1)(2J+2)(2J+3)} \right]^{1/2} \tag{B.11}$$

B.1.5 Coupled Matrix Elements

The reduced matrix element for a tensor that acts on one component of a coupled system can be expressed as

$$\langle j_1, j_2, j | \left| T^k(\mathbf{A}_1) \right| | j_1', j_2', j' \rangle = \delta_{j_2 j_2'} (-1)^{j_1' + j_2 + j' + k} [(2j+1)(2j'+1)]^{1/2} \begin{Bmatrix} j_1' & j' & j \\ j & j_1 & k \end{Bmatrix} \langle j_1 | \left| T^k(\mathbf{A}_1) \right| | j_1' \rangle \tag{B.12}$$

The reduced matrix element for two tensors that act on different parts of a coupled

system can be expressed as

$$\langle j_1, j_2, j | \left| T^k(\mathbf{A}_1) \cdot T^k(\mathbf{A}_2) \right| | j_1', j_2', j' \rangle =$$

$$\delta_{jj'}(2j+1)^{1/2}(-1)^{j_1'+j_2+j} \begin{Bmatrix} j_1' & j_2' & j \\ j_2 & j_1 & k \end{Bmatrix} \langle j_1 | \left| T^k(\mathbf{A}_1) \right| | j_1' \rangle \langle j_2 | \left| T^k(\mathbf{A}_2) \right| | j_2' \rangle \qquad \text{(B.13)}$$

Appendix C

Artiq

The Artiq FPGA hardware offers high precision time resolution for running the experiment. The built-in scheduler can perform tasks at the microsecond scale with precision on the order of nanoseconds. The Artiq hardware is connected to a Linux control computer via a gigabit ethernet connection. Artiq scripts are programmed with Python and the entire frontend of the Artiq open-source software is built with Python. Here I will briefly summarize the devices that Artiq controls and the two main script procedures that we use.

C.1 Device Summary

At present, only two hardware interface features of Artiq are utilized: TTL out and ADC in. The TTLs are used to trigger the Yag to fire and to control the opening and closing of the Uniblitz beamline shutter. As per the manual, the Yag is triggered with a 15 μs TTL pulse to the flash lamp, followed by a 135 μs delay, and finally a 15 μs TTL pulse to the Q-switch to release the laser pulse. The shutter is built in for later use and

was installed after all the data presented here. There are multiple control modes for the shutter driver box. At present, it is configured to operate in a HI = OPEN, LO = CLOSED configuration with a customizable delay to dictate the time the shutter is open.

Artiq Device	Lab Device	Direction	Description
ttl4	Yag Flashlamp	Out	TTL pulse to trigger Yag flashlamp
ttl6	Yag Q-Switch	Out	TTL pulse to trigger Yag q-switch
ttl7	Uniblitz Shutter	Out	TTL HI/LO to control beam shutter
sampler0	ch0: Absorption PD	In	Primary measurement photodiode
	ch1: Fire-Check PD	In	PD to confirm that the Yag fired
	ch2: PMT	In	PMT to look for fluorescence in UHV
	ch3: Check 1	In	SHG 1 noise subtraction/blue check
	ch4: Check 2	In	SHG 2 noise subtraction/blue check

Table C.1: List of Devices Controlled by Artiq. PD is short for "photodiode".

Our Artiq hardware configuration has two sampler boards, only one of which is currently in use. This sampler board consists of 8 channels which are all read out in a single command. It is important to note that it was measured to take 8.97 μs to complete a single 8-channel sampler readout. The ADCs read in the voltages from the photodiodes and from the PMT (which is again built-in, but not used for the data shown here).

C.2 Scan Single Laser

The first script that we use is use the primary spectroscopy script. The main function of the script is to scan over a defined frequency range and measure the voltages on the absorption photodiode and PMT for each location. Depending on where the laser is directed, this can be used for a fluorescence beam velocity test, in-cell absorption spectroscopy, or vapor-cell pump-probe spectroscopy.

Parameter	Unit	Description
scope_count	reads per shot	Number of ADC reads per Yag shot
scan_count	averages	Number of shots per frequency setpoint
setpoint_count	setpoints	Number of frequency setpoints per scan
setpoint_min	MHz (red)	Setpoint minimum relative to offset
setpoint_max	MHz (red)	Setpoint maximum relative to offset
which_scanning_laser	-	Select which laser is scanning in frequency
offset_laser1	THz (red)	Laser 1 frequency offset to scan around
offset_laser2	THz (red)	Laser 2 frequency offset to scan around
fire_time	ms	Yag shot delay from experiment start
open_time	ms	How long the Uniblitz beam shutter is open
step_size	μs	Time between ADC reads
repetition_time	s	Time between Yag shots
yag_power	-	(Notational) Yag power lever setpoint
he_flow	sccm	(Notational) helium flow
yag_check	bool	Turn on/off Yag-checking
blue_check	bool	Turn on/off blue-checking
uniblitz_on	bool	Turn on/off beamline shutter

Table C.2: Scan_Single_Laser.py Parameters

To keep the ablation laser from digging a hole in the target, which would limit the ablation yield, we utilize the provided actuator control software to scan the ablation laser's focus over a rectangular region of the target. This is done by determining the bounds of the target, either manually with a scope or with the raster_target.py script, and setting the actuators to scan back and forth between these two bounds independently. The scanning speeds are set such that one axis is about 10 times that of the other and both are based on primes such that the exact same ablation spot setting is rarely reached. Typical values are 0.0017 mm/s for one axis and 0.013 mm/s for the other. This configuration allows for the target position to vary for each average and significantly reduce the effect of a bad ablation yield from Yag fluctuation or target quality.

C.3 Raster Target

Parameter	Unit	Description
scope_count	reads per shot	Number of ADC reads per Yag shot
scan_count	averages	Number of shots per frequency setpoint
min_x	mm	Minimum extension of x-axis actuator
max_x	mm	Maximum extension of x-axis actuator
steps_x	-	Number of x-axis actuator setpoints
min_y	mm	Minimum extension of y-axis actuator
max_y	mm	Maximum extension of y-axis actuator
steps_y	-	Number of y-axis actuator setpoints
step_size	μs	Time between ADC reads
cooling_set	THz (red)	Laser 1 fixed frequency
slowing_set	THz (red)	Laser 2 fixed frequency
repetition_time	s	Time between Yag shots
yag_power	-	(Notational) Yag power lever setpoint
he_flow	sccm	(Notational) helium flow
yag_check	bool	Turn on/off Yag-checking
blue_check	bool	Turn on/off blue-checking 1
slow_check	bool	Turn on/off blue-checking 2

Table C.3: raster_target.py Parameters

Appendix D

Line Centers

Table D.1: $Al^{37}Cl$ line center frequencies for the $X^1\Sigma^+ \rightarrow A^1\Pi$ taken from a least-square fit of the observed lines to a Voigt function. Because the Q branch has multiple overlapping lines, we report the frequency of peak absorption for the Q branch observations. Included for completeness[15].

ν	ν'	J	J'	Expt. (cm^{-1})	Dunham Model (cm^{-1})
0	0	Q	*	38237.6921(5)	38237.69492
0	0	0	1	38238.1634(5)	38238.16090
		1	2	38238.6376(7)	38238.63926
		2	3	38239.1189(5)	38239.11939
		3	4	38239.6023(5)	38239.60130
		4	5	38240.0828(4)	38240.08501
		5	6	38240.5708(9)	38240.57054
0	0	2	1	38236.737(1)	38236.73642
		3	2	38236.266(1)	38236.26514
		4	3	38235.796(1)	38235.79567
		5	4	38235.3283(5)	38235.32801
		6	5	38234.864(1)	38234.86221
		7	6	38234.4032(8)	38234.39829
1	1	Q	*	38201.9390(5)	38201.93598
1	1	2	3	38203.3512(5)	38203.35117

Table D.2: $Al^{35}Cl$ line center frequencies for the $X^1\Sigma^+ \rightarrow A^1\Pi$ taken from a least-square fit of the observed lines to a Voigt function. Because the Q branch has multiple overlapping lines, we report the frequency of peak absorption for the Q branch observations. Included for completeness[15].

ν	ν'	J	J'	Expt. (cm^{-1})	Dunham Model (cm^{-1})
0	0	Q	*	38237.4877(5)	38237.49094
0	0	0	1	38237.9691(5)	38237.96818
		1	2	38238.4589(3)	38238.45802
		2	3	38238.9509(4)	38238.94967
		3	4	38239.4426(3)	38239.44312
		4	5	38239.9388(2)	38239.93841
		5	6	38240.4364(5)	38240.43555
		6	7	38240.9341(3)	38240.93458
0	0	2	1	38236.5086(4)	38236.50944
		3	2	38236.026(1)	38236.02680
		4	3	38235.5443(4)	38235.54600
		5	4	38235.0664(4)	38235.06705
		6	5	38234.5898(5)	38234.58999
		7	6	38234.115(1)	38234.11484
1	1	Q	*	38201.2184(5)	38201.22056
1	1	0	1	38201.705(2)	38201.70510
		1	2	38202.189(1)	38202.18754
		2	3	38202.6691(7)	33202.66967
		3	4	38203.1530(5)	38203.15152
		4	5	38203.630(1)	38203.63310
		5	6	38204.114(1)	38204.11443
1	1	3	2	38199.7701(9)	38199.77233
		4	3	38199.2888(8)	38199.28843
		5	4	38198.8042(4)	38198.80428